In presenting the dissertation as a partial fulfillment of the requirements for an advanced degree from the Georgia Institute of Technology, I agree that the Library of the Institute shall make it available for inspection and circulation in accordance with its regulations governing materials of this type. I agree that permission to copy from, or to publish from, this dissertation may be granted by the professor under whose direction it was written, or, in his absence, by the Dean of the Graduate Division when such copying or publication is solely for scholarly purposes and does not involve potential financial gain. It is understood that any copying from, or publication of, this dissertation which involves potential financial gain will not be allowed without written permission.

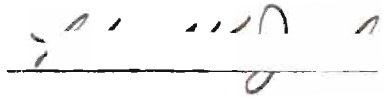

7/25/68

CHARACTERISTIC SCATTERING OF LOW-ENERGY ELECTRONS FROM PARTIALLY DISORDERED COPPER AND NICKEL CRYSTALS

A THESIS

Presented to

The Faculty of the Graduate Division

by

Leland K. Jordan, III

In Partial Fulfillment

of the Requirements for the Degree

Doctor of Philosophy in the School of Physics

Georgia Institute of Technology

June, 1969

CHARACTERISTIC SCATTERING OF LOW-ENERGY ELECTRONS

FROM PARTIALLY DISORDERED COPPER AND NICKEL CRYSTALS

Approved:

Chairman

Date approved by Chairman: Nov 26, 1968

ACKNOWLEDGEMENTS

The author wishes to express his deep appreciation to Professor E. J. Scheibner for his guidance and support in this research and in other phases of his student career. In addition to acknowledging his colleagues for their many helpful suggestions, the author would like to express special thanks to Drs. J. R. Stevenson and J. W. Hooper for their contributions as members of the reading committee and to the faculty of the School of Physics for their instruction and support.

The research forming the basis for this dissertation was carried out as a part of the program entitled "Surface Properties of Magnetic Materials," directed by Dr. Scheibner in the Physical Sciences Division. This program has been supported by the U. S. Atomic Energy Commission under the Metallurgy and Materials Program of the Division of Research. In particular, the author would like to thank Dr. D. K. Stevens, the A. E. C. Technical Monitor, whose continued interest in this program has made this research possible.

The author would finally like to express his gratitude to Mrs. Sandy Tilley for her attention and patience in typing this thesis, and to Mr. Tom Buckley for his assistance in preparation of the illustrations.

TABLE OF CONTENTS

LIST OF TABLES

LIST OF ILLUSTRATIONS

LIST OF ILLUSTRATIONS (Continued)

LIST OF ILLUSTRATIONS (Continued)

SUMMARY

Elementary excitations of solids are explored in numerous ways. In this thesis these excitations are studied by means of a low energy electron probe which impinges on a well-defined single crystal surface. The energy analysis of the back-scattered electrons in terms of various scattering mechanisms is then used to identify various aspects of the elementary excitations. Scattering mechanisms considered in the characteristic energy-loss region of the spectrum are those due to collective excitations of the electron gas in the solid, the surface and bulk plasma resonances, and the single-electron excitations such as umklapp, intraband and interband transitions.

In initial exploratory studies it is usually assumed that the solid can be represented by a perfectly ordered, infinite lattice and the electronic structure is that which results from this assumption. Furthermore, in verifying basic aspects of the theory of an electron gas, one often performs experiments on selected materials that are not complicated by other factors. Thus, much of the previous work on collective excitations has been done on simple free-electron-like metals such as aluminum and beryllium. The purpose of this thesis is therefore two-fold: (1) to examine the characteristic energy losses in the scattering of low energy electrons from copper and nickel in which there is a significant coupling between collective and single-electron excitations and (2) to utilize this coupling to examine the effect of thermal disorder.

In order to understand the dependence of the collective excitation

on electronic structure, the theory of plasmon excitations was studied with emphasis on interactions between the collective and individual electron modes. Perturbations on the crystalline potential were then examined and it was shown that these lead to a line broadening in the one-electron energy band structure. These studies were then combined to obtain a description of the plasmon dispersion in a partially disordered crystal which could be compared with the experimental results.

The energy loss spectra were obtained in a low-energy electron-diffraction system using the electron optics as an energy analyzer to obtain the distribution of electrons backscattered from the copper and nickel single crystal surfaces. Diffraction patterns were observed at all stages of the experiment to insure that the data were representative of well-defined scattering surfaces. The surface plasmon loss peak was identified in the spectra from its intensity dependence on changes in the surface dielectric constant caused by oxygen adsorption at the surface. Optical reflectivity data were taken on the same surfaces and energy loss functions derived from the real and imaginary parts of the dielectric constant were used to identify both interband transitions and the surface plasmon peak in the energy loss spectra. The plasmon excitations were found to involve both the 3d- and 4s-electrons where a strong interaction between the plasmons and tightly bound electrons depressed the plasmon energies far below their free-electron values. The half-widths of the surface and bulk plasmon loss peaks found at 8.5 and 20 ev in nickel were measured at room temperature as 1.6 and 2.5 ev, respectively; these widths were due to an electron-plasmon interaction manifested as plasmon induced single-electron excitations. Changes in the

characteristic loss spectra obtained at elevated sample temperatures were shown to arise from increased bulk and surface plasmon half-widths. These half-widths increased by about 50 per cent at 70 per cent of the melting point as a result of energy level broadening in the electronic band structure in qualitative agreement with predictions of the effects of energy level broadening in the plasmon dispersion relation developed from collective electron theory.

CHAPTER I

INTRODUCTION

The Problem

In discussions of the physical properties of solids, it is frequently tacitly assumed that the solid state may be characterized by a perfectly ordered, infinite lattice. This assumed model is greatly oversimplified since crystals in natural form contain many imperfections which may significantly alter their electronic properties. At a conference solely concerned with crystal imperfections, Seitz stated, "It is very improbable that we are yet familiar with all the intricate properties of imperfections and with all the ways in which they may combine to impart new and unusual properties to crystals."[1] Many of these properties arise from crystal disorders such as lattice imperfections, interstitial impurities and vacancies, crystalline stresses, and from discontinuities at the crystal boundaries. The effects of these disorders are not easily predicted, and empirical studies are complicated by interactions among the different types of imperfections simultaneously present in a real solid.

The properties of solids are determined mainly by electron behavior, and thus the effects of disorder on electron motion are of major interest to solid state physicists. This dissertation is a study of disorder effects, emphasizing thermal perturbations on the electronic band structure in metals. The method employed is to examine the collective

electron excitations in a partially disordered crystal by contrasting excitation spectra obtained at high temperatures with those obtained at room temperature. As these excitations are characteristic of the metal's electronic structure, the differences in the spectra are attributed to thermal disorder effects on the band structure.

A number of mechanisms are responsible for the characteristic excitations including bulk and surface plasmon resonances, and umklapp, intraband, and interband transitions. The plasma resonances are collective excitations of the electron gas in the metal, and their existence reflects long-range Coulomb effects which couple the motions of many individual electrons. Umklapp processes are excitations of single electrons in which there is a momentum exchange with the lattice as a whole; intraband and interband transitions are special umklapp processes in which electrons in a particular band are excited to unoccupied levels in the same band or in higher energy bands, with momentum conserved in the two-body interaction. These characteristic excitations can be studied by energy loss analyses of electrons backscattered from metallic single crystals.

In order to interpret the effects of disorder on inelastically scattered electrons, the electron interactions in solids which give rise to the characteristic energy losses must first be examined to show how the collective excitations are related to the electronic band structure. It is also necessary to establish theoretical results concerning the effects of thermal disorder on electronic structure in order that these perturbations may be properly treated in analyses of the characteristic energy loss spectra. Finally, these studies should be combined to pre-

dict the behavior of elementary excitations in a disordered crystal.

For the disorder effects on electronic structure to be experimentally observable, the samples studied were selected to display significant electron-plasmon coupling. The transition metals have long been recognized as having complex 4s- and 3d-electron energy bands. Furthermore, it has been suggested that the plasmon excitation energies in copper and nickel are determined by their spectrum of s- and d-electron interband transitions.[2] If this is the case, these excitations are indeed sensitive to the electronic band structure, and, as disorder effects appear, the plasmon behavior would be influenced in such a way as to reflect the changes in the electronic structure. On the other hand, the plasmon excitations in these metals have been attributed to a free gas of 4s-electrons.[3] In this case, no differences in the excitation spectrum would be seen since the free-electron behavior would not be affected except by small phonon interactions.

In this study, the plasmon behavior in copper and nickel was first investigated to establish that the collective excitations were sensitive to the electronic band structure because of plasmon excitations of tightly-bound d-electrons. The plasmon excitations were observed through energy analyses of characteristically scattered low-energy electrons. Optical reflectivity data were also obtained since the surface plasmon loss function could be determined from the optical constants to support the identifications made in the energy loss studies. Finally, the energy loss data were obtained at elevated sample temperatures to reveal the effects of increased disorder on the plasmon excitation spectra. An ultrahigh vacuum, low-energy electron-

diffraction (LEED) system was used in this investigation in order that the sample surface conditions could be carefully monitored. The electron optics was used as a spherical retarding potential energy analyzer to obtain the plasmon excitation spectra in energy distributions of backscattered electrons. Further, an optical monochromator was added to the LEED system to permit optical reflectivity measurements from well characterized sample surfaces.

The experimental methods outlined above were employed to give the following results: (1) the characteristic energy losses in copper and nickel were obtained for various surface conditions permitting the identification of the different loss mechanisms; (2) optical reflectivity measurements were made to support the identification of the surface plasmon; (3) the plasmon excitations in both metals were shown to be sensitive to the spectrum of 3d-electron excitations; and (4) changes in plasmon excitation spectra produced by elevated sample temperatures were explained on the basis of thermal disorder effects on the electronic band structure, in agreement with the theoretical description of plasmon dispersion in a disordered crystal.

The remainder of this thesis is concerned with the concepts, experimental methods and results summarized here. The following introductory section in this chapter contains background information about collective excitations and disorder studies relevant to this dissertation. In the next chapter, the collective theory of metals is discussed, and a model is presented to explain the effects of thermal disorder on electronic structure and on the plasmon excitations. In Chapter III, the experimental apparatus and techniques used to obtain the characteristic

energy loss spectra and optical reflectivities are described. The energy loss and optical data for the clean surfaces and for surfaces with different amount of adsorbed oxygen are presented in Chapter IV, and the characteristic energy loss data obtained at high temperatures are discussed in terms of the energy band structure in the disordered surface layers.

Background

Characteristic Energy Losses

The study of characteristic excitations using electron energy loss analysis involves monoenergetic electrons incident on a crystal. These electrons are scattered while interacting with the sample and are collected as a function of their energy. The energy distributions contain elastically scattered electrons usually assumed to appear in LEED patterns, inelastically scattered electrons which have lost characteristic amounts of energy to the solid through umklapp processes or by exciting plasmon resonances, and electrons which are emitted as true secondaries because of multiple inelastic collisions or discrete processes such as Auger emission. The characteristically scattered electrons are of primary interest here as they would contain information concerning the effects of thermal disorder on the electronic structure.

Electron scattering as a technique for investigating the characteristic excitations of a metal began in 1930 with Rudberg's qualitative analyses of backscattered low-energy electron energy losses.[4] The majority of recent work, however, has employed either modified electron microscopes using transmission of high-energy electrons through thin films or deflection spectrometers using reflection from freshly evapo-

rated surfaces.[5] The development of these measurements has been troubled by inconsistencies both in qualitative observations and quantitative measurements. The principle cause of discrepancies in reported results appears to have arisen from different sample surface conditions; the addition of LEED to electron scattering studies has already provided more consistent results as this combination of techniques can be used to obtain energy loss data from well defined and reproducible scattering surfaces.

Several explanations have been given to the peaks in the characteristic energy loss spectra. Rudberg and Slater originally suggested that the loss peaks arose from interband excitations of single electrons,[6] and this suggestion has been employed by Wanatabe[7] and by Leder, Mendlowitz and Marton[8] to explain their observations on a number of metals, including copper and nickel. If the characteristic losses are interband transitions, some similarity is expected with the absorption maxima found on the short-wavelength side of x-ray absorption edges. The difference in energy between the absorption edge and the fine structure on the high energy side of that edge represents the difference in energy between the unoccupied density of states above the Fermi level and the maxima in the occupied density of states immediately below the Fermi level. These energy values should correspond to interband transitions in which the incident electron excites a band electron to one of the vacant states above the Fermi level. A comparison between x-ray absorption and characteristic energy loss data has been made by Leder et al.[8] and some correlation was found. However, Gauthe[9] has since suggested that the corresponding x-ray emission line rather than the absorption edge should be the point

from which the absorption maxima should be measured. For the compounds studied by Leder et al.[8] the difference between these reference points is 5 to ten ev which would invalidate the comparison with x-ray absorption data.

Sternglas[10] proposed that the losses be interpreted as individual atomic excitations and calculated the energy loss spectrum of aluminum in good agreement with the results of Ruthemann[6] and Marton and Leder.[11] Yet, a series of electron energy loss measurements in the vapors of a number of materials confirmed the known atomic transitions but showed no correlation with the energy losses in the solid state.[12] Since it is expected that the materials should display the same atomic ionization losses in the solid and the vapor states, the agreement in the case of aluminum may be accidental.

Bohm and Pines' collective theory of metals has given a very satisfactory understanding of the loss mechanisms as many-particle excitations of conduction electrons.[13] The first observation of characteristic energy losses in multiples of a basic quantum, as expected for multiple plasmon excitations, was made by Ruthemann[6] and Lang[14] on beryllium and aluminum, metals for which one expects to find a free-electron plasma with sharp lines in the energy loss spectrum. Powell and Swan have also shown the loss spectrum of aluminum to consist of combined bulk and surface plasmon losses.[15] Furthermore, the variation of energy loss intensity predicted by the collective theory has been verified by Wanatabe,[16] Meyer,[17] and Marton.[18] The collective theory has also been successful in predicting incident energy and surface effects on the intensity of the bulk and surface plasmon losses.

In summary, the characteristic energy losses may be interpreted as either collective or single-particle excitations. These processes are usually treated independently although they are strongly coupled in some materials with the result that the plasmon energies may be shifted from the free-electron values. Failure to recognize this electron-plasmon interaction has sometimes made interpretation of energy loss data quite difficult. This is particularly true for the transition metals for which there is no satisfactorily theoretical description of the interactions between 3d- and 4s-electrons.

The collective modes of behavior of a free-electron gas are classical plasma oscillations at characteristic frequencies ω_p, and their energy quanta are called plasmons. The collective behaviors may be described as an oscillatory motion of the electrons in the body of a metal and as similar motion of the electrons located near the metal's surface where the effect of the surface potential is to shift the surface oscillation frequency below the bulk oscillation frequency. The nature of these oscillations can be visualized by considering a momentary charge fluctuation in the electron gas created by a passing electron. The neighboring electrons rush into the affected area in an attempt to screen out the disturbance. These electrons acquire momentum and more electrons accumulate in the region than are necessary to restore charge neutrality. The excess negative charge thus created repels electrons outwards again creating oscillations of the bulk electron gas at the frequency[13]

$$\omega_p = \left(\frac{4\pi ne^2}{m}\right)^{\frac{1}{2}} . \qquad (1)$$

The excitation of collective resonances is easily described in metals with free valence electron gases, but when the valence electrons interact strongly with the electrons bound to the periodic ion cores, the oscillation frequencies cannot be readily predicted. In these metals, collective excitations of the electrons are damped by single-electron excitations in which the plasmon decays into an individual-particle excitation of the same momentum. The plasmon still exists as an elementary excitation but the breadth of its loss line is increased and its energy may be substantially shifted from the free-electron value, $\hbar\omega_p$, toward either higher or lower energies.

Theoretical attempts to account for the electron-plasmon interaction in non-ideal metals were made by Wolff[19] and Adams[20] and prepared the way for the more advanced calculations of Bohm and Pines.[13] These latter authors considered collective excitations in which an interaction between the plasmon field and the individual electrons was included to account for the damping of the collective motion. They obtained a plasmon dispersion relation

$$1 = \frac{\omega_p^2}{n} \sum \frac{f_{on}(k)}{\omega^2 - \omega_{on}^2} \qquad (2)$$

in which the single-particle excitations that damp the plasmon motion are described by oscillator strengths f_{on} and frequencies ω_{on}. This relation determines the shifted bulk plasmon frequency ω from the f_{on}'s and ω_{on}'s characteristic of the metal considered. Generally, there is a lack of knowledge concerning these parameters so Equation 2 cannot be

solved explicitly for other effects on plasmon behavior, for instance those caused by crystal imperfections, which also need to be considered in a complete treatment.

Disorder Effects in Crystals

The influence of crystal imperfections on the physical properties of solids can not be overemphasized. Electrical resistance, semiconductivity, deformation characteristics, and the diffusion of matter are just a few phenomena which depend on defects of one kind or another. Some crystal defects such as surface steps, vacancies, and foreign atoms in either interstitial or substitutional positions are of a localized nature and, when they exist singly, are not easily observed. These defects introduce energy levels which are not representative of an ideal lattice and which can not be easily detected when the imperfections are several atoms apart. Fortunately, the imperfections normally interact with one another and form stable, long-range groups making them more susceptible to experimental measurements.

An "extended defect" which interacts with imperfections in every crystal is the surface itself. When a crystal is terminated at some plane, large stresses arise between the atoms in layers at the surface as they adjust their positions to account for the new boundary. Since the penetration depth of low-energy electrons is limited to the first few atomic layers, LEED is ideally suited to study the scattering potentials near a surface. Stresses existing in surface layers have been observed to change the lattice constants between atoms both normal and parallel to the surface. Although these changes are usually small, the stresses in Si[21] and Ge[22] surfaces are apparently large enough to cause

reordering of the atomic positions from the bulk arrangement.

Feuchtwang[23] has described the static equilibrium configuration of a lattice surface in terms of a set of displacements relating the actual positions to those which the atoms would assume if they were in an infinite crystal. The displacements were calculated from a set of difference equations which described small, time dependent displacements of the lattice atoms from their equilibrium condition resulting from removal of all the crystal above a lattice plane. The general conclusion was that the two-dimensional structure parallel to the surface could be larger than that of the bulk lattice structure. The model also showed that changes in the spacing of atomic planes normal to the boundary varied monotonically with distance from the boundary. These results provided initial support for interpretations of LEED patterns which required reassignment of lattice constants.

Taloni and Haneman[24] have reported computer calculations of Si and Ge surface structures in which a Morse-like potential with an adjustable bonding energy and shape factor was used for the interatomic potential. Surface free-energies, elastic constants, and sublimation energies were calculated for various spacings of surface atoms normal and parallel to the surface. The surface structure which gave the minimum free-energy and agreed with experimentally measured elastic constants was found to correspond to surface arrangements predicted for Ge from LEED analysis. Similar calculations were carried out for Si and showed that departures from the bulk interlayer separation were expected and that they agreed with the surface model presented by Haneman.[25] Although these calculations give soundness to the models proposed for reconstructed Si and Ge surfaces, Bauer[26] has recently attributed the rearrangement

of surface atoms to impurity effects on the surface free energy. These questions are yet unanswered and form the basis for current research.

Another fundamental imperfection, designated by Tamm[27] as the phonon, is associated with quantum excitation of the vibrational modes within a crystal. The contributions of these phonons are most important in thermal conductivity, in producing large displacements which can lead to interstitial and vacancy defects, in semiconductivity, and in creating excitons. Interactions between atomic thermal vibrations and the surface defect in a crystal have recently received much theoretical and experimental attention with the advent of electron scattering as a tool for studying atomic behavior at surfaces.

LEED investigations of surface atom vibrations have been reported by MacRae[28] from data concerning the intensity of beams diffracted from nickel samples at elevated temperatures. These studies indicate that the mean-square vibrational amplitude of atoms in the surface plane is greater than that of the atoms in the crystal bulk for the same vibrational direction. Other studies[29] have shown that the component of vibrational amplitude normal to the surface is not equal to the tangential component. A theoretical basis for these observations was first given by Wallis and Gazis[30] who calculated the relations between atomic mean-square velocity and interatomic force constants and showed that the different forces acting on surface atoms lead to a corresponding difference in the mean-square velocity. Theoretical descriptions of surface atom motions have also been given by Clark, Harris and Wallis[31] and by Maradudin and Melngaillis.[32] In general, their results are in qualitative agreement with experimental data although detailed comparisons have not been possible.

Jones, McKinney and Webb[33] and Aldag and Stern[34] have experimentally observed an anisotropic background superimposed on LEED patterns. This background is attributed to extraordinary phonon modes associated with the surface defect. The temperature dependence of the diffuse background is due to a combination of the Debye-Waller factor and single phonon scattering, and thus the background increases with increasing temperature. In the kinematical approximation, Huber[35] has investigated this thermal diffuse scattering of low-energy electrons. The diffraction was assumed to arise mainly from the surface layer, and the thermal motion in the crystal was approximated by vibrations in an isotropic, elastic continuum. His results showed that the surface boundary conditions do not change the qualitative behavior of the scattering and except for a doubling factor in the intensity of the Bragg diffraction spots agreed with the work of Wallis and Maradudin[36] who applied Green's function techniques to a discrete lattice. In both cases, thermal diffuse scattering was attributed to nonpenetrating radiation reflected by surface phonon modes created by the introduction of surface boundary conditions.

These authors have emphasized the study of imperfections using elastically scattered electrons. The electrons characteristically scattered from the crystal have lost energy to excitations involving the electronic structure in the sample bulk. The effects of thermal disorder on the electronic structure could therefore be reflected in the characteristically scattered electrons. No previous work has specifically dealt with this problem but perturbations on the electronic structure in a disordered solid have received some attention.

The very high degree of regularity among atoms in a perfectly

ordered crystal is the guide to its structure and electronic properties. The long-range periodic potential gives rise to an energy band structure and Brillouin zones. As disorder is introduced into a crystal, the potential becomes an aperiodic function of position and electron wavefunctions can no longer be easily found. In recent years, the properties of electrons in disordered solids and liquids have been investigated by Edwards,[37] Jones,[38] Ziman,[39] and others through Green's function techniques. These studies have shown that short-range atomic order created by a densely-packed assembly of ions causes a general electronic structure, including gaps in the energy spectrum, to persist into a completely disordered liquid. Sergeeva[40] and Jones[41] have studied the effects on the band structure as the temperature is raised to the melting point. They concluded that the energy bands are broadened by displacement of energy levels and that the line widths of the individual levels are increased by ionic disorder. These effects would be reflected in the plasmon excitation spectrum obtained from metals with considerable plasmon scattering since the oscillator strengths and frequencies of the single particle excitations in Equation 2 would be affected in the disordered crystal. To take fullest advantage of this opportunity for research requires that the results from disorder studies be combined with the collective theory of metals to provide a theoretical description of the characteristic excitations in disordered crystals which can be compared with experimental observations. This is the purpose of the next chapter.

CHAPTER II

THEORETICAL CONSIDERATIONS

This chapter is concerned with the effects of thermal atomic motion on the distribution of characteristically scattered electrons. The majority of the characteristic electrons are scattered in the solid after losing energy to collective excitations whose breadth and energy are determined mainly by the electronic energy band structure of the metal considered. Thus, disorder effects on the characteristic excitations are realized through thermal perturbations on the electronic band structure. In the next section of this chapter, the nature of plasmon excitations is fully explored in order to demonstrate the coupling of plasmon behavior with the electronic structure in a solid. Following this, the effects of thermal disorder on the electronic band structure are discussed, and a plasmon dispersion relation for collective motion coupled to single-electron excitations in a disordered crystal is developed.

Collective Excitations in Solids

Although plasma oscillations are implicit in much work on the optical properties of solids, their existence as an elementary excitation was probably first suggested by Steenbeck in 1932[42] when he studied the problem of selective reflection of light from metals. In 1943, Kronig and Korringa[43] treated the energy losses of charged particles passing through a metal in a plasma oscillation theory; however, the full sig-

nificance of these oscillations was not recognized until the appearance in 1951 of a series of apeprs by Bohm and Pines[13] who developed the collective theory of metals to explain certain electrical and magnetic properties previously not understood. Since that time, considerable emphasis has been placed on the importance of plasmon excitations in determining properties of solids. An initial understanding of these excitations can be gained by a consideration of collective motion in the free-electron gas.

Plasma Oscillationsin Free-Electron Gases

We begin with a study of the manner in which Coulomb interactions in an assembly of free-electrons bring about organized collective oscillations. Instead of following the motion of a particular particle, as is done in the single-electron model, the gas is described in terms of Fourier components of the electron density which are proportional to the density fluctuations of the electron gas. It is found that these components can be split into two groups. One group represents an organized oscillation at the characteristic plasma frequency ω_p; the other is associated with random thermal motion of the individual electrons and shows no collective behavior.

Each electron in the assembly is acted on by the sum of forces from all of the other electrons plus that force resulting from a uniform positive background. It is convenient to expand the potential energy of interaction between the $i^{\underline{th}}$ and $j^{\underline{th}}$ electron,

$$V_{ij} = \frac{e^2}{|\underline{x}_i - \underline{x}_j|} \quad ,$$

as a Fourier series in a unit volume with periodic boundary conditions giving

$$\frac{e^2}{|\underline{x}_i - \underline{x}_j|} = 4\pi e^2 \sum_{\underline{k}} \frac{1}{k^2} e^{i\underline{k} \cdot (\underline{x}_i - \underline{x}_j)} .$$

The system Hamiltonian is then

$$H = \sum_i \frac{p_i^2}{2m} + 4\pi e^2 \left(\frac{1}{2}\right) \sum_{i \neq k} \sum_{k=-\infty} \frac{1}{k^2} e^{i\underline{k} \cdot (\underline{x}_i - \underline{x}_j)} , \qquad (3)$$

where the last term describes the interparticle Coulomb interactions. We find the equation of motion of the $i^{\underline{th}}$ electron from

$$m\ddot{\underline{x}}_i = - \nabla_i V_i = - 4\pi e^2 \sum_{j,k}{}' \frac{i\underline{k}}{k^2} e^{i\underline{k} \cdot (\underline{x}_i - \underline{x}_j)} ,$$

where V_i is the Coulomb potential of the $i^{\underline{th}}$ electron,

$$V_i = \sum_{j \neq i} V_{ij} = 4\pi e^2 \sum_{j \neq i, k} \frac{1}{k^2} e^{i\underline{k} \cdot (\underline{x}_i - \underline{x}_j)} .$$

The electron density operators, $\rho(x)$, are introduced under the assumption that we are dealing with point particles, so that

$$\rho(\underline{x}) = \sum_i \int \delta(\underline{x} - \underline{x}_i) \ .$$

which has Fourier components

$$\rho_k = \int \rho(\underline{x}) e^{-i\underline{k} \cdot \underline{x}} d\underline{x} = \sum_i e^{-\underline{k} \cdot \underline{x}_i} \ .$$

Note here that $k = 0$ corresponds to $\rho_o = n$, the total number of particles, but since we are working in a unit volume, ρ_o is the mean electron density and is exactly cancelled by the uniform positive background. Hence, $k = 0$ is neglected in the Fourier expansion of the interaction as denoted by a prime on the sum. For $k \neq 0$, the ρ_k describe fluctuations of the gas about the mean electron density. In terms of these density fluctuations, then, the equation of motion of the $i^{\underline{th}}$ electron can be written as

$$\ddot{\underline{x}}_i = \dot{\underline{v}}_i = - \frac{4\pi i e^2}{m} \sum_k{}' \frac{\underline{k}}{k^2} \rho_k e^{i\underline{k} \cdot \underline{x}_i} \ . \qquad (4)$$

The equations which describe fluctuations in the electron density caused by Coulomb interactions between the particles can be obtained by simple time differentiation of the ρ_k; thus,

$$\dot{\rho}_k = \sum_i \left(- i\underline{k} \cdot \underline{v}_i \right) e^{- i\underline{k} \cdot \underline{x}_i} ,$$

and

$$\ddot{\rho}_k = - \sum_i \left[(\underline{k} \cdot \underline{v}_i)^2 + i\underline{k} \cdot \dot{\underline{v}}_i \right] e^{- i\underline{k} \cdot \underline{x}_i} .$$

In this last equation we can substitute for $\underline{v}_i$ from Equation 4 to get

$$\ddot{\rho}_k = - \sum (\underline{k} \cdot \underline{V}_i)^2 e^{- i\underline{k} \cdot \underline{x}_i} \qquad (5)$$

$$- \sum_{i,j,k'} \frac{4\pi e^2}{m(k')^2} \underline{k} \cdot \underline{k}' e^{i(\underline{k}' - \underline{k}) \cdot \underline{x}_i} e^{- i\underline{k}' \cdot \underline{x}_j} .$$

If we consider the terms in the second sum with $k' = k$, this part of that sum becomes

$$- \frac{4\pi n e^2}{m} \sum_j e^{- i\underline{k} \cdot \underline{x}_j} = - \frac{4\pi n e^2}{m} \sum_i e^{- i\underline{k} \cdot \underline{x}_i} ,$$

and that part with $\underline{k}' \neq \underline{k}$ is

$$- \frac{4\pi e^2}{m} \sum_{i,j,k' \neq k} \frac{\underline{k} \cdot \underline{k}'}{(k')^2} e^{- i\underline{k}' \cdot \underline{x}_j} \sum_i e^{i(\underline{k}' - \underline{k}) \cdot \underline{x}_i} .$$

Here we have separated the sum

$$\sum_i e^{i(\underline{k}' - \underline{k}) \cdot \underline{x}_i} ,$$

which is a phase factor and tends to vanish since there is a very large number of particles distributed throughout the gas in random positions. To first order we drop these terms, the "random phase approximation"[44] and the equations of motion of the electron density fluctuations become

$$\ddot{\rho}_k = - \sum_i (\underline{k} \cdot \underline{v}_i)^2 e^{- i\underline{k} \cdot \underline{x}_i} - \frac{4\pi n e^2}{m} \sum_i e^{- i\underline{k} \cdot \underline{x}_i} . \qquad (6)$$

The first term on the right-hand-side would be present even in the absence of particle interactions since it arises from the thermal motion of the electrons. The second term represents the effects of particle interactions which dominate the electron motion when the thermal effects can be neglected in comparison with the collective effects; i.e., when

$$\frac{4\pi n e^2}{m} \gg \langle (\underline{k} \cdot \underline{v}_i)^2 \rangle .$$

Therefore, when the disruptive thermal effects are small, the equation of motion describes simple harmonic motion through

$$\ddot{\rho}_k + \left(\frac{4\pi ne^2}{m}\right) \rho_k = 0 \ ,$$

so as a result of the Coulomb interactions, the electron density oscillates at the well-known plasma frequency

$$\omega_p = \left(\frac{4\pi ne^2}{m}\right)^{\frac{1}{2}} \ . \tag{7}$$

The plasma frequency ω_p is of the order of 10^{16} sec^{-1} and the quantum of excitation, called a plasmon, has a corresponding energy in the range 10 to 20 ev for most metals. This energy is greater than that of an electron at the top of the Fermi distribution, so the probability that an electron in the metal can excite a plasma oscillation is vanishingly small. A fast particle traversing the sea, however, has the energy required to create one or more plasmons, and in an energy analysis of the electrons either transmitted through a metallic foil or backscattered from a crystal, these excitations are seen as appropriate energy losses.

The plasma oscillations just described represent fluctuations of the free-electron density in the bulk of the material, and their excitation would represent the only collective "characteristic loss mechanism" if the crystal were infinite. However, when a bounding surface is present, the electric field extends beyond the specimen boundary and polar-

izes the charges in the surface layers to produce an electric field opposing the bulk field. Thus the electric field at the surface is weakened compared to that in the bulk, leading to a reduction in frequency of the oscillations of surface electrons relative to the bulk electron oscillation frequency. The frequency of this charge oscillation in the surface layers, the surface plasmon, was predicted by Ritchie[45] to be

$$\omega_s = \frac{1}{\sqrt{2}} \omega_p \tag{8}$$

for an ideal free-electron metal with a clean, planar surface bounded by vacuum.

Because the frequency of the surface plasmon oscillation depends on the magnitude of the depolarizing field produced at the surface, its energy may be affected by any films or contaminants on the specimen surface. Stern and Ferrell[46] showed that the presence of a thin layer of oxide should lead to disappearance of the surface plasmon loss given by Equation 8 and to the appearance of a modified surface plasmon loss with an energy $\hbar\omega_{ms}$ given by

$$\hbar\omega_{ms} = \frac{1}{\sqrt{1+\epsilon'}} \hbar\omega_p \tag{9}$$

where ϵ' is the dielectric constant of the surface medium. This lowest loss is predicted to rise to a maximum intensity approximately 40 per cent of that of the surface plasmon loss in the unoxidized specimen.

The above results were derived on the assumption that the metal's valence electrons may be treated as a free gas neutralized by a continuous positive background charge representing the fixed ion cores. This description may be applied ideally to metals such as aluminum, since the binding energy difference between the core electrons and the three 3p valence electrons is large and since the core electrons are not easily polarized. For aluminum, one predicts the bulk plasmin excitation energy to be 15.8 ev using Equation 7; the surface plasmon value for the clean surface is similarly predicted using Equation 8 to be 11.2 ev. These values have been experimentally confirmed by Powell and Swan[15] in measurements of electron energy losses from evaporated Al films; measured losses were 15.3 and 10.3 ev and other losses representing multiple excitations of bulk and surface plasmons. Furthermore, later work[47] showed that the 10.3 ev loss displays the predicted intensity dependence on the degree of oxidation of the surface and that a modified surface loss appears at a lower energy as expected. The agreement between the experimental observations and predictions of the collective theory demonstrates the applicability of the collective theory to free-electron metals, although the results of this model may not be applied directly to more complicated metals.

Plasma Oscillations in Real Solids

So far we have considered only the free-electron model of a metal in which the ionic lattice is replaced by a uniform distribution of positive charge. This model is likely to give reasonable results for metals in which the core electrons are very tightly bound; the periodic potential of the lattice must somehow affect the plasma frequency, how-

ever, since it causes the electron wavefunctions to differ to some extent from free-electron plane waves. In an extreme case when the energy distinction between core and valence electrons is small, direct participation of core electrons in the plasmon excitations may occur and serious discrepancies are expected with the free-electron theory.

A logical step to account for the periodic lattice is to replace the electron mass in the expression for ω_p by the electron's effective mass. This was employed by Wolff in 1953[19] in his semi-classical treatment of plasma oscillations which has since been discussed in more detail by Hubbard[48] and Kanazawa.[49] Wolff accounted for the periodic potential in a self-consistent Hartree calculation which led to the plasmon dispersion relation

$$\omega^2 = 4\pi ne^2 \frac{1}{m_z^*} + k^2(\partial E/\partial P_z)^2$$

where m_z^*, the effective mass, is defined from

$$\frac{1}{m_z^*} = \frac{\partial^2 E}{\partial P_z^2}$$

and the averages are taken over occupied electron states. Hence, this relation includes only the effects of intraband transitions; Adams[20] extended the work to include interband transitions in the plasmon scattering. His perturbation was based on Bohm and Pines' generalized

plasma coordinates,[13] and, although the resulting dispersion relation does admit transition between bands, it can be interpreted only if the excitation frequencies are either large or small compared to the plasmon energy. In the former case, Adams concluded that a shift of some magnitude above ω_p was generally expected although it will be shown later that this conclusion is incorrect. For low-energy transitions, he concluded that the shift was almost always negligible.

When single-electron transitions between bands are considered along with the transitions within the conduction band, one finds that a broadening in the observed plasmon loss distribution is expected in addition to the energy shift. It was suggested that this broadening in the transition metals may be due to a strong coupling between electrons in overlapping s and d bands which makes possible a rapid transfer of energy from a plasma oscillation in the s-band to a single d-electron, thus leading to a short lifetime and large energy width for the oscillations.[19] Therefore to calculate the width of a plasmon loss line due to such interband transitions, one first determines the rate at which plasma oscillations excite electrons and then uses the Uncertainty Principle to obtain the energy broadening. This calculation was first carried out in detail by Adams,[20] who showed that the matrix element for excitation of an electron by a plasma oscillation is identical with that for the absorption of a phonon of the same energy. Taking advantage of this fact, Wolff[19] expressed the energy width of the plasmon oscillation in terms of the parameter nk for optical absorption as

$$E/\hbar\omega_p = nk \ .$$

A plasmon dispersion relation which accounts for the effects of interband transitions on the plasmon excitations may be obtained using a model suggested by Mott.[51] According to this model, the electron-plasmon scattering is described in terms of a classical treatment of harmonically bound electrons excited by an electromagnetic field of varying frequency. The plasma oscillation is pictured as an electric field $E = E_o \cos\omega t$ oscillating at frequency ω in a solid where electrons are bound by Hooke's law forces to their respective atoms and thus exhibit oscillatory motion about that atom. If the natural frequency of each electron oscillation is ω_o, then the equation of motion in the presence of the plasma electric field is

$$\ddot{x} + \omega_o^2 x = - \frac{e}{m} E_o \cos\omega t \ , \tag{10}$$

where damping of the electron response has been set to zero. The solution of this equation is

$$x = x_o e^{-\omega_o t} + \frac{e/m}{\omega^2 - \omega_o^2} E_o \cos\omega t \ , \tag{11}$$

where the first term disappears rapidly. The problem is now to relate this expression for the electronic displacement to the electron response in the metal.

The plasma oscillation can be thought of as a longitudinal wave of electron motion so we consider the polarization of each electron,

-ex, arising from the plasma electric field. The polarizability of each single electron is

$$\frac{-ex}{E_o \cos\omega t} = \frac{e^2/m}{\omega_o^2 - \omega^2} \tag{12}$$

from Equation 11. To include in this model the many oscillation frequencies which would exist for electrons bound in a solid, we replace ω_o by a series of oscillation frequencies ω_i and include a factor f_i which describes the strength or magnitude of the charge oscillations at each frequency ω_i. The total polarizability of the solid is thus a sum over the frequencies and oscillator strengths of the solid and can be written as

$$\alpha = \frac{e^2}{m} \sum_i \frac{f_i}{\omega_i^2 - \omega^2} . \tag{13}$$

Further, the possibility that electrons are excited from the ground state to a series of higher energy levels by the plasma oscillation may be accounted for by summing over the occupied ground state energy levels in a reduced zone and considering excitations to all energy levels above the ground level. To do this, we define $\underline{k}$ as the reduced wave vector of a one-electron state and n = 0 as the level occupied in the ground state in the first Brillouin zone. The energy absorbed by an electron of wavevector $\underline{k}$ in making an interband transition from the

occupied level n = 0 to a higher unoccupied level in the zone n is then $\hbar\omega_{\underline{k}n}$. The polarizability of the entire solid is therefore expressed as

$$\alpha = \frac{e^2}{m} \sum_{\underline{k}} \sum_{n} \frac{f_{\underline{k}n}}{\omega_{\underline{k}n}^2 - \omega^2} \quad . \tag{14}$$

The plasmon dispersion relation can now be obtained by determining the polarizability α for the longitudinal response. This can be done by describing the fluctuations in the electronic charge density due to the plasma oscillation and using the definition of charge polarization. Thus if n is density at any moment during the oscillation, Poisson's equation

$$\nabla \cdot E = - 4\pi\rho = 4\pi e(n - n') \ , \tag{15}$$

gives the plasma electric field in terms of the electronic charge fluctuations. The polarization current density $\underline{J}$ is defined by

$$\underline{J} = \alpha \frac{\partial E}{\partial t} \tag{16}$$

and must satisfy the continuity equation

$$\nabla \cdot \underline{J} = \frac{\partial \rho}{\partial t} = \alpha \frac{\partial}{\partial t} (\nabla \cdot E) \ . \tag{17}$$

From Equations 15 and 17 we therefore have

$$- e \frac{\partial}{\partial t} (n - n') = \alpha 4\pi e \frac{\partial}{\partial t} (n - n') ,$$

so $\alpha = - 1/4\pi$ for a longitudinal wave charge fluctuation.

Returning to Equation 13 and substituting for α leads to a final plasmon dispersion relation

$$1 = \frac{4\pi e^2}{m} \sum_{\underline{k}} \sum_{n} \frac{f_{\underline{k}n}}{\omega^2 - \omega_{\underline{k}n}^2} \tag{18}$$

which determines the plasma frequency ω from the oscillator strengths and frequencies of the interband transitions coupled to the plasmon motion. In spite of the simplicitly of the model, this relation is essentially that determined by Bohm and Pines.[13] As shown in Appendix A, an involved quantum mechanical treatment which includes the interband scattering of electrons by the plasma motion through an interaction between plasmon field and single-particle density operators leads to this same result.

This dispersion relation includes both intraband and interband scattering of the plasmon motion. The effects of intraband excitations can be separated and handled without much difficulty; a proper identification of their oscillator strengths made in Appendix A shows that

$$\omega = \omega_p \left(\frac{m}{m^*} \right)$$

which is the effective mass approximation used by Wolff[19] to successfully account for free-electron excitations. However, no simple relation such as this can account for the shift and broadening of plasmon loss lines due to interband scattering. In fact, when single-particle excitation frequencies exist near ω, a resonance occurs in Equation 18 and may substantially raise or lower the plasmon energy. This possibility precludes an accurate perturbation treatment such as that suggested by Adams and shows why his conclusions are subject to error. Fortunately, a dielectric treatment of the electron gas is able to describe the collective excitations in more complicated systems.

Dielectric Response of an Electron Gas

Collective excitations in solids are conveniently described using the dielectric model, which offers the advantage that one is able to describe both collective and individual electron interactions within the same framework. Furthermore, this approach clearly illustrates the important connection between the energy distributions of electrons undergoing characteristic energy losses and the energy loss function determined from optical reflectivity data, as mentioned earlier. In the dielectric approach, it is assumed that the ensemble of conduction electrons in a metal may be characterized by a dielectric constant which is a function of both the frequency and wavevector of an electromagnetic disturbance in the solid. If, for example, the solid is bombarded by a beam of relatively fast electrons, then the response of the electron gas to the external probe is described by the complex dielectric constant $\epsilon(k,\omega)$; the magnitude represents the coefficient of proportionality of the response and the phase represents the time delay of the retarded response.

Several authors[52,53] have investigated this longitudinal dielectric constant and have showed that the expression

$$\epsilon(k,\omega) = 1 - \frac{1}{n} \sum_{n} f_{on} \frac{\omega_p^2}{\omega^2 - \omega} \tag{19}$$

describes the response of a nearly free-electron gas to perturbing Coulomb forces. Previously, the plasmon dispersion relation which accounts for the effect of a plasmon interaction with single-particle excitations has been written as

$$1 = \frac{4\pi e^2}{m} \sum_{\underline{k}} \sum_{n} \frac{f_{\underline{kn}}}{\omega^2 - \omega_{\underline{kn}}^2} . \tag{18}$$

The momentum dependence of the single-particle excitations in Equation 18 may frequently be neglected; if all excitations are considered to arise from the ground state, the oscillator strengths and frequencies are ω_{on} and f_{on} and the sum is taken over only the excited states. Comparison with Equation 19 then shows that the dielectric constant vanishes when Equation 18 is satisfied. This singularity of the dielectric constant at the plasma frequency can be used to determine the plasmon energy when it cannot be evaluated straightforwardly. It is also possible to determine the qualitative effect of interband transitions on the plasmon frequency. In Figures 1(a) and 2(a), the dielectric behavior of a free gas is shown. We have already seen that when the plasmon disper-

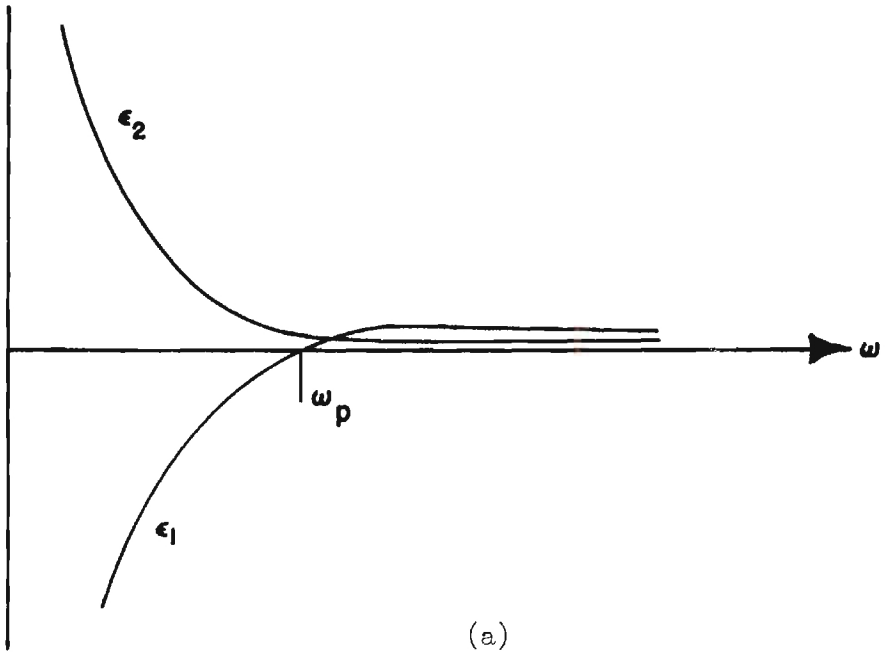

(a)

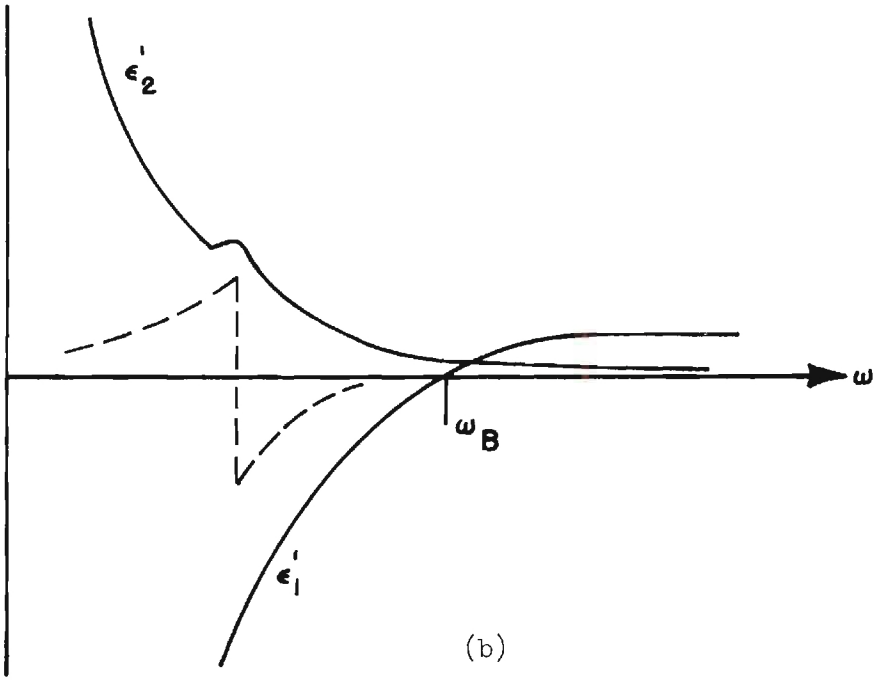

(b)

Figure 1. Dielectric Behavior When Interband Transition Exists Near but Below ω_p.

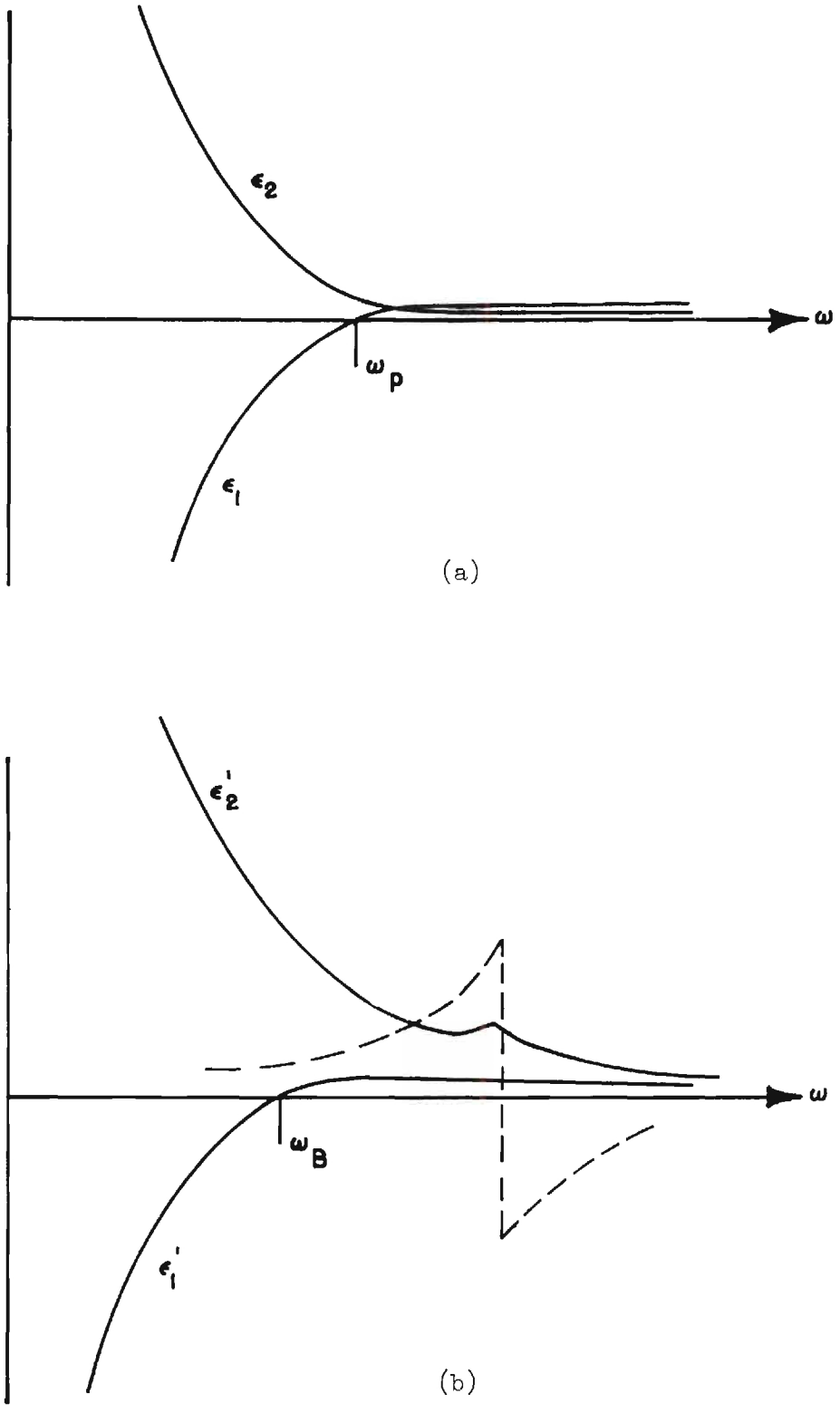

Figure 2. Dielectric Behavior When Interband Transition Exists Near but Above ω_p.

sion relation is satisfied, ϵ_1 will be zero with ϵ_2 small; this locates the plasma frequency as illustrated in the figures. To illustrate the change in the plasmon frequency produced by plasmon interactions with "core" electrons, we consider a single electron bound to an ion core with a natural frequency ω_{on} but responding to the plasmon oscillation at frequency ω_p. The amplitude response of this electron can be described by analogy with the response of a classical oscillator driven by an external force. Thus, if the binding frequency is less than the driving plasmon frequency, the driven oscillator will move out of phase with the plasmon field and will contribute to the dielectric response of the solid as indicated by the dashed curve in Figure 1(b). When this oscillator-like response is added to the free-gas dielectric behavior, the response, ϵ', passes through zero at a frequency greater than ω_p, and thus the plasma frequency is shifted upwards. A similar picture describes the effect of a plasmon interaction with a single-particle excitation of frequency ω_{on} greater than ω_p. In this case, the oscillator response is in phase with the plasmon field and its dielectric contribution depresses the point at which ϵ_1 is zero as illustrated in Figure 2(b). Therefore, in a solid with many electrons bound to the ion cores, the plasma frequency will be decreased below its free-electron value if the majority of oscillator strengths are associated with interband transitions having excitation frequencies greater than ω_p. On the other hand, if the oscillator strengths are associated mainly with transitions having frequencies less than ω_p then the plasmon frequency is shifted above its free-electron value.

The condition $\epsilon = 0$ at the plasma frequency is rarely satisfied in

a real solid because the plasmon behavior is damped at all energies by single-particle excitations and ϵ_2 is thus displaced from zero. The dielectric approach, however, may be used to determine the collective energy losses of a moving charged particle since these losses are reflected in the total energy change in the electric field. Based on this method, Frohlich and Pelzer have shown the bulk plasmon loss probability to be a maximum when the ω-dependent function[55]

$$- \mathrm{Im}(1/\epsilon) = \frac{\epsilon_2}{\epsilon_1^2 + \epsilon_2^2}$$

is greatest. For free-electron gases, the plasmon energies determined from $\epsilon = 0$ and from the maximum in $-\mathrm{Im}(1/\epsilon)$ are the same, but for the more complicated metals, the dielectric energy loss function must be used to more accurately locate the plasmon frequency.

When interband transitions are important in determining the bulk plasmon frequency, the surface plasmon energy is also affected by the single-particle excitations as can be seen by examining the dielectric response. Stern and Ferrell[46] have shown that the condition for a surface plasmon oscillation is $\epsilon(k,\omega_s) = -\epsilon'$, where ϵ' is the dielectric constant of the bounding medium. For the clean surface, $\epsilon' = 1$, so the surface plasmon dispersion relation can be written

$$\epsilon(k,\omega_s) + 1 = 0 \quad \text{or} \quad 2 = \frac{4\pi e^2}{m} \sum_n \frac{f_{on}(k)}{\omega_s^2 - \omega_{on}^2} \quad .$$

This relation accounts for the effect of the periodic potential on the surface plasmon frequency but can not be explicitly evaluated to determine ω_s. The dielectric approach is again helpful as Ritchie[45] has shown that the probability for excitation of a surface plasmon is proportional to

$$- \mathrm{Im}\left[\frac{(1 - \epsilon)^2}{\epsilon(\epsilon + 1)}\right] .$$

Near the surface resonance frequency, ϵ_1 is near -1, so this loss probability locates the surface plasmon energy from the maximum in the function

$$- \mathrm{Im}(1/\epsilon+1) = \frac{\epsilon_2}{(\epsilon_1 + 1)^2 + \epsilon_2^2} .$$

Because the interaction between a transverse electromagnetic wave with a metal's valence electrons is similar to the interaction between these electrons and the plasmon field, a close connection exists between the optical and collective properties of a metal. The system response to the incident charged particle is a density fluctuation of the electrons, so the dielectric constant in Equation 19 describes the longitudinal response of the system. The electromagnetic field of the photons employed in optical investigations is a transverse disturbance, however, so an optical determination of the system response is described by the transverse dielectric constant. In the limit of long wavelengths such

as those describing the collective properties of isotropic or cubic solids, the quite general result[56]

$$\epsilon_{\perp}(0,\omega) = \epsilon_{\parallel}(0,\omega)$$

is valid, so the results of an optical determination of $\epsilon_{\perp}(0,\omega)$ can be used to help interpret the loss spectrum of a charged incident particle traversing that solid since they determine the real and imaginary parts of the dielectric constant and thus the energy loss function $-\mathrm{Im}(1/\epsilon)$, and the surface plasmon loss function $-\mathrm{Im}(1/\epsilon+1)$.

Electron Energy States in a Disordered Crystal

With an understanding of the coupling between collective and single-particle excitations, it is possible to discuss the effects on electronic band structure. This treatment might include a plasmon-phonon interaction, although the influence of this interaction has been suggested to be small in view of the large plasmon energy. The situation we are concerned with, therefore, is a non-periodic ion distribution which varies in time and how the consequent changes in potential disturb the electronic structure of the disordered solid. Rather than attempting to solve the severely difficult mathematical problem concerning electron eigenfunctions and their energy distributions in an irregular potential, we seek only to demonstrate how the thermal disorder affects the plasmon dispersion.

In the classical model employed earlier to obtain the plasmon dispersion relation, harmonically bound electrons were allowed to freely follow an oscillation plasmon field. One might extend this model to in-

clude thermal perturbations on the electron structure by subjecting the electrons to a viscous force which damps the electron response in proportion with its velocity. The characteristics of the electron coupling to the plasmon field might be modified by increased viscous damping to illustrate the effects of thermal disorder in the plasmon dispersion arising from perturbations on the individual electron states.

In this model, the damped harmonic motion is described by

$$\ddot{x} + b\dot{x} + \omega_o x = -\frac{e}{m} E_o \cos\omega t \qquad (22)$$

where b describes the viscous damping proportional to electronic velocity. The solution of this equation is[57]

$$x = -\frac{e}{m} \frac{E_o}{G} \sin(\omega t - \alpha) \qquad (23)$$

where

$$G^2 = m^2(\omega^2 - \omega_o^2) + b^2\omega \qquad (24)$$

and $\alpha = \cos^{-1}\frac{\omega}{G}$. The amplitude of electronic oscillation is well known to display a dependence on the driving frequency and becomes increasingly large as that frequency approaches the natural oscillation frequency. This resonance phenomenon predicted from the inverse proportionality of x to the factor G which depends on the difference between ω

and ω_o.

The behavior of the electron response depends on the magnitude of the damping force as well as on the driving frequency. This is best illustrated through a graphical analysis of x as shown in Figure 3 where the oscillation amplitude is sketched as a function of $\frac{\omega}{\omega_o}$ for a series of progressively larger damping constants. Curve (a) shows the amplitude when there is no damping and when energy is continuously fed into the system. The other curves indicate an increased half-width of the oscillatory response as the damping due to dissipative forces is increased. We also see that the resonant frequency is no longer exactly equal to the natural frequency of the bound electron. Both of these qualitative effects should influence the plasmon excitation spectrum as thermal disorder, corresponding to damping in this model, is increased.

One probable result of the thermal perturbations is easily anticipated; extra energy levels may be introduced into the original energy band structure or existing levels may be shifted from their unperturbed positions because of the changed potential felt by the electrons. This is suggested by displacement of the resonant frequency from the natural response frequency in the damped harmonic oscillator. In the plasmon dispersion relation, some changes in the spectrum of interband transition frequencies which affect the collective motion might occur. These changes are not expected to be significant, however, since there already exists a complex of transitions which are responsible for the original shift of the plasmon energy; the overall composition of excitations in the dispersion relation would therefore not change enough to influence the plasmon energy. The other factor which enters the new spectrum of

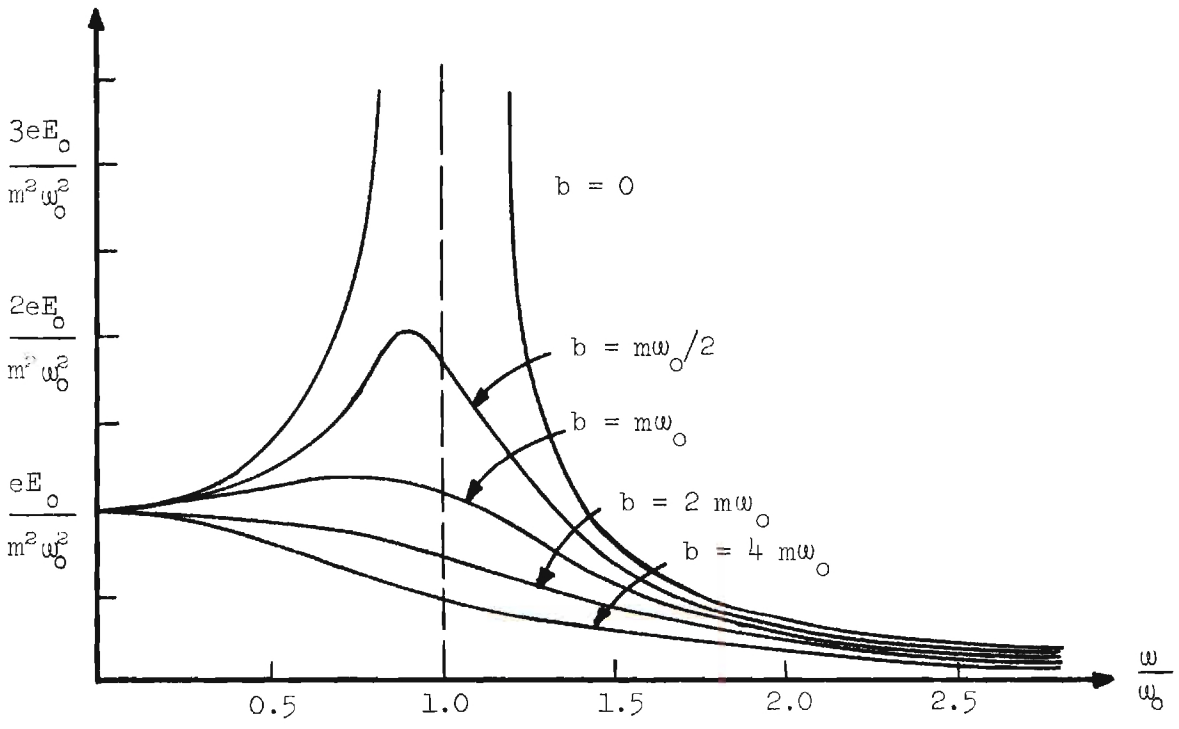

Figure 3. Amplitude of a Driven Harmonic Oscillator Versus the Ratio of the Driving Frequency to the Undamped Natural Frequency. Curve (a) Shows no Damping and Curve (b) High Damping.

single-particle transitions is an increased line width of each energy level; this appeared in the model as an increased half-width of the electronic response to an oscillating plasmon field.

Unfortunately, there is no straightforward way to verify these properties of the energy band structure in a partially disordered solid. In fact, they were obtained only after much theoretical work on the electronic structure of liquid metals had developed the techniques for studies of non-periodic potentials. In Appendix B, a Green's function perturbation calculation is presented in which the difference between the original potential and that in a partially disordered crystal is considered as a perturbation on the original energy level spectrum. In this calculation, the unperturbed density of states is obtained from the imaginary part of the Fourier transform of the Green's function integrated over all momentum space. The Green's function is then generalized to include one term indicative of energy level displacements and another which describes increased line widths of the levels; this extended function is used as a solution of the perturbed crystal Schroedinger's equation. To complete the calculation, the new density of states is determined in terms of the displacement and line widths introduced by the thermal disorder perturbation. These two factors are related to matrix elements of the perturbing potential but since neither the electron wave functions in the disordered crystal nor the explicit form of the perturbing potential are known, only the qualitative effects on band structure can be determined.

The main conclusions drawn from the analysis are that both displacement and line broadening of the energy levels in the ordered system

occurs as disorder is introduced by thermal agitation. Since the energy level displacements are not expected to affect the plasmon behavior, only the line broadening needs to be appropriately included in the plasmon dispersion relation. This line broadening, ΔE, in the energy of a level and is related to the lifetime of a state in which an electron occupies that level through the Uncertainty Principle

$$T\Delta E \cong \hbar \ .$$

The lifetime T is inversely proportional to a parameter Γ which describes the probability that the excited state will make a transition to a lower energy state. Through this decay probability, the effect of energy level broadening in a disordered system can be included in the plasmon dispersion relation.

In time-dependent perturbation theory,[58] the probability that a system makes a transition from the state m to the state n is given by

$$a_{nm}(t) = e^{i\omega_{nm}t}$$

where $\hbar\omega_{nm} = E_n - E_m$. In order that this excited state decay, it is necessary that an exponential decay factor $e^{-\Gamma_{nm}t}$ be included in a_{nm} so that

$$a_{nm}(t) = e^{-i\omega_{nm}t}\, e^{-\Gamma_{nm}t} = e^{-i(\omega_{nm} + i\Gamma_{nm})t} \ .$$

Thus, line broadening, system lifetime and other decay effects can be

considered in any interaction by adding an imaginary contribution to the excitation frequencies of the transitions involved.

The half-widths of the broadened energy levels must be included in any expression involving excitations between the energy levels. For metals in which the collective excitations are coupled to the energy band structure, the plasmon dispersion relation has been found as

$$1 = \frac{\omega_p^2}{n} \sum_n \frac{f_{on}}{\omega^2 - \omega_{on}^2} \quad . \tag{18}$$

Since the thermal disorder causes increased decay probabilities in the interband transition spectrum, the plasmon decay probability is probably also increased. We have already seen that these effects can be accounted for by replacing ω_{on} by $\omega_{on} + i\Gamma_{on}$ and ω by $\omega + i\Delta$ in Equation 18, where Δ is indicative of the addition to the plasmon decay probability which would arise from broadening of the single-particle energy levels. These terms have been inserted in the following plasmon dispersion relation which therefore describes plasmon excitations in heated samples when there is strong coupling between the plasmons and single electrons:

$$1 = \frac{\omega_p^2}{n} \sum \frac{f_{on}}{(\omega + i\Delta)^2 - (\omega_{on} + i\Gamma_{on})^2} \quad . \tag{25}$$

That the imaginary part of each side of this equation must be equal requires

$$0 = \sum_{n} \frac{f_{on}(\omega\Delta - \omega_{on}\Gamma_{on})}{(\omega^2 - \omega_{on}{}^2)^2} \quad . \tag{26}$$

From this relation, it is seen that increases in the Γ_{on} are necessarily accompanied by decreases in the plasmon decay probability Δ in order that the equation still hold. It is noted that there are disorder contributions to the decay probability of excited single-particle states other than those affected by thermal motion. Crystal dislocations, impurities, and similar imperfections also decrease the lifetimes and influence the plasmon dispersion through Γ'_{on} decay contributions. These effects do not significantly change with increased sample temperature and hence can be observed in the plasmon excitation spectra obtained at room temperature. Thus, as the sample temperature is raised, the linewidths of the levels in the energy band structure due to thermal disorder increase and the plasmon half-widths increase in turn.

This prediction is derived from theoretical results concerning both disorder effects on band structure and the electron-plasmon interaction in metals. Because of the proximity of the 3d- and 4s-electron energy levels in transition metals, a strong electron-plasmon interaction involving the 3d-electrons is likely to exist and the plasmon dispersion relation at elevated temperatures would be given by Equation 25. This relationship is therefore appropriate for an investigation of the effects of disorder on the electron excitation spectrum obtained at high temperatures from transition metals copper and nickel.

In the next chapter, the experimental apparatus used to obtain the data necessary to test these observations is described. Next, the

question of whether the plasmon oscillations involve an interaction with the 3d- and 4s-electrons or involve only the free-gas of 4s-electrons is answered. Then, the plasmon excitation spectra are obtained at elevated sample temperatures to study the effects of a perturbed electronic structure on the plasmon dispersion.

CHAPTER III

EXPERIMENTAL METHODS

Collective excitations in solids have been discussed in Chapter II in terms of backscattered electron energy losses and optical data. The discrepancies in previously reported energy loss data emphasize the need for surface characterization; the optical constants of a metal are also known to be affected by formation of a dielectric layer at the surface.[59] An ultrahigh vacuum, low-energy electron diffraction system was therefore used in this study since the low pressure capabilities of the system could be used to maintain surface conditions for extended periods of time and since the electron optics could be used to generate electron energy distribution curves along with LEED patterns. Furthermore, this instrumentation could be conveniently combined with optical apparatus to obtain the optical constants of samples with known surface conditions in the LEED system. The instrumentation used in this experiment to obtain energy distributions of electrons emitted from the sample consisted mainly of a three grid electron optics package which could be used as a spherical retarding field analyzer with differentiation of the current transmitted to the display screen. In the optical measurements, light derived from a grating monochromator was focused onto the sample and the reflected radiation was monitored with photomultiplier tubes placed in two view ports on the LEED chamber. The apparatus and techniques employed to obtain the energy loss and optical reflectivity data are described in this chapter; in addition, the sample preparation

and cleaning procedures are discussed.

Apparatus and Procedures

Ultrahigh Vacuum System

In view of the sensitivity of the energy loss and optical data to surface conditions, it was desirable to maintain a chamber pressure on the order of 10^{-10} Torr throughout these measurements. This ultrahigh vacuum was required because a clean surface can adsorb a full monolayer of a foreign gas with a unit sticking probability in one second at 10^{-6} Torr. The LEED system was therefore designed for routine operation at pressures near 2×10^{-10} Torr. The system was constructed mainly from 304 stainless steel and employed either metal-to-metal or metal-to-glass seals on all flanges and vacuum feedthroughs in order that it be totally bakeable. Conventional vacuum techniques as discussed by Roberts and Vanderslice[60] and by Brunser and Batzer[61] were employed in all stages of handling the LEED system and samples studied.

Vacuum pressure in an experimental system is limited to several factors, the most important of which are virtual leaks due to backstreaming vapors from diffusion pumps and desorption of gases from surfaces inside the system. Backstreaming vapors were eliminated in the LEED system through use of ion-gettering pumps to produce a clean, high vacuum with cryogenic sorption pumps employed as roughing pumps to produce the vacuum (10^{-2} Torr) required for starting the ion pumps. In the present system, a 80 liter/second ion pump was used to maintain the pressure in the sample chamber, a 40 liter/second pump was used in the gas delivery system, and a 8 liter/second pump was used in the roughing manifold. During the course of the experiment, the vacuum system was equipped with a titanium

ion-sputtering pump which was used to further lower the chamber pressure. The schematic diagram of the vacuum system in Figure 4 shows the pumps, valves, and gas handling system.

The procedure for attaining a vacuum in the system when starting from atmospheric pressure is outlined below. With all valves open and the Granville-Phillips leak-valve controller removed, the system was exposed to one of the two cryogenic pumps already chilled to liquid nitrogen temperature. When the LEED chamber pressure was reduced to approximately 500 microns, the first sorption pump was closed and the second used to obtain a system pressure of five microns so that it was possible to start the ion pumps. The sorption pumps were then closed, and, after the system had attained a pressure in the 10^{-7} Torr range, resistance heating elements located near the vacuum plumbing and a shell-like oven placed around the exposed chamber were activated. Gas desorption from inner parts of the system was reduced by baking the entire system at 250° C for eight to ten hours. Pressure sensitive relays were incorporated into the oven power supplies so that whenever the pressure in the system rose above 5×10^{-6} Torr, the ovens were automatically turned off. After the system was baked out, the pressure was generally 5×10^{-9} Torr and dropped to 5×10^{-10} Torr within 48 hours. A nude ionization gauge located on the far side of the sample chamber from the pumping throat was used to determine the pressure.

During the sample cleaning procedure and during exposures of the cleaned sample to oxygen, oxygen and argon gases were admitted from spectroscopically pure one-liter glass flasks to the sample chamber through pressure-regulated leak valves. The 40 liter/second pump was turned off

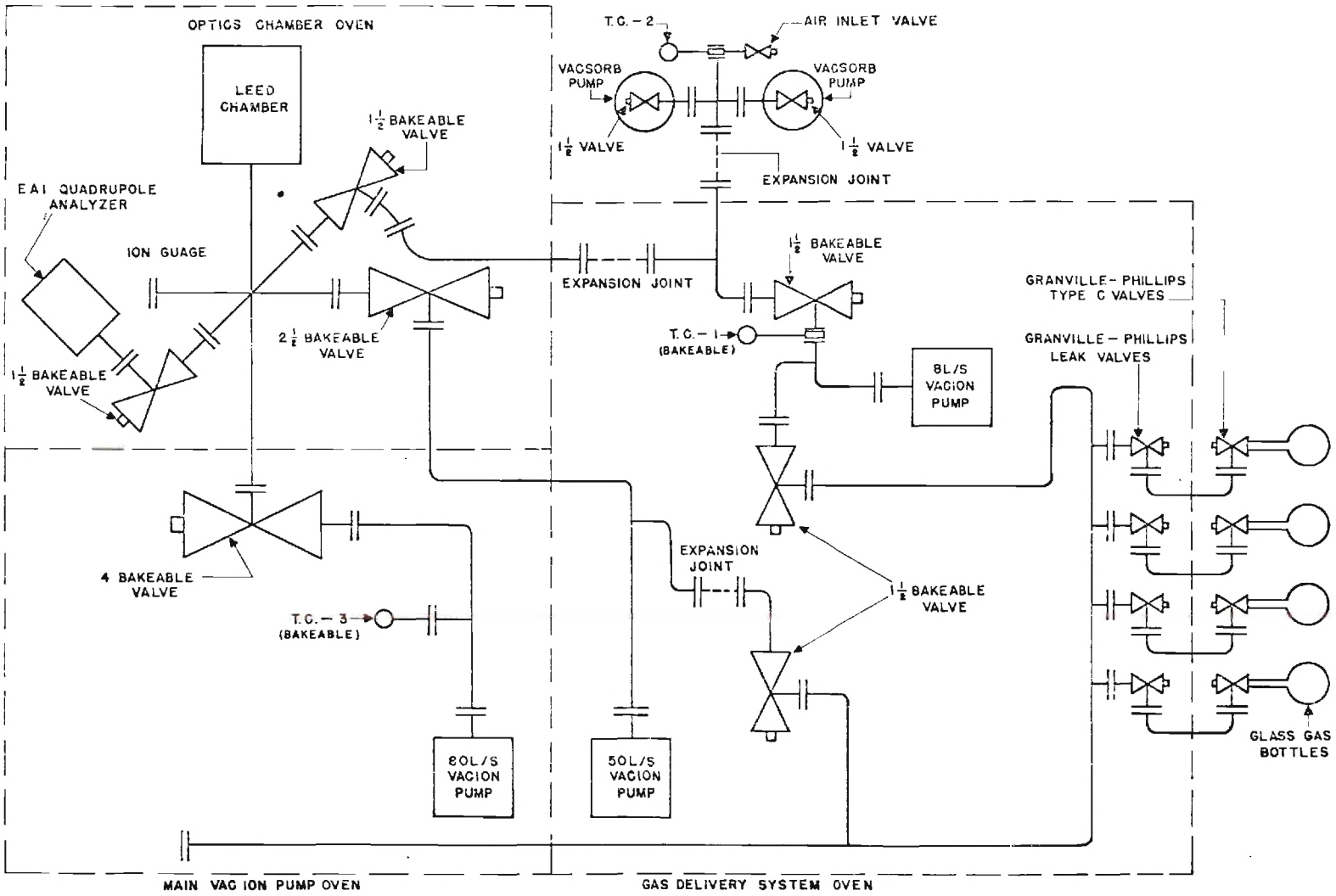

Figure 4. Schematic Diagram of LEED Vacuum System.

and the 80 liter/second pump was throttled during the oxygen exposures in order to maintain a continuous flow of gas in the chamber at any pressure desired between 5×10^{-9} and 5×10^{-6} Torr. When argon was used in cleaning the sample, the necessary quantity of gas was admitted into the chamber with all the pumps turned off. Any other gas could be introduced into the system through a third gas inlet assembly. Furthermore, through use of multiple leak-valve controllers, a mixture of gases could be admitted into the system.

The vacuum system included an Electronic Associates, Inc. quadrupole residual gas analyzer which was used to monitor the background pressure and to test the purity of the gases admitted into the chamber. It was found that the light gas hydrogen not adequately retained in the ion-pump plates and carbon monoxide released from the optics filaments constituted about 75 per cent of the background pressure at 5×10^{-10} Torr.

Electron Optics

The electron optics of the LEED apparatus consisted of an electron gun, fluorescent screen, and grid assembly. The basic geometry and electronics of the optics are illustrated in Figure 5. Beam voltages supplied by a Keithley Model 240-A power supply were continuously variable between 0 and 1200 volts but were digitally selected for operating convenience. A bariated nickel cathode was heated using a Kepco Model CK-3M dc current source which could be operated in either a constant current or constant voltage mode to control the emission current. The electron beam was accelerated toward the sample by a grounded drift tube which passed through the tungsten mesh grids and was focused at different beam voltages by a variable potential on a lens element at the front

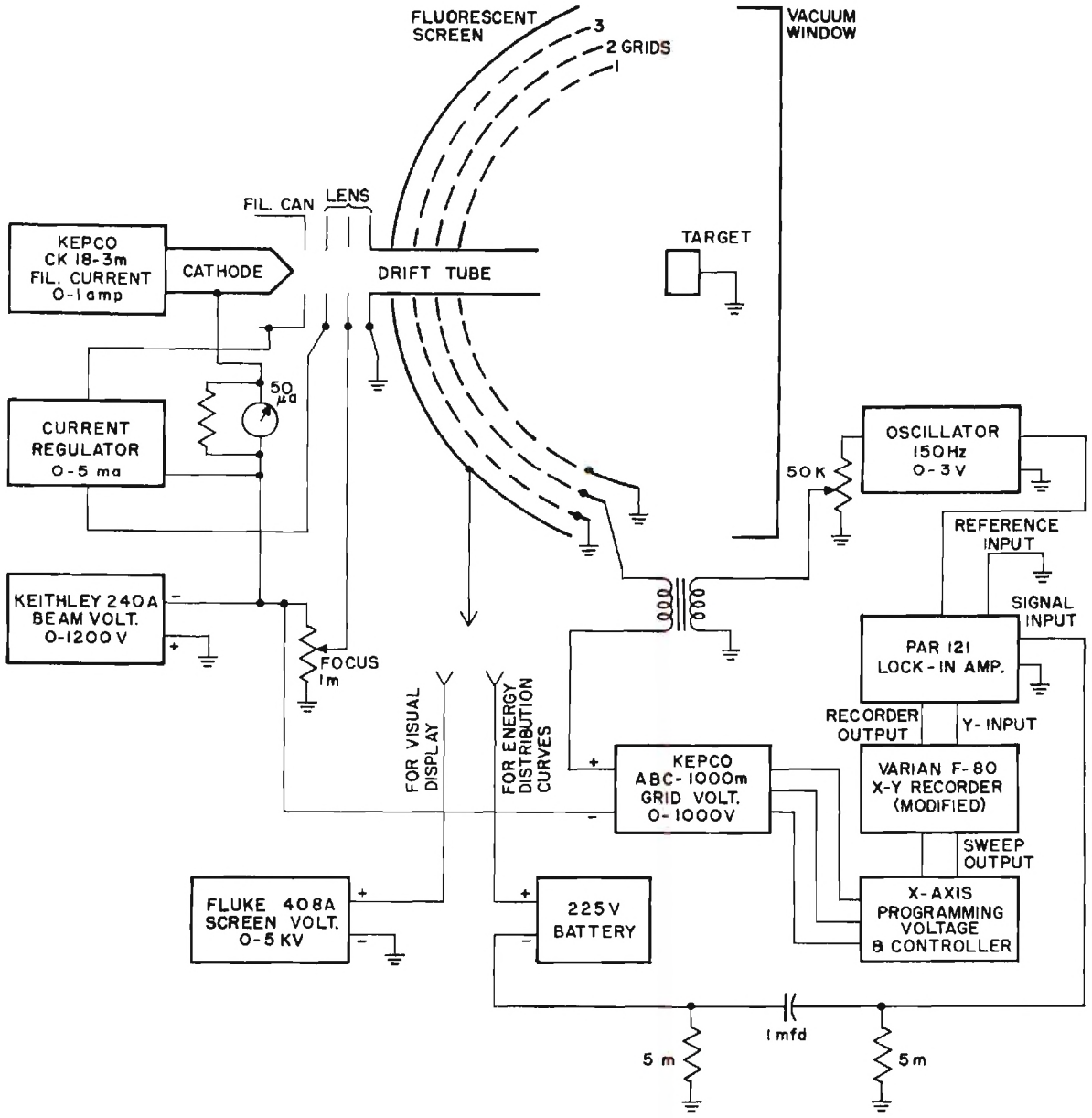

Figure 5. Schematic Diagram of LEED Optics and Electronics for Obtaining Diffraction Patterns and Electron Energy Distribution Curves.

of the drift tube. Because the backscattered electrons did not have energies capable of exciting the fluorescent screen, they were "post-accelerated" onto the screen by operating the screen at a positive 5000 volt potential supplied by a Fluke Model 408 high voltage supply.

Because of the high strength of the magnets in the ion pumps, the low-energy electron beams in the sample chamber were deviated from their free-field paths unless compensation was made for the stray magnetic fields. Two Helmholtz coils with adjustable currents were placed outside the diffraction chamber and used to bring the electron beams into alignment. The compensated fields were arranged so that when the sample was removed from the beam path, the electron beam was not deflected from an aligned path. When the sample was replaced, the resulting diffraction patterns could be photographed through the chamber window. The grid nearest the target was grounded to shield the region about the target so that it remained free of electric fields which otherwise disturbed the electron trajectories. The grid next to the fluorescent screen was also grounded to give a field-free region between it and the screen. The potential on the middle grid could be adjusted to suppress electrons having energy less than that of the primary beam. Since most of the electrons are reflected inelastically from the crystal and contain no diffraction information, the middle or suppressor grid potential was used to pass only the electrons with the primary electron energy when diffraction patterns were of interest.

The diffraction patterns characteristic of low-energy incident electrons have features which result from two as well as three-dimensional effects. In terms of the usual reciprocal space and Ewald con-

structions,[62] diffraction conditions are satisfied whenever the Ewald sphere intersects elements in the reciprocal space appropriate for the scattering centers involved. One-dimensional periodic adsorption on a sample surface is represented by a set of sheets in reciprocal space which are perpendicular to a preferred adsorption direction. The Ewald sphere intersects cones in reciprocal space and produces streaks in the diffraction pattern orthogonal to the direction of adsorption.

When scattering is produced by a two-dimensional array, another set of sheets appropriate to that array is added to the previous one-dimensional reciprocal space. The reciprocal space of a two-dimensional structure is thus composed of rods whose spacings and positions reflect those same properties of the scattering array. Diffraction takes place when the Ewald sphere intersects the rods common to both sets of sheets.

In the construction of reciprocal space for scattering from a three-dimensional periodic structure, another set of sheets is added to the two-dimensional reciprocal space. This produces a lattice of points which reflects all the symmetries and spacings of the scattering crystal. With low-energy electrons, diffraction from a crystal involves more than the single surface layer, so the rods of the reciprocal space appropriate for an explanation of diffraction patterns for low-energy electrons are modulated in intensity. This explains the appearance in LEED patterns of spots which are "forbidden" in pure three-dimensional diffraction and the absence of spots expected in pure two-dimensional diffraction.

LEED patterns reveal surface contamination in two ways: features other than those predicted for the clean surface arise from adsorbates

with a periodic structure, while a disordered adsorbate gives increased background in the pattern. From the previous discussion, it is seen that an adsorbate ordered in parallel rows on a crystal surface produces a diffraction pattern representative of that adsorption structure on the clean crystal substrate. This pattern can sometimes be used to identify the particular surface contaminant. Of course contamination is not always revealed in the LEED patterns, but when they are used along with measurements of the secondary electron distributions, it is possible to determine if a surface is free from contamination.

Energy Loss Measurements

The energy loss measurements were made by varying the potential on the middle grid linearly from the negative cathode potential toward ground. The current collected by the fluorescent screen was composed of all electrons with energy greater than E′ where E′ was the difference between the retarding potential on the middle grid and the cathode potential. This curve was not very sensitive to the fine structure in the backscattered current; instead, the energy derivative of this curve, the number of electrons with a particular energy, was desired as a function of their energy. This curve was obtained through an ac differentiation method described by Leder and Simpson.[63]

In the differentiation technique, a small sinusoidal signal, typically one volt peak-to-peak at 150 Hz, was superimposed on the retarding potential to modulate the current transmitted to the screen. That component of the screen current at the same ac frequency and phase as the modulating signal represented the energy derivative of the transmitted current and was proportional to the number of electrons backscattered

from the sample with a particular energy.[63] The small ac voltage was taken from the reference output of a Princeton Applied Research Model JB-4 lock-in amplifier and was added to the retarding grid voltage through an audio transformer. The screen current was collected and the ac component preamplified by a low-noise Princeton Applied Research CR4-A amplifier; the current was then sent to the JB-4 lock-in amplifier where only that part of the current with the same frequency and phase as the original modulating signal was selected. In the latter stages of the experiment, the signal/noise ratio was increased by a factor of 100 by replacing the CR4-A and JB-4 amplifiers with a Princeton Applied Research Model 121 lock-in amplifier which contained its own low-noise preamplifier. The lock-in amplifier generated a dc voltage proportional to the magnitude of the in-phase current, the derivative of the total current curve, which was sent to the Y-axis of an X-Y recorder.

By coupling the carriage displacement of a Varian Model F-80 X-Y recorder to the retarding potential, the time-sweep mode of the recorder was used to control the retarding potential so the energy distribution curves were automatically obtained as a function of electron energy. This connection was accomplished by adding a potentiometer to the X-axis drive mechanism; a resistance signal from the potentiometer was used to program the voltage output of a Kepco Model ABC 1000M power supply and this voltage was used as the retarding potential. Provision was also made for manual adjustment of the grid voltage and voltage sweep rate so the recorder trace could be concentrated on any particular portion of the loss curve. The curves could be taken at energy sensitivities of 0.5, 5, 10, 15, 20, 25, and 50 ev per inch of recorder trace.

The energy loss curves generated with this equipment were affected by an inherent energy resolution characteristic of the retarding electrostatic grid system as discussed by Simpson.[64] This resolution was realized as an energy half-width added to the natural structure in the loss curves and arose because the retarding field produced by the grid system was not perfectly spherical about the sample. Thus, electrons radially reflected from the sample had a momentum component parallel to the retarding equipotential surfaces. The retarding potential affected only the normal component of electron momentum so electrons may not have traversed the retarding region even though their energy was larger than the suppressor potential. The resolution was also energy-dependent as illustrated in Figure 6 where the energy half-width of the elastically scattered primary peak is shown as a function of the primary energy. The relative resolution $\Delta E/E$ was approximately two per cent and had to be considered whenever half-widths of structure in the loss curves were analyzed.

Optical Measurements

In order to exploit the close relationship between the optical and collective properties of solids, optical reflectivity measurements were also made on the copper and nickel samples. The equipment used to obtain the optical constants was designed to cover the largest possible energy range and also to be compatible with the existing LEED system. The upper energy limit, 11.8 ev, was imposed by the transmission characteristics of the lithium fluoride windows on the LEED chamber, and the lower limit, 1.65 ev, was imposed by the response characteristics of the photomultiplier tubes employed. Extension of these measurements to

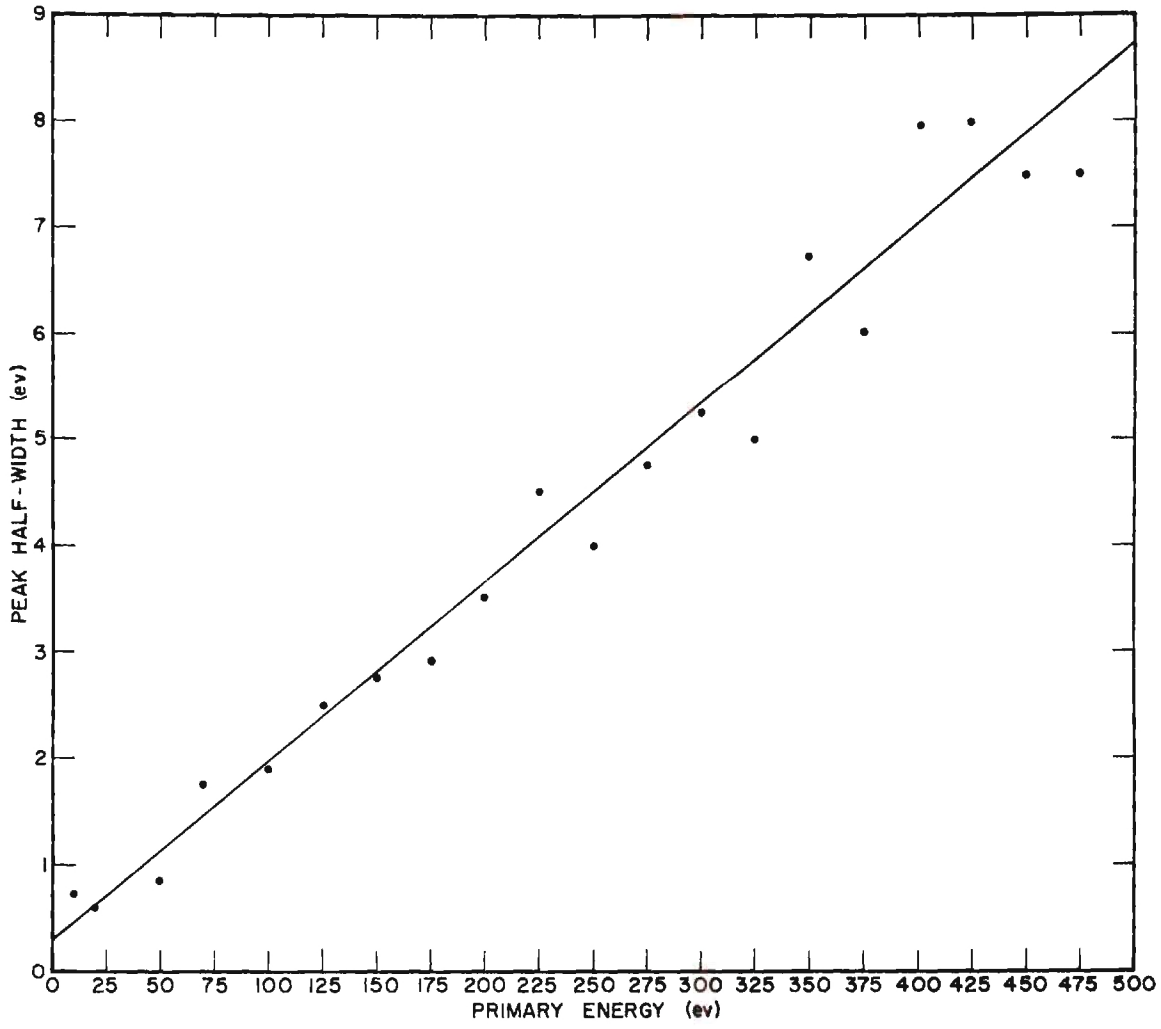

Figure 6. Energy Resolution of Electron Optics as a Function of Electron Energy.

energies higher than 11.8 ev would require either thin-film windows to replace the LiF windows or differential pumping for windowless operation. To make the measurements at energies much lower than 1.65 ev would require photo-diode-like detectors and infrared light sources. Fortunately, the purpose of the optical studies could be satisfied within the bounds of the apparatus as described.

The experimental apparatus shown in Figure 7 produced a monochromatic beam of light which was focused onto the sample and reflected through each of the view ports on the LEED chamber to obtain the reflectivity of the sample at two angles of incidence. A LiF pile-of-plates polarizer was used to produce radiation polarized either normal or parallel to the plane of incidence when desired. The light source was a water and air-cooled, low-pressure spark discharge in hydrogen gas which gave light from the infrared to below 1000Å. This source was manufactured by the McPherson Instrument Corporation and was mounted directly onto the entrance arm of the monochromator. In order to maintain as low a pressure as possible in the monochromator, the light source was equipped with a cam operated sliding plunger which sealed against the entrance slit jaws on the monochromator thus limiting the gas leak to an opening of the slit width times six millimeters. The spark discharge which excited the hydrogen gas in the lamp was obtained from a McPherson Model 720 power supply. The spark was provided when a 0.0048 microfarad capacitor discharged between two tapered tungsten rods connected in parallel with the capacitor. The gap between the rods was adjusted to give a spark repetition rate of 6.5 kilocycles per second. This spark then passed through the hydrogen-filled capillary in the lamp to produce the hydrogen molecular spectrum from 1050Å to 8000Å. To improve the spark

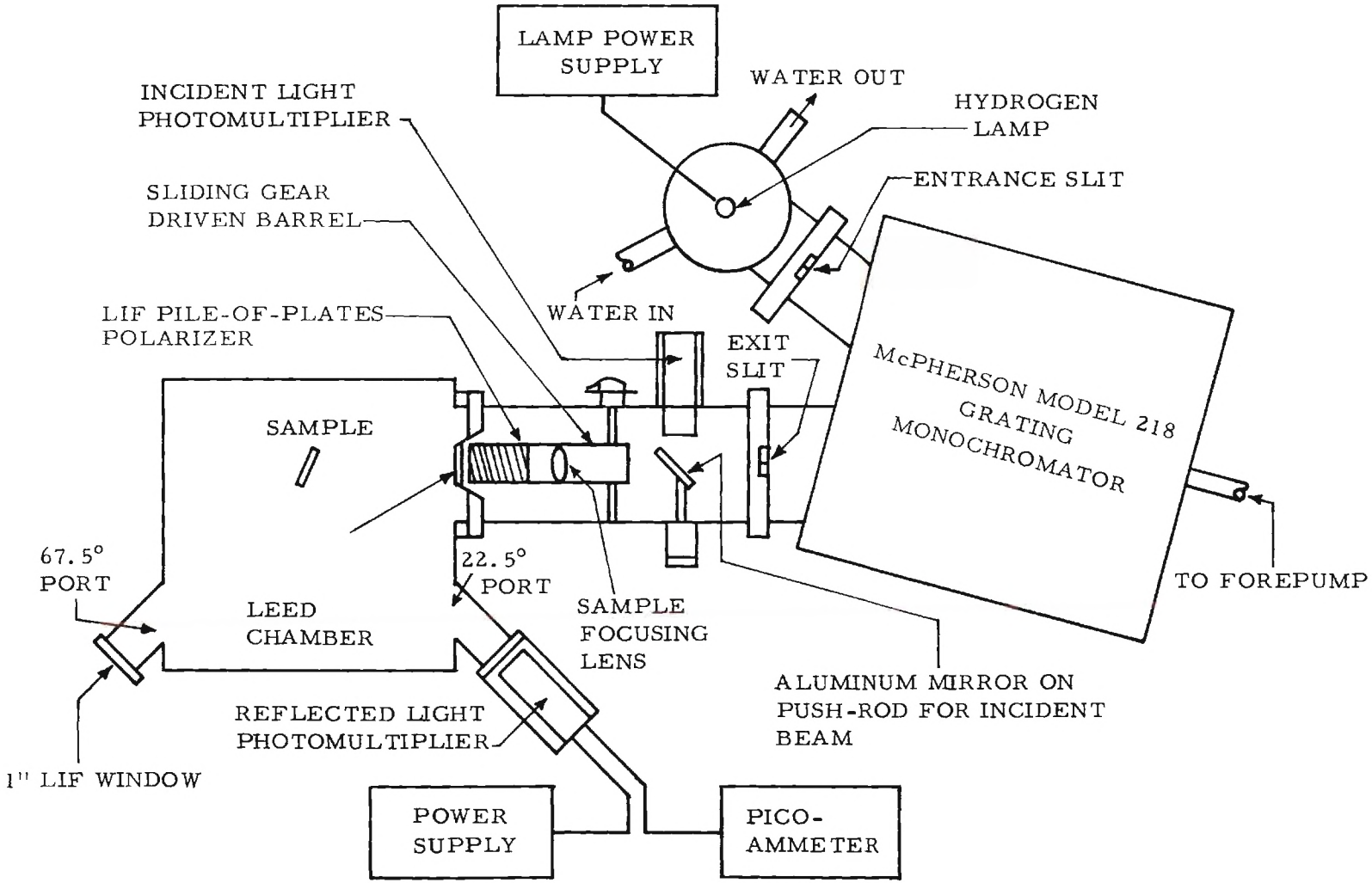

Figure 7. Optical Apparatus as Attached to LEED System.

stability, the gap between the tungsten rods was irradiated with a quartz mercury lamp and was swept continuously with a jet of compressed air.

The monochromator was also manufactured by the McPherson Instrument Corporation and employed a plane grating to monochromatize the light from the entrance slit. An unconventional two-mirror and grating system in which the entrance and exit beams were crossed was employed to give minimum off-axis conditions at the collimating and focusing mirrors. To further reduce the optical aberrations, the mirrors were formed with aspheric focal lengths. The grating chosen for the monochromator was a Bausch and Lomb replica with 600 lines per millimeter with the grove faces inclined at $2^{\circ}35'$ to the surface. This angular setting made the angle of incidence equal to the angle of reflection for the 1500Å wavelength in the first order and thus concentrated the first order of reflected light in this wavelength region. Other gratings are available which can be interchanged directly in this system to give monochromatic light at wavelengths up to 160,000Å. The mirrors and their gratings were overcoated with magnesium fluoride to increase their efficiency below 1700Å and to retard oxidation of the aluminum surfaces. Because of atmospheric absorption of wavelengths below 2000Å the instrument was evacuated using a two-stage, mechanical pump. To minimize the remaining absorption, the optics were purged with hydrogen gas prior to an investigation since this gas is fairly transparent to its own radiation. The cam seal at the gas entrance slit permitted the pressure in the chamber to be held at 200 microns while a hydrogen pressure of 2 millimeters was used in the lamp with a slit width of 0.010 inch.

The light beam from the monochromator was partially reflected into a 9529B EMI photomultiplier tube used to monitor the light incident on the sample. The undeflected beam passed through a LiF lens which had been ground from a rectangular plate using standard lens-maker techniques to a plano-convex form with a 5.5 centimeter radius of curvature. This lens was mounted in a gear-driven barrel so that its position could be changed to produce a beam of parallel rays from the exit slit. Since the index of refraction of the lens changed so rapidly in the shortest wavelength region, a dial on the gear-driven housing was calibrated from the lens equation[65]

$$\frac{1}{f} = (n-1)\left(\frac{1}{r_1} - \frac{1}{r_2}\right),$$

so that the lens focal point could be positioned exactly on the exit slit of the monochromator at each wavelength. In this equation, n is the index of refraction at a given wavelength, f is the focal distance, and r_1 and r_2 are the radii of curvature of the lens.

A 9698QB EMI photomultiplier tube was used to detect the radiation reflected from the sample through LiF windows placed in the view ports on the LEED chamber. The tube was held in a solid aluminum housing to eliminate stray light and to insure that the same relation always existed between the tube cathode and the rest of the apparatus. In order to eliminate the effects on the light beam reflected from the aluminum mirror at the "incident" tube and passed through the LiF lens and windows on the LEED chamber, the tube responses were calibrated at each wavelength.

This was accomplished for both exit windows and their respective housings by placing the housings and windows opposite the entrance window on the LEED chamber at a distance equal to that when the tube was in the reflected position and determining the ratio of signals from the reflected and incident tubes. The sample reflectivity was obtained by comparing this ratio with that ratio found when the sample intercepted the light beam and reflected it to either the 22.5° or 67.5° viewport. In this manner no indirect comparisons of currents or reference mirrors were used so the resulting photomultiplier tube calibration was exact.

Since the photomultiplier tube responses were restricted below 2000Å, the entrance face of the incident light tube and the outsides of the viewport windows were coated with sodium salicylate by spraying a solution saturated in methyl alcohol onto those surfaces. In the presence of radiation shorter than 3000Å, this phosphor fluoresced at 4400Å, a wavelength to which both tubes were especially sensitive. It was important to position the photomultiplier tubes in their housings on the windows in exactly the same position for calibration and for measurements since the phosphor coatings were not uniform. If this was not done, different tube positions changed the amount of light received by the photocathode or the area of the cathode on which the light fell.

In passing through the optical system the light beam was severely attentuated so that the signal intensity was often near the dark current level in the 9698QB photomultiplier tube. Phase-sensitive detection of the reflected signal was employed to eliminate this source of error. Similar detection of the incident signal was not necessary as the dark current in that tube was always three orders of magnitude less than the

signal current. In this technique, the light beam was chopped at 30 Hz by electrically interrupting the power to the discharge lamp power supply, and a phase-sensitive lock-in amplifier, Princeton Applied Research Model 121, was used to detect the in-phase component of the signal from the reflected photomultiplier tube. A voltage signal in phase with the lamp discharge was taken from the capacitor bank in the power supply and provided the reference signal for the phase-sensitive detector. This correlation technique achieved an extremely high signal/noise ratio and eliminated all errors due to the background currents.

It was desirable to obtain the reflectivity data in as little time as possible since gaseous adsorption onto the sample surface affected the optical constants in an unpredictable manner. An automated method for obtaining the ratio of reflected and incident signals was therefore developed. The voltage output of the current meter used to measure the incident photomultiplier tube response and the lock-in amplifier output were first averaged over five seconds to eliminate high frequency noises arising from fluctuations in the discharge lamp intensity. The "reflected" signal was then divided by the "incident" signal and that ratio was plotted on an X-Y recorder versus the photon wavelengths which were swept at 50 Å/min. The signal averaging and division were performed using a Systron Donner Model 3500 Analog Computer incorporating a Model 3732P electronic division circuit which was adjusted for an output accurate within ± 0.25 per cent. A schematic of this measurement apparatus is illustrated in Figure 8. Using this technique, sample conditions were maintained constant throughout the measurements, dark current effects were eliminated, and the task of directly reading photomultiplier currents was abolished.

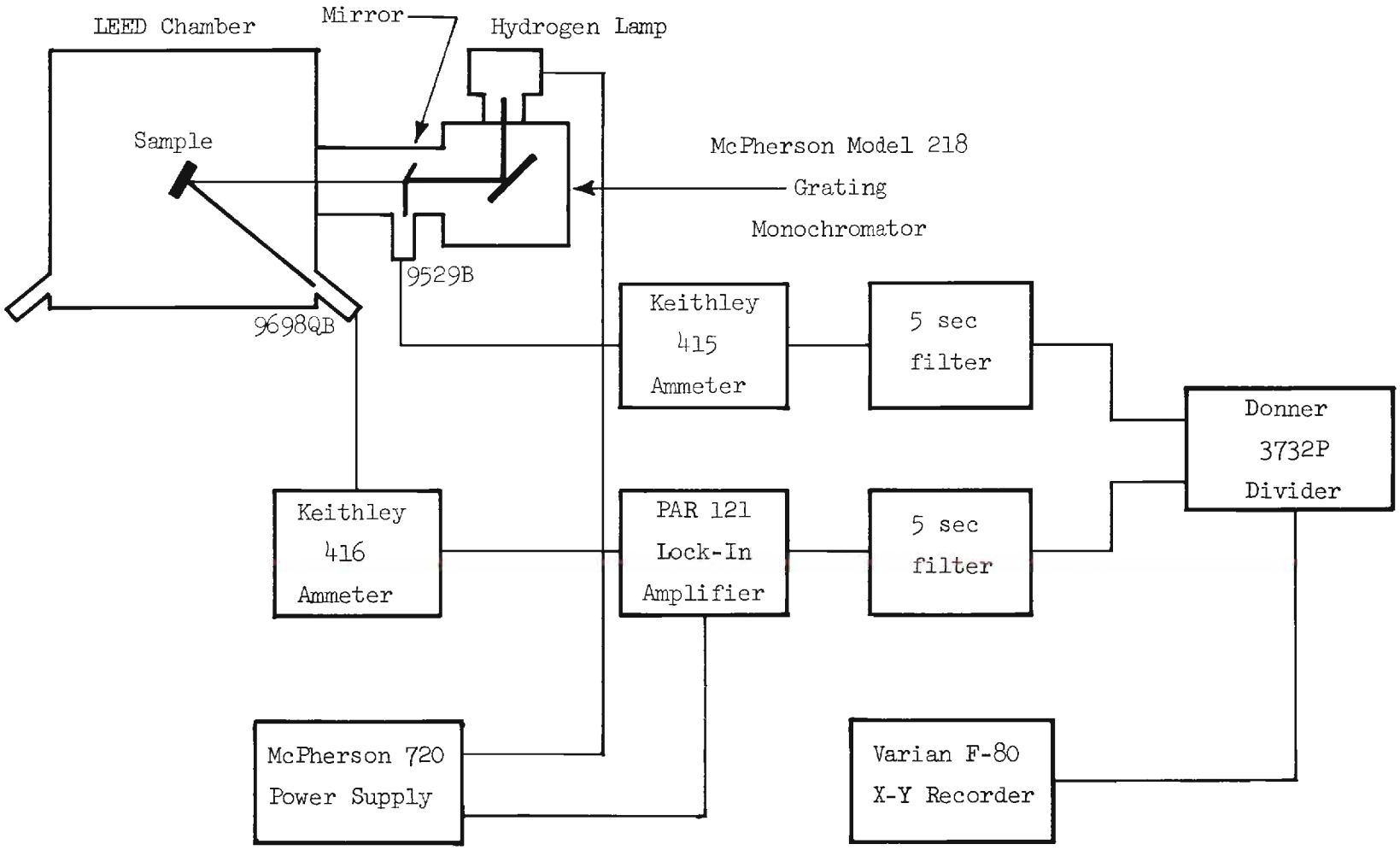

Figure 8. Schematic Diagram for Obtaining Optical Reflectivity Data.

The analysis of the reflectivity data to obtain the optical constants n and k was made using a Burroughs B-5500 computer program similar to that mentioned by Hunter[66] and is discussed in Appendix C. The technique started from given values for n and k and calculated the reflectivity at the two angles of incidence for that point and other points in the n-k plane surrounding the starting point. The point which gave the smallest error between the calculated and measured reflectivities was chosen as a new starting point and the procedure was repeated until the starting point gave the smallest error. That point was taken to give the correct values for n and k. The initial starting point in the n-k plane was determined from a graphical method for finding approximate values for n and k from reflectivity measurements. This analysis consisted of comparing isoreflectance curves calculated at 22.5° and 67.5° from a computer analysis of the Fresnel equations over a substantial range of n and k values. The intersection of the isoreflectance curves determined the starting n-k point for each set of measured reflectivities. In this analysis, the photon beam was assumed completely unpolarized although reflection from the grating in the monochromator did introduce a small degree of polarization.

Sample Preparation and Cleaning Procedures

Sample Preparation

Considerable efforts were made to obtain well-oriented crystals with smooth, defect-free surfaces in view of the effects of surface irregularities on LEED results and optical reflectivity data. Conventional cutting and polishing methods on soft crystals such as copper introduce crystal damage several microns below the surface. Attempts to remove

this damaged volume by etching frequently destroy the smooth surface and require that the crystal be cut again.

In this study, damage to the copper and nickel crystals was minimized by employing the acid cutting and polishing techniques described by Young and Wilson.[67] The copper crystals were cut from single crystal bars of 99.999 per cent purity using the acid string saw seen in Figure 9(a). A 90 per cent nitric acid cutting solution was fed onto a reciprocating ten mil stainless steel wire which was lowered through the crystal at a rate consistent with the removal of copper by the acid solution. The appropriate cutting rate was one inch per sixteen hours. To facilitate mounting of the crystal on the sample holder, two grooves, approximately 15 mils wide by 30 mils deep, were cut on opposing edges of the sample.

Even though the crystals were cut from oriented bars, orientation after cutting was necessary to guarantee that the desired lattice face existed at the crystal surface. Orientation corrections were made from Laue back-reflection x-ray diffraction patterns taken with the sample held in a goinometer which could be mounted directly onto the acid polishing wheel seen in Figure 9(b). A solution of concentrated hydrochloric acid saturated with cupric chloride was used as the polishing solution to remove the undesired bulk and to produce a smooth surface on the copper crystals. When necessary, the cupric ion solution was replenished during the polishing by adding a 30 per cent hydrogen peroxide solution to the polishing mixture. A 10-15 minute polish was usually required to correct the surface orientation.

After the acid polish the copper crystal was rinsed in hydrochloric acid and distilled water and was electropolished to remove any

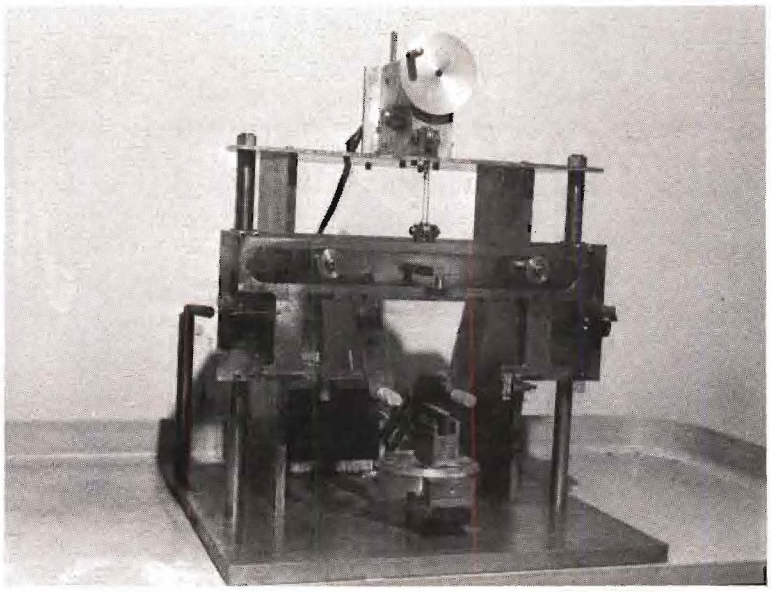

(a)

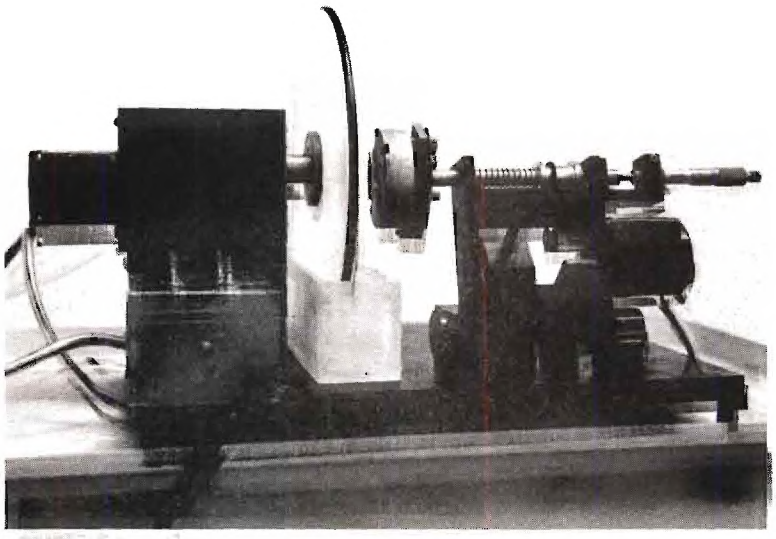

(b)

Figure 9. Photographs of (a) Acid String Saw and (b) Acid Polishing Wheel.

remaining disturbed surface layers and to produce a mirror-smooth, highly reflective surface. The electropolishing solution was 50 per cent phosphoric acid in distilled water. During the polishing process, care had to be taken to prevent etching and pitting of the surface. Pitting was reduced by stirring the solution to remove the gas evolved to the surface and to agitate the viscous polishing layer at the crystal surface. The sample was then rinsed in distilled water and placed in the LEED chamber.

The nickel crystal was obtained from Research Crystals, Ltd. and was of 99.999 per cent purity; it was noted that carbon formed the major part of the impurities in the sample. Mounting grooves were cut in opposing edges of the crystal with the acid string saw using a 5 per cent hydrochloric acid in nitric acid cutting solution. Attempts to chemically polish the crystal resulted in a surface with visible contours; preferrential etching was also unsuccessful as the surface became rough after sufficient etching to remove even 0.1 millimeter of damaged crystal. To obtain the flat surfaces desired for both LEED and optical measurements, it was necessary to mechanically polish the crystal first using 400 grit metallographical polishing paper and next using a suspension of aluminum oxide in water on a rotating felt disk. During this procedure, the crystal was held in an especially designed holder which could be mounted on an x-ray goniometer and the desired crystal face aligned parallel to a polishing surface. In this manner, orientation corrections determined from x-ray Laue photographs were made, and a surface parallel to the desired crystallographic plane was obtained.

Because of surface damage to the nickel crystal which occurred during the mechanical polish, extensive electropolishing was required

to produce a defect-free undamaged surface. A 5 ampere anode current passing through a 50 per cent sulfuric acid solution resulted in a highly reflecting, flat surface suitable for the optical studies. The polishing mechanism for nickel involved vigorous gas evolution but produced no surface etch pits. Immediately after the electropolish the nickel crystal was rinsed in distilled water and mounted on a sample holder in the LEED system with platinum wires placed in the grooves along the upper and lower edges.

The stainless steel sample holder was mounted on a vacuum manipulator flanged to the LEED chamber. The crystals were heated indirectly by radiation from a hot tungsten filament which was insulated from the holder by a ceramic tube which had a small opening in the side toward the crystal. A chromel-alumel thermocouple imbedded in the holder was used with a potentiometer to measure the temperature. The crystal could be heated to a maximum temperature near 500°C by the radiation from the filament, but for temperatures up to 1000°C, an adjustable potential, 0-500 volts, was applied between the filament and the holder. The resulting electron bombardment was capable of producing these higher temperatures.

The sample holder was attached to a universal motion, vacuum feedthrough which could make 15° angular tilts with the vertical and could be rotated through 360° except when inhibited by heated and thermocouple wires. The sample could also be moved one and one-half inches vertically and one inch laterally from the axis centerline. These degrees of freedom in the LEED chamber allowed positioning of the sample for both energy loss and optical analysis.

Sample Surface Conditions

After the sample was placed in the LEED chamber and the system pressure reduced into the 10^{-10} Torr range, the surface was cleaned by cycles of argon ion bombardments and high temperature annealings. In the cleaning procedure, argon gas was admitted to the sample chamber through leak valves to a pressure of 5×10^{-5} Torr and the surface bombarded with positive argon ions to remove adsorbed gas layers from the crystal surface. The bombardment gun generated ions and by means of several grids, focused and accelerated them toward the target. The ion energies could be adjusted from 0 to 390 ev to clean the surfaces without causing excessive crystal damage; an ion current monitor was available to estimate the ion current density of the beam.

The copper samples were annealed at 250°C for ten hours during the system bakeout and then at 850°C for five hours. The initial argon bombardment used 390 ev ions with a sample current of 6×10^{-7} amp/cm^2. The surface was then annealed at 500°C for one-half hour. This procedure was repeated until no surface contamination was seen in the diffraction patterns. Similar procedures were used to clean the nickel surface except the annealing temperature was 850°C. The clean surface was defined by two criteria. First, the diffraction patterns for the clean surface were required to show sharp reflections, high contrasts, and no diffraction features other than those predicted for the clean surface. Second, since LEED patterns depend on periodic structures and hence do not always reveal surface contaminants, the energy loss data which are very sensitive to surface conditions were also used to define the surface conditions. The surface was not accepted as clean until the

energy distributions showed no changes upon additional ion bombardment or extended annealing. During investigations of the clean surface the system background was monitored with the residual gas analyzer, consisted mainly of carbon monoxide and hydrogen and was always less than 5×10^{-10} Torr. Under these circumstances, the copper surface could be kept clean about eight hours; the nickel surface remained clean only four hours but a ten minute flash at 800° C gave clean surface results.

CHAPTER IV

RESULTS AND DISCUSSION

In previous chapters, the effects of thermal disorder on characteristically scattered electrons have been discussed, and apparatus which can be used to obtain the desired data concerning elementary excitations in a partially disordered crystal has been described. In this chapter, experimental evidence of a strong electron-plasmon interaction in transition metals is presented, and the effects of thermal disorder on the inelastically scattered characteristic electrons are demonstrated. The collective excitations were investigated through LEES and optical reflectivity measurements; high temperature LEES data were obtained to examine the effects of increasing crystal disorder on the plasmon excitations.

Copper

Energy distributions of electrons reflected from (100) and (110) faces of copper single crystals and optical reflectivity data from a (100) face were obtained using the techniques described in Chapter III. Characteristic energy loss peaks in the energy distribution curves were interpreted as arising from many-particle collective excitations and single-particle interband transitions; optical data helped identify the collective characteristic energy losses. These data show that plasmon excitations in copper are strongly coupled to the electronic structure through high-energy single-particle excitations which depress the bulk

plasmon energy from a free-electron value of 36 ev to 19.5 ev. The surface plasmon energy was similarly affected by single-particle excitations as it was reduced from the free-electron value of 25 ev to 7.5 ev. The data and their interpretation in terms of interacting individual and collective excitations are presented in the remainder of this section.

Characteristic Energy Losses

Energy loss spectra of electrons backscattered from clean copper (100) and (110) surfaces were obtained for primary electrons with energies between 30 and 350 ev. An energy loss distribution curve typical of those obtained from both the clean Cu (100) and (110) surfaces, characterized by LEED patterns in Figures 10(a) and 11(a), and which was obtained by bombarding a clean (100) surface with 190 ev primary electrons is seen in Figure 12. The curve is characterized by three regions; I, the elastically scattered electrons usually assumed to appear in the LEED patterns; II, the characteristic loss region representing primary electrons which have undergone losses characteristic of the sample studied; and III, the secondary electrons emitted from the sample. The energy losses in Figure 12 occur at 9.0, 19.5, 27.5, and 39 ev. The measured value of the low-lying characteristic loss depended on the energy of the bombarding electrons because the resolution of the electron energy analyzer decreases with increasing energy of the backscattered electrons. The decreasing resolution causes this peak to shift toward a nearby, more intense peak as the incident electron energy increases. This instrumental effect was reproduced in a graphical, computer program using parameters appropriate for the analyzing grid system, and it was found that the most accurate value for the low-lying loss is 7.5 ev. It

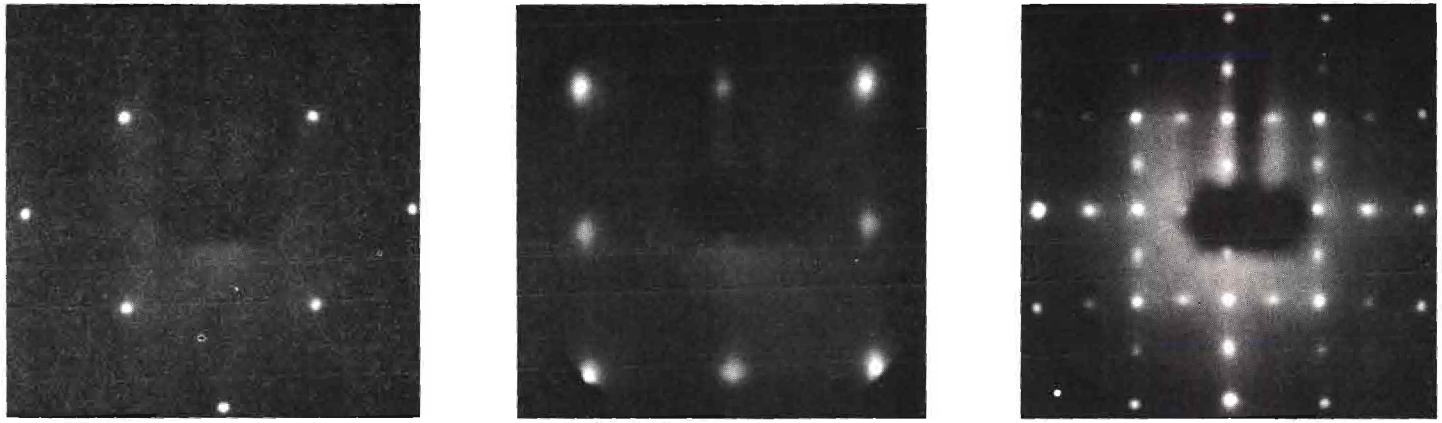

Figure 10. LEED Patterns of Copper (100) Surface for Successive Stages of Oxygen Adsorption. (a) Shows Clean Surface at 190 Volts, (b) Primitive Adsorption at 64 Volts, (c) Further Adsorption at 124 Volts.

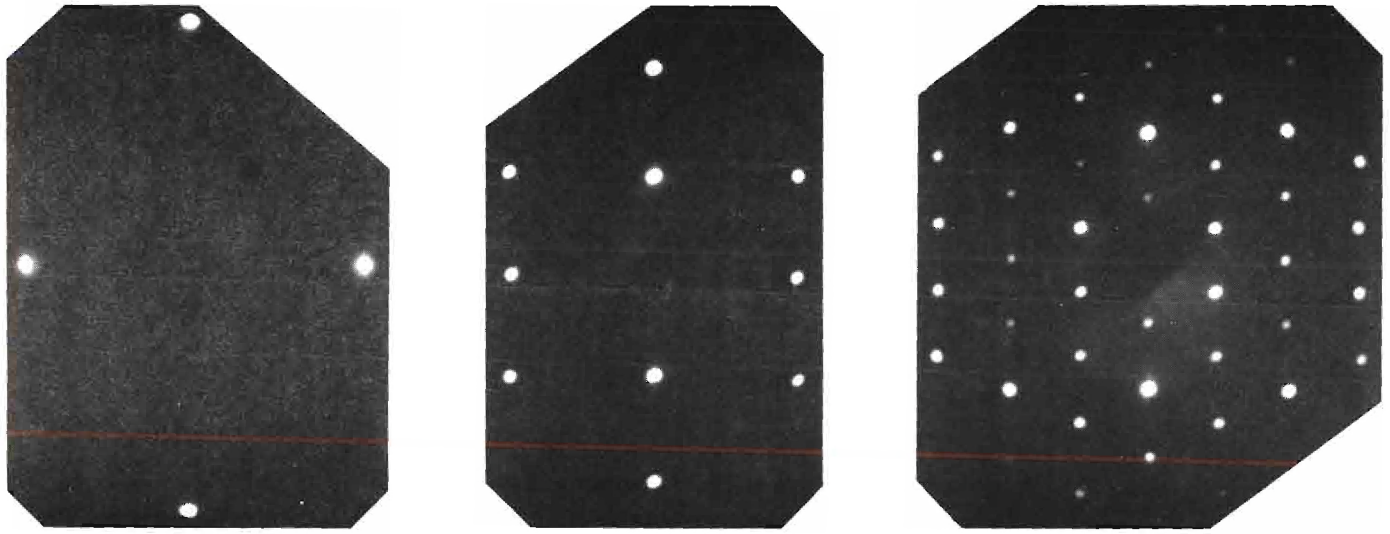

Figure 11. LEED Patterns of Copper (110) Surface for Successive Stages of Oxygen Adsorption. (a) Shows Clean Surface at 63 Volts, (b) Initial Adsorption at 73 Volts, (c) Further Adsorption at 69 Volts.

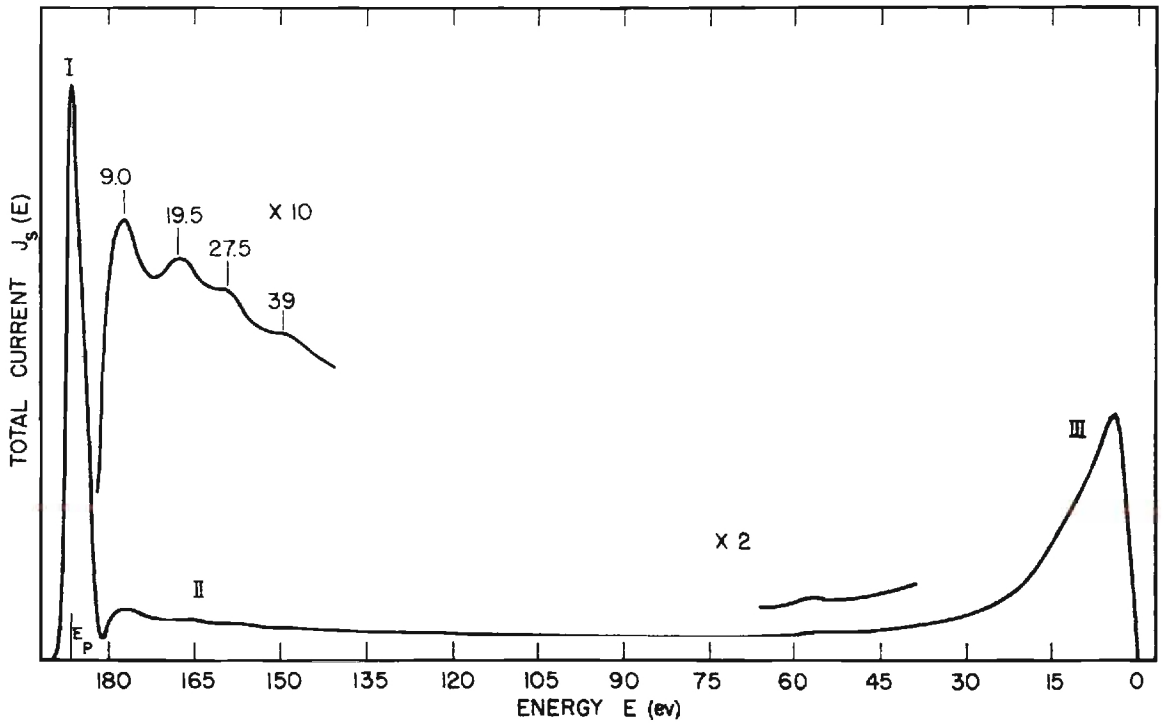

Figure 12. Electron Energy Distribution for 190-Volt Primary Electrons Incident on Clean (100) Copper Surface.

should be noted also that this value was observed in energy loss spectra taken with 50 ev primary electrons.

In view of the small energy distinction between 4s- and 3d-electrons in copper, the plasmon excitation energies cannot be directly predicted from either the free-electron or the collective theory, Equations 7 and 18, thus requiring that the surface plasmon loss peak be identified from its intensity dependence on the surface dielectric constant. As mentioned in Chapter II, Stern and Ferrell[46] showed that the clean surface loss decreases in probability when the dielectric constant at the surface is affected such as by adsorbing oxygen onto the crystal, and they predicted that another loss, the modified surface plasmon excitation would appear in the loss spectrum with a lower energy. These predictions concerning plasmon behavior have been verified by Powell and Swan[47] in their investigations of the energy loss spectra of Al and Mg. Therefore, to make the identification of the surface loss in copper, the clean surface was exposed to increasing amounts of oxygen to affect the surface dielectric constant and reduce the surface plasmon loss probability.

In order to insure well-defined scattering surfaces, LEED patterns were obtained at all stages of the experiment to accompany the energy loss and optical data. A clean (100) copper surface diffraction pattern is shown in Figure 10(a) for comparison with the patterns produced after exposure of this surface to oxygen. Oxygen adsorption was first observed after a 5×10^{-5} Torr-min exposure at room temperature, and the resulting primitive (1 x 1) structure is shown in the 64 volt LEED pattern of Figure 10(b). Further exposure, totalling 2×10^{-4} Torr-min, to oxygen pro-

duced the diffraction pattern shown in Figure 10(c). This pattern can be explained by superimposing diffraction patterns resulting from the two possible orientations of a (2 x 1) structure on the substrate unit mesh. Annealing at approximately 500° C resulted in sharper spots and higher contrast in the diffraction pattern. Exposure of the clean (110) surface, diffraction pattern of Figure 11(a), to 1×10^{-6} Torr-min of oxygen followed by annealing at 200° C produced the diffraction pattern shown in Figure 11(b). When this (2 x 1) surface structure was heated to 400° C and the sample exposed to 5×10^{-4} Torr-min of oxygen, the (6 x 2) structure seen in Figure 11(c) was observed. These oxygen adsorption structures are consistent with those reported by Simmons, Mitchell and Lawless.[68]

Exposure of the clean copper surfaces to increasing amounts of oxygen did affect the characteristic energy loss spectra as predicted by the dielective theory. The increased dielectric constant at the surface resulted in a decrease in intensity of the loss at 7.5 ev as shown in Figures 13 and 14 for the two surfaces studied. The intensity decreases in the top three curves in each figure correspond to the oxygen coverages indicated by the diffraction patterns in Figures 10 and 11. In view of Stern and Ferrell's predictions concerning the intensity dependence of the surface plasmon loss on surface conditions, this loss was considered to correspond to the excitation of a surface plasmon. The amount of oxygen adsorbed at the surface was not sufficient to produce a modified surface plasmon loss peak, although this peak could have been hidden under the elastically scattered primary peak which was broadened because of the resolution of the gun and grid system. The

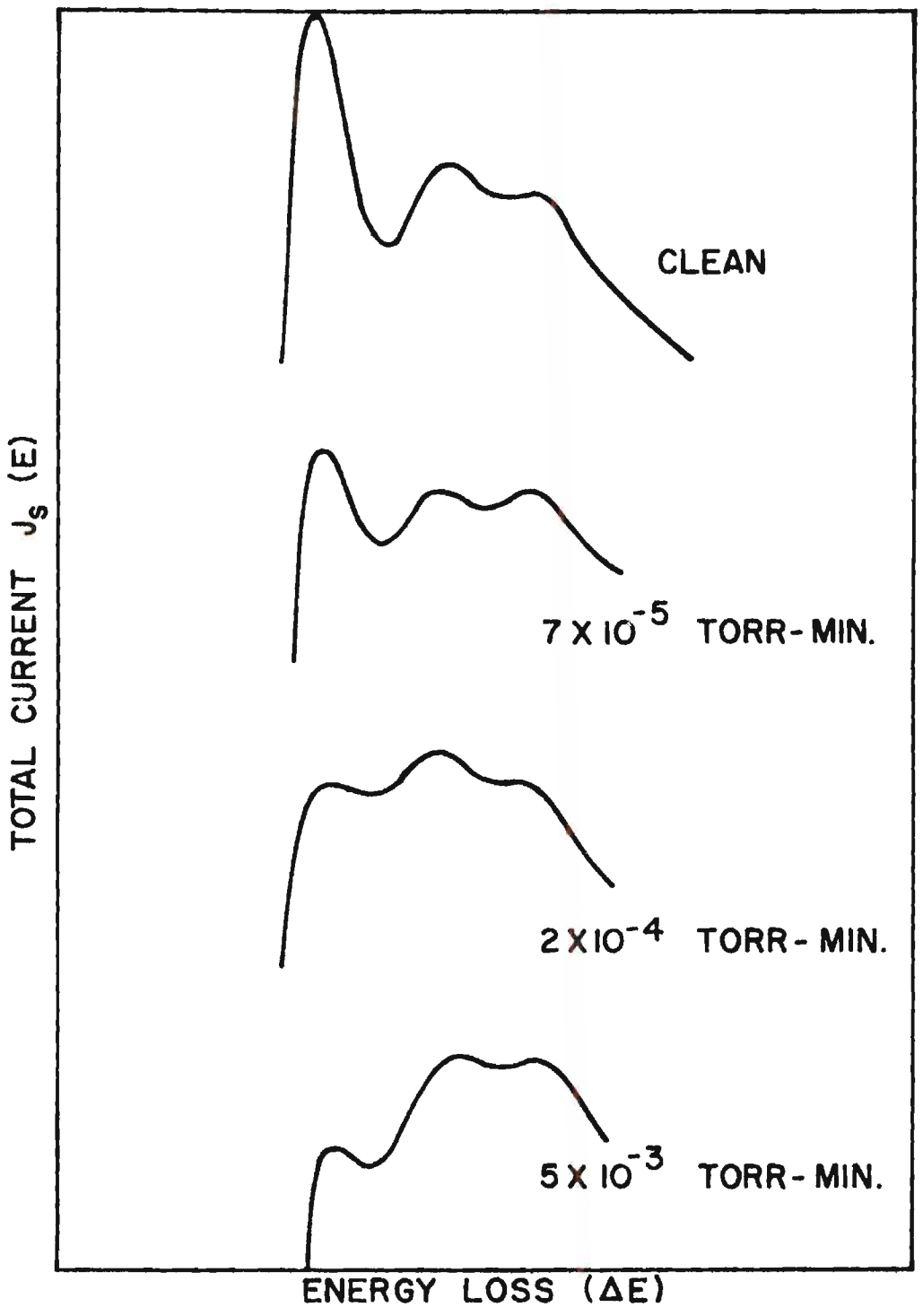

Figure 13. Variation of Surface Plasmon Intensity with Increased Oxygen Exposure on Copper (100) Surface.

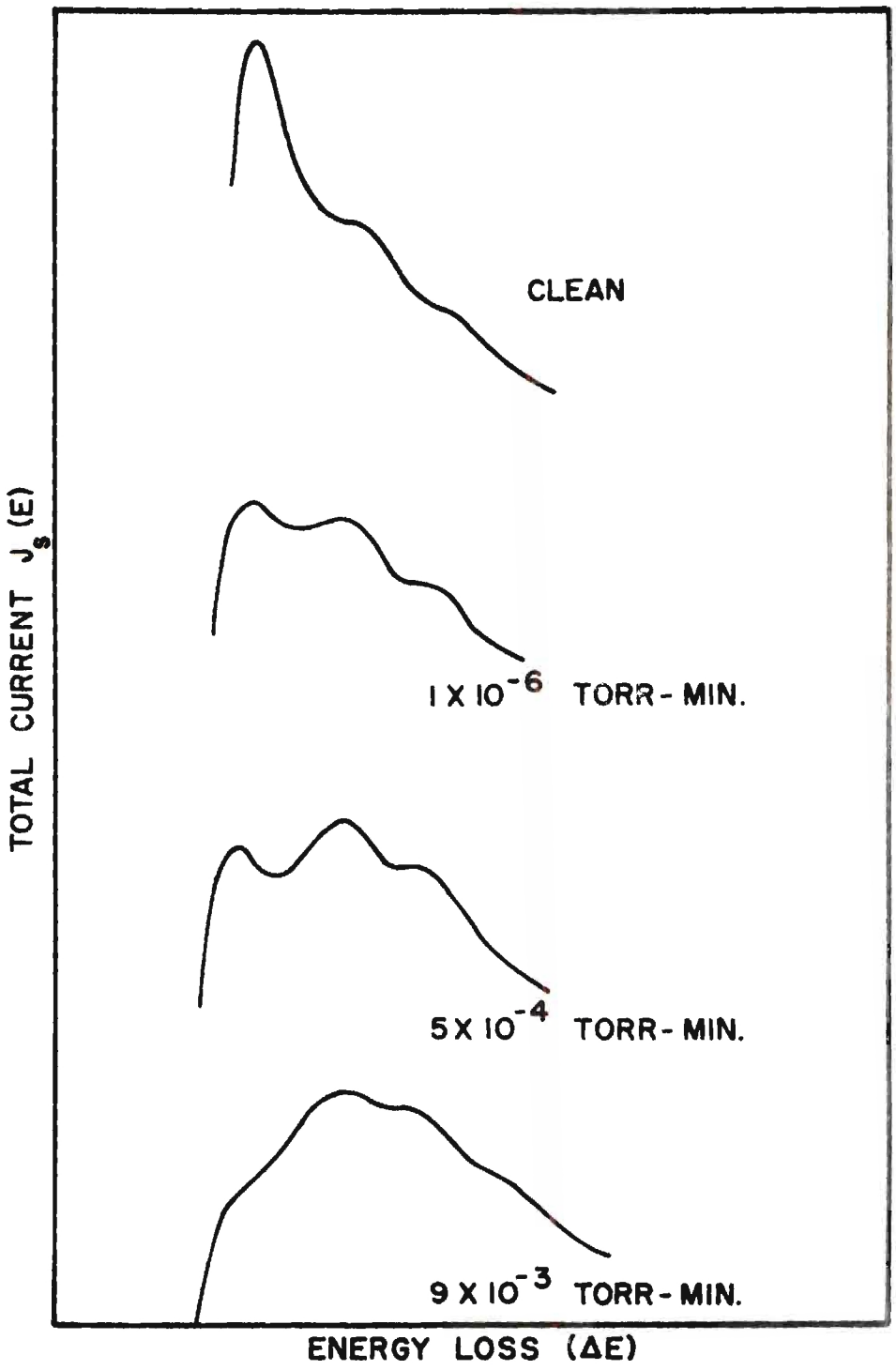

Figure 14. Variation of Surface Plasmon Intensity with Increased Oxygen Exposure on Copper (110) Surface.

bulk plasmon excitation is not affected by surface conditions and could be responsible for either the 19.5 or 27.5 ev loss peak. On the basis of copper alloy data discussed later, the 19.5 ev peak was identified as the bulk plasmon excitation.

Two peaks representing electrons which had excited combinations of surface and bulk and two bulk plasmon resonances were observed at 27.5 and 39 ev. The 39 ev loss was difficult to separate from the spectrum background and was resolved only with primary energies between 100 and 200 ev. The 27.5 ev loss was observed to have an unexpectedly high intensity compared to the bulk and surface losses so it might not be composed of only combined bulk and surface losses. Beeman and Friedman's x-ray absorption data[69] indicate that interband transitions in copper are expected at 18 and 27 ev. Thus, a 27 ev single-particle transition may have contributed to the loss at that energy in view of its intensity. In this case, the collective and individual excitations are not completely distinguished as the loss peak is probably due to both an interband transition and a combined bulk and surface plasmon excitation.

The characteristic energy losses observed in this study and the interpretations of previous investigations are grouped by energy in Table 1. The interpretation given by the respective authors is indicated in the table title. The 4.5 ev loss in that table arises from an interband transition involving the excitation of a d-electron to the vacant levels above Fermi energy, and was seen only at the lower primary energies where the optics resolution was greatest. In the optical data discussed later, this transition is accompanied by a loss at 2.5 ev which is always hidden in the energy loss data by the primary peak but did

Table 1. Characteristic Energy Losses Observed by Various Authors. (The identified losses are denoted by: a = bulk plasma loss, b = interband transition loss, c = surface plasma loss).

Present Work	2.5[a]		4.5[b]	7.5[c]			19.5[a]	27.5[a,b,c]	39.0[a]
Stephenson[70] (Leder, Mendowlitz and Marton)[8]		3.5[b]		7.5[b]		14.0[b]	23.0[b]		34.0[b]
Robins & Swan[2]			4.5[b]	7.6[c]			19.1[a]	27.3[a,b,c]	
Ehrenreich & Philipp[5]	2.5[b]		5.0	7.5[a]	10.5		20		
Viatskin[71]					11.5[b]		23.0[b]		34.5[b]
Cruezberg[72] (Raether)[73]	2.0[b]	3.8		7.5[a]	10.7		19.0	27.0	
Powell[74]			4.4[b]	7.2[c]			19.9[a]	27.1[a,b,c]	

contribute to the asymmetry of that peak. The only agreement with Stephenson's x-ray data,[70] which Leder, Mendlowitz and Marton[8] used for comparison with characteristic energy loss spectra, is with the 7.5 ev loss. This energy has already been interpreted as a surface plasmon excitation, and since the observed intensity dependence on surface conditions can not be expected for an interband transition, this agreement is considered accidental. It is of course possible that a single-particle excitation does contribute to the intensity of the loss peak, but the main contribution is from the surface plasmon loss. Viatskin's perturbation calculations[71] on inelastic scattering of primary electrons by interactions with the lattice electrons predict and interband transition at 11.5 ev. This value is close to a loss resolved by Creuzberg,[72] but Viatskin's other calculated losses do not agree with the observed loss spectrum. Thus, agreement between the characteristic losses and interband transitions is observed for the 4.5 and 27 ev losses. Interband transitions at 7.5 and 18 ev may constitute part of the collective loss intensities at 7.5 and 19.5 ev, since at these energies the interband transitions can not be distinguished from collective excitations.

The true secondary electrons with energies less than 50 ev seen in region III of Figure 12 are usually considered to be electrons which were originally bound in the crystal but were emitted from the solid after some inelastic process. The quantum theory of the production of secondary electrons has been reviewed by Hachenberg and Brauer,[75] while the experimental aspects and general features of the curve have been described by Dekker.[76] The shape of this part of the energy loss curve is generally the same for all metals, but is sensitive to surface prop-

erties and impurities in the body of the crystal.

Superimposed on the secondary end of the curve in Figure 12 is a peak representing electrons with energies distributed about 58 ev. This peak represents Auger electrons ejected from the 3d band because of electron transitions from the same 3d band to 3p states which have been ionized by the incident electrons. Based on the distribution shape of Auger electrons ejected after neutralization of low-energy incident ions, Hagstrum[77] has investigated the density of states in copper. This analysis required a detailed knowledge of the electronic transition probabilities for the levels involved, the perturbing effects of the ionized level, and transport properties of the excited electrons, problems which have recently received considerable attention.[78,79] Part of this interest arises because Auger electrons with energies characteristic of the low-lying levels in a foreign element can be seen in the secondary emission spectra and thus used to identify that contaminating element.[79] These electrons are most easily observed when higher energy (1 to 3 kev) electrons are used for the ionizing beam.[80]

Optical Studies

The results of optical reflectivity measurements from a clean (100) face of a copper single crystal made at two angles of incidence for photon energies between 1.65 and 11.8 ev are shown by the solid curves in Figures 15 and 16. The surface conditions for these data were determined by LEED patterns and secondary electron distributions. Similar data were obtained for the surface after exposures to 5×10^{-5} and 2×10^{-4} Torr-min of oxygen. The diffraction patterns describing the adsorption structures are those seen in Figures 10(b) and 10(c), respectively, and corres-

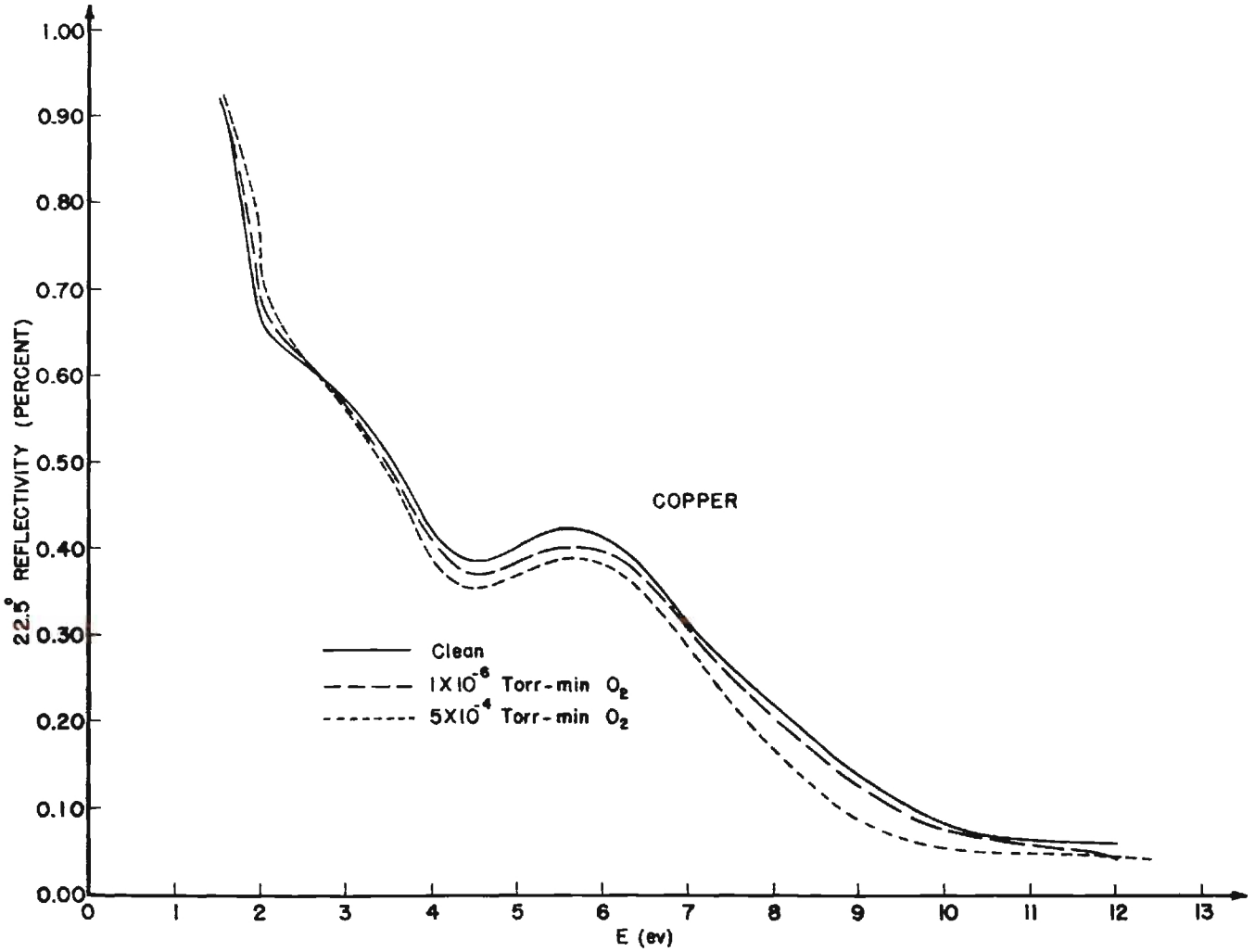

Figure 15. Reflectivity of Copper at 22.5° Incident Angle for Different Surface Conditions.

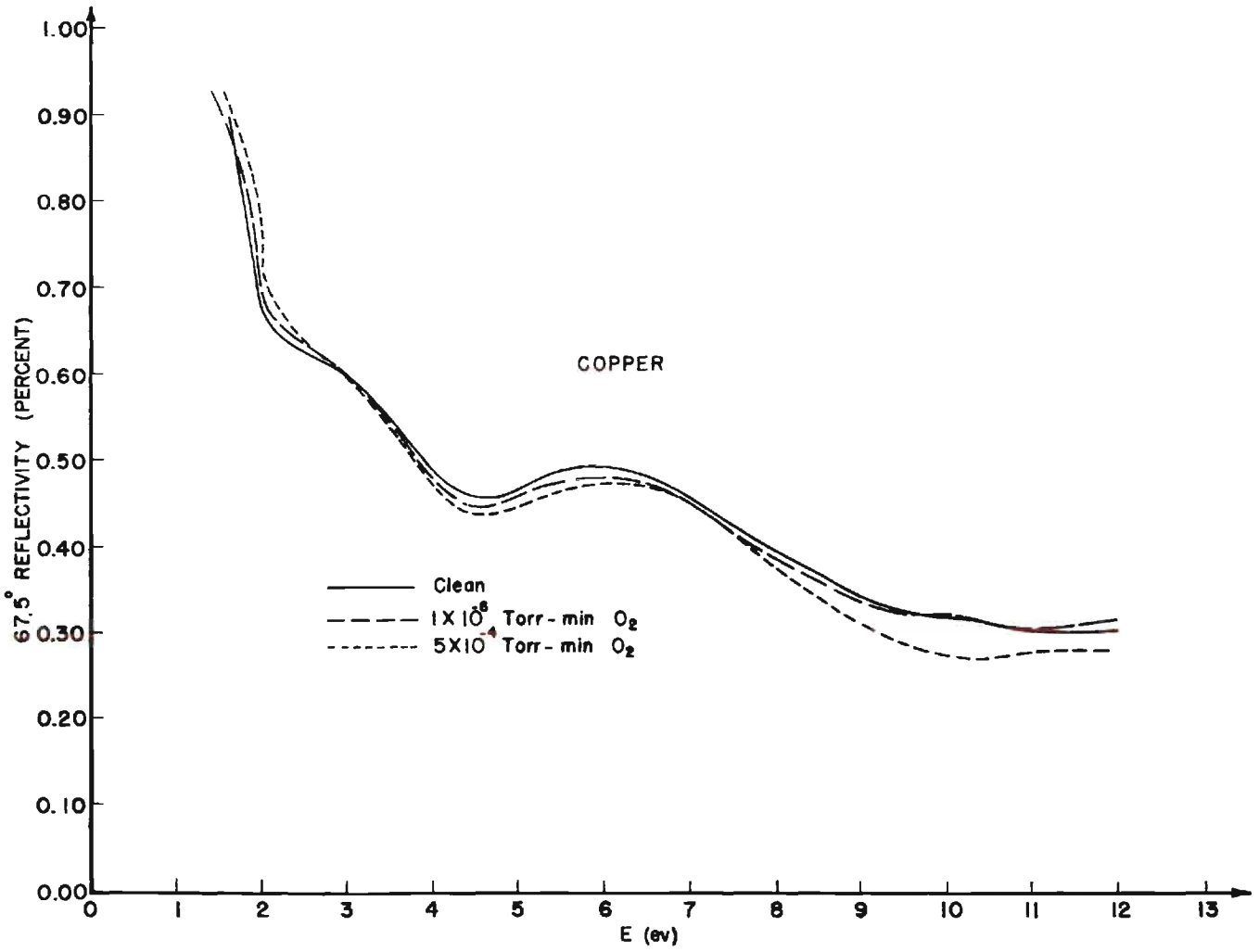

Figure 16. Reflectivity of Copper at 67.5° Incident Angle for Different Surface Conditions.

pond very roughly to one-quarter and three-quarter monolayer coverages. These data are shown in the dashed and dotted curves in Figures 15 and 16 and were taken to see if changes occurred in the surface plasmon loss function corresponding to those observed in the energy loss data.

The reflectivity data were analyzed by an iterative computer procedure to obtain a solution of the Fresnel reflectivity equations in terms of the optical constants n, the refractive index, and k, the reflection coefficient. These constants were then used to calculate ϵ_1 and ϵ_2, the real and imaginary parts of the dielectric constant, the energy loss function, $-\mathrm{Im}(1/\epsilon)$, and the surface plasmon loss function, $-\mathrm{Im}(1/1+\epsilon)$. The results of this analysis are shown in Figures 17, 18, 19, and 20 where the curves have been drawn to correspond to the same surface conditions as in Figures 15 and 16.

Many of the optical properties of copper can be discussed in detail with the aid of fairly accurate band structures such as those calculated by Burdick[81] and Segall.[82] The high reflectance region seen in Figure 15 extending up to about 2 ev arises from a lack of optical absorption; the abrupt decrease near 2 ev is caused by the onset of interband transitions. Interband absorption can be identified with structure in the imaginary part of the dielectric constant. The transition at 2 ev is seen as the first peak in $\epsilon_2(\omega)$ in Figure 18; the second peak in that figure gives evidence for a transition near 4.5 ev. In copper the Fermi surface is known to contact the (111) faces of the first Brillouin zone at the points conventionally labeled L, but do not touch the (100) faces at X.[83] Furthermore, there is a high density of states at both X and L so one might suppose that the peaks at 2.5 and 4.5 ev are

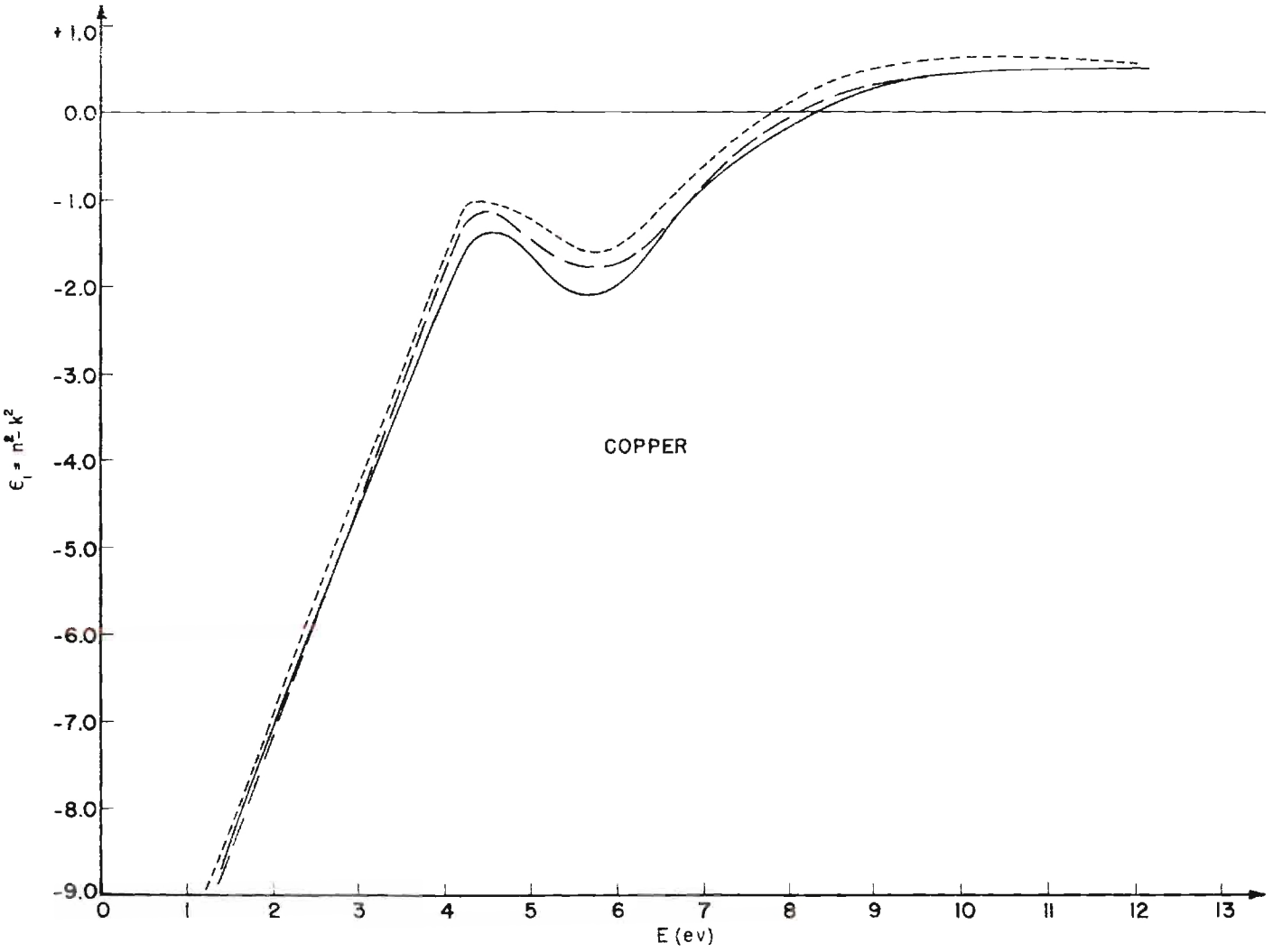

Figure 17. Real Part of Copper Dielectric Constant for Different Surface Conditions.

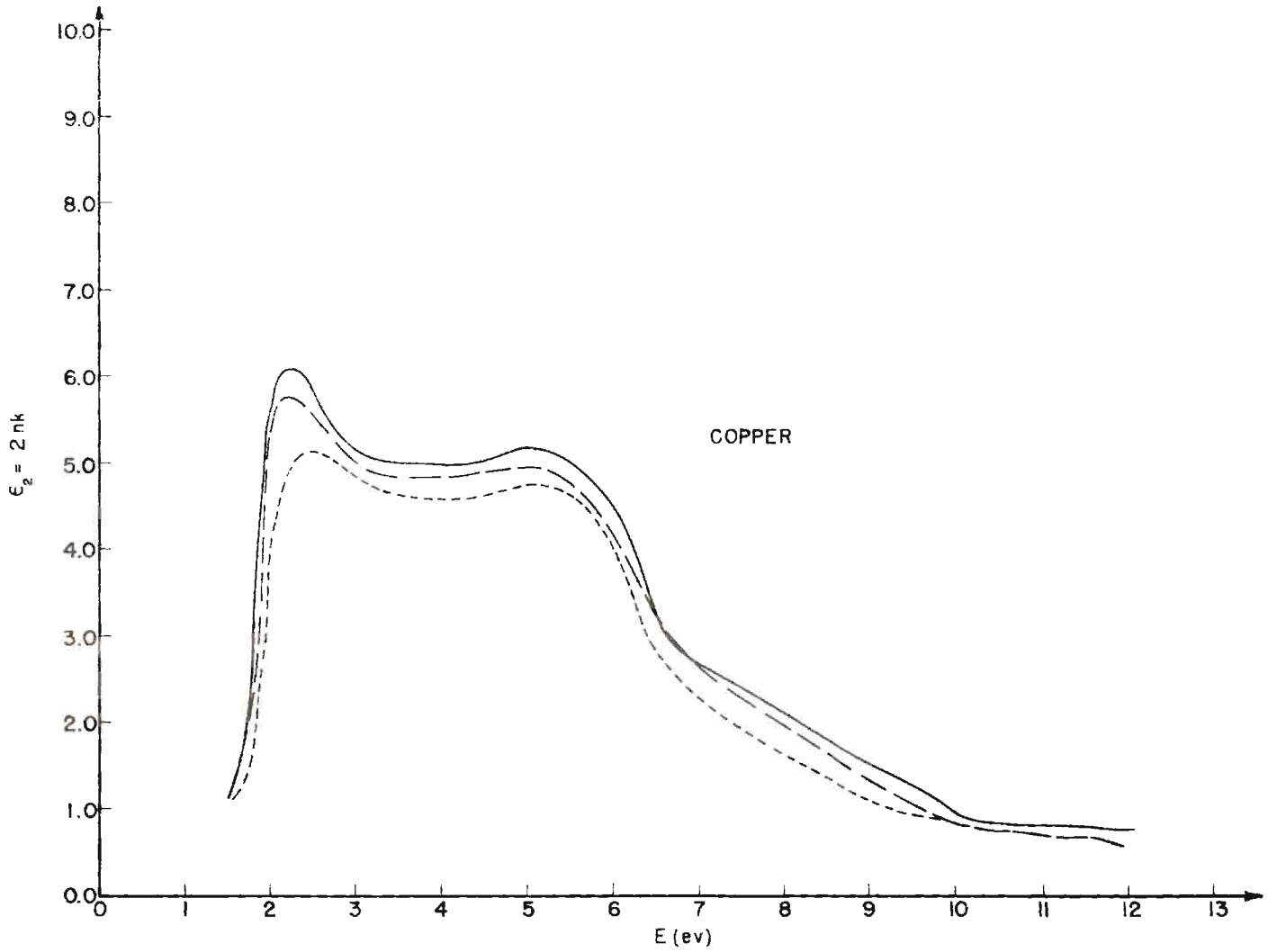

Figure 18. Imaginary Part of Copper Dielectric Constant for Different Surface Conditions.

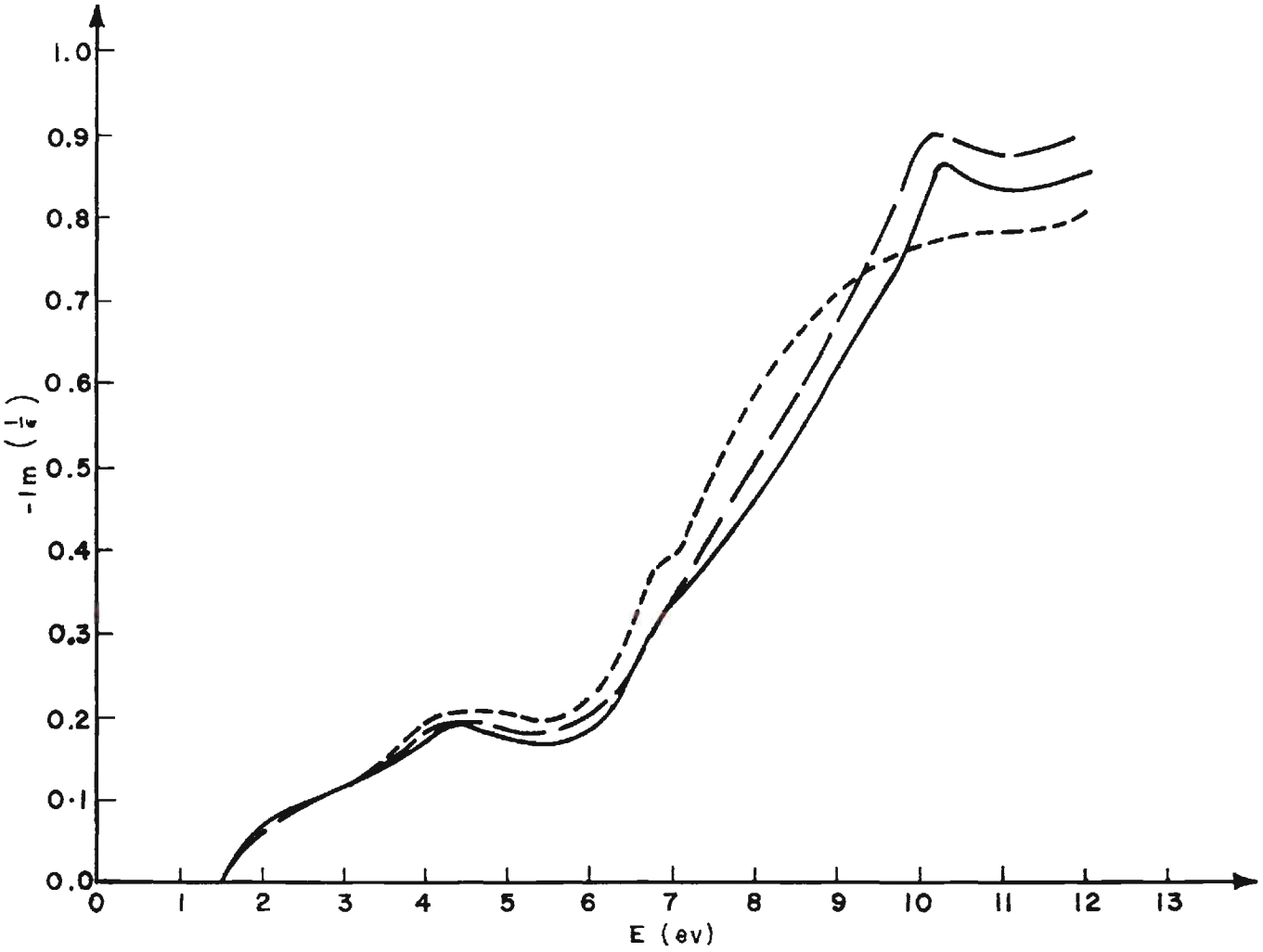

Figure 19. Optical Energy Loss Function of Copper with Different Surface Conditions.

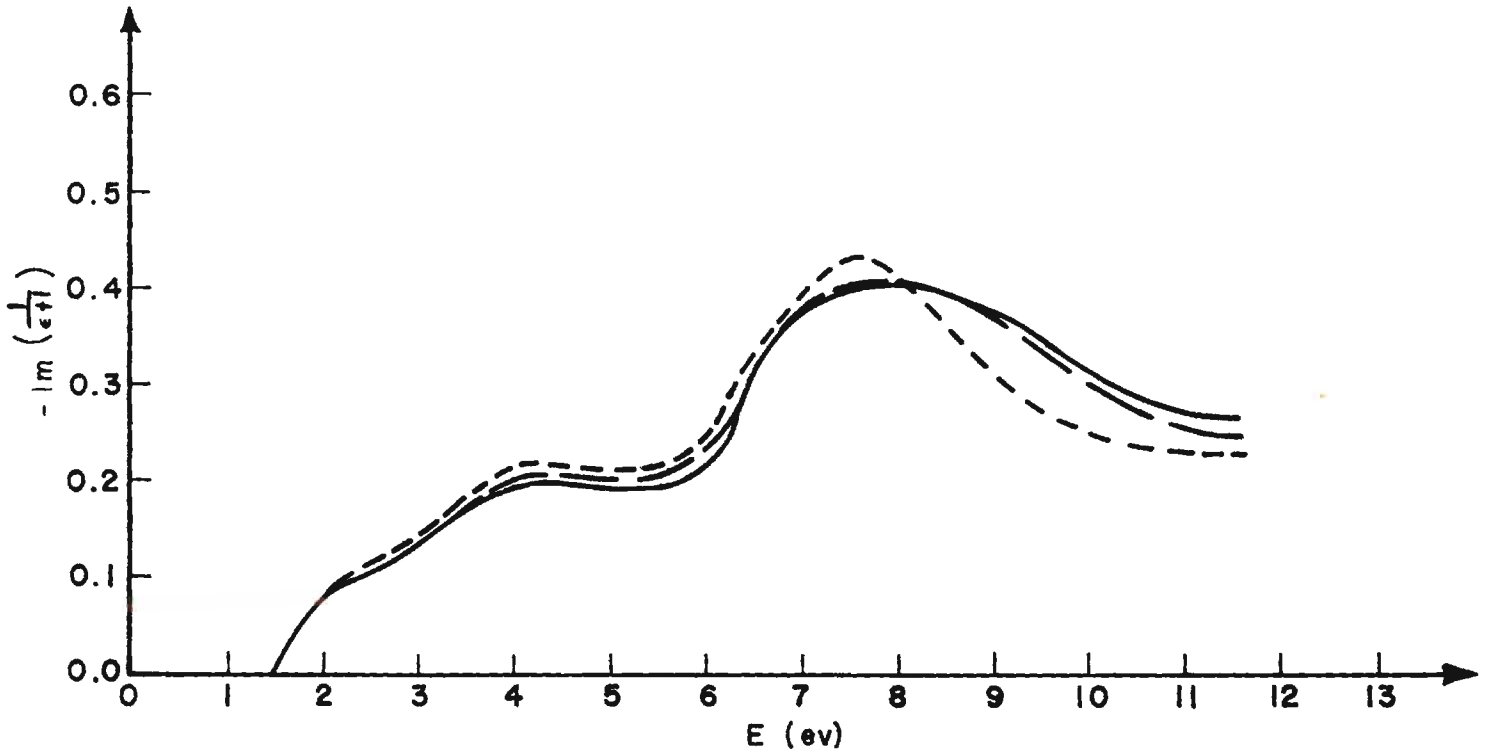

Figure 20. Surface Plasmon Loss Function of Copper with Different Surface Conditions.

associated with excitations of d-electrons into these regions; these transitions are indicated by arrows in Figure 21 which shows the general features of Segal's calculated energy band structure. It is also possible that valence electron excitations from occupied p-like states near L to s-like states contribute to the peak in ϵ_2 near 5 ev.

Collective excitations of the electron gas are also excited by phonons and give structure to the energy loss functions $-\mathrm{Im}(1/\epsilon)$ and $-\mathrm{Im}(1/1+\epsilon)$ for the bulk and surface plasmons. In the absence of damping the surface plasmon is located by $\epsilon_1 = -1$ which would be near 7 ev according to Figure 17. The corresponding peak in the surface plasmon loss function is exhibited near 8 ev in Figure 20 and serves to further support the identification made from the energy loss data. The energy range of the optical data was limited such that the bulk plasmon excitation near 20 ev was not observed in the energy loss function $-\mathrm{Im}(1/\epsilon)$; however, this loss is seen considerably broadened about 20 ev in the optical energy loss function determined by Ehrenreich and Philipp.[3]

The reflectivity data determined for different surface conditions are consistent with previously reported decreases in reflectivity with continued exposure of the sample to poor vacuum conditions.[59] The clean surface reflectivities averaged about 5 per cent higher at 22.5° and about 4 per cent higher at 67.5° incident angle. The surface plasmon peak seen in Figure 20 at 7.5 ev did not decrease in intensity as oxygen was adsorbed onto the crystal. That this peak actually increased in amplitude can be explained by examining the behavior of ϵ_1 and ϵ_2 for the different surface conditions shown in Figures 17 and 18. When oxygen was adsorbed onto the clean crystal, ϵ_1 assumed smaller negative values as it

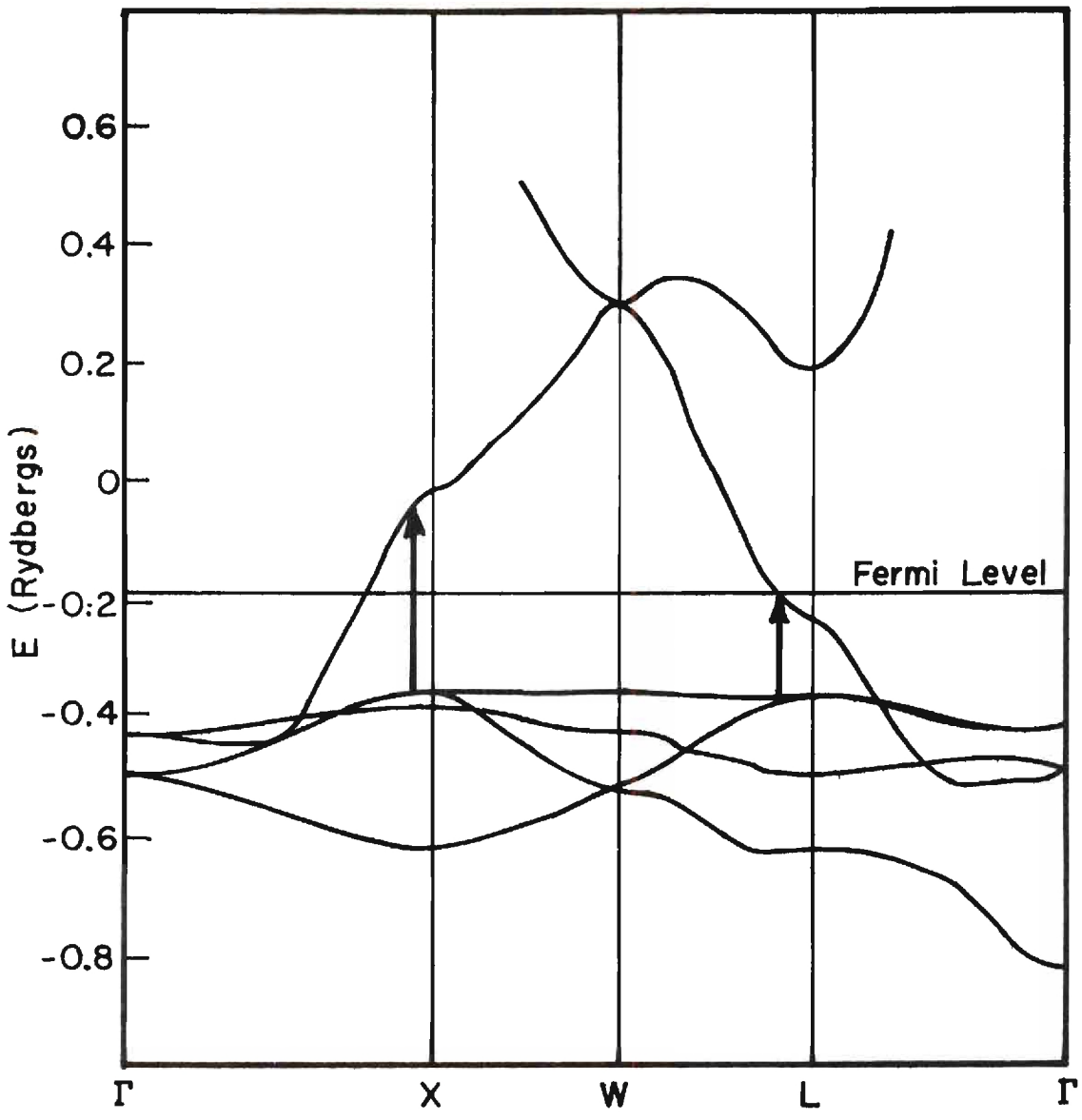

Figure 21. Energy Bands in Copper Showing Likely Interband Transitions.

approached the ϵ_1 representing the unclean surface. These dependences were a direct consequence of the higher reflectivities observed on the cleaned surface, and their effect was to decrease the surface plasmon excitation probability for the smaller ϵ_1 and ϵ_2 observed on the uncleaned surface. These effects on $-\mathrm{Im}(1/1+\epsilon)$ were so large that decreases in the probability of surface plasmon excitation were obscured. For this reason the optical identification of the surface plasmon was not as sensitive to surface conditions as the characteristic energy loss measurements.

Discussion

The transition metals copper and nickel were chosen as samples in this study since their valence 4s-electrons do not move independently of the 3d core electrons and the lattice potential. A strong electron-plasmon interaction was therefore anticipated to affect the collective oscillation frequencies so that the plasmon loss spectra obtained at high temperatures would reveal the effects of thermal disorder on electronic structure. There are two points concerning the unperturbed energy loss spectra which had to be established before the disordered spectra could be confidently analyzed. First, a strong plasmon interaction with tightly bound d-electrons had to be demonstrated -- this would insure that the loss spectra are sensitive to the detailed single-particle energy band structure. Second, the characteristic energy loss spectra had to be shown to be composed mainly of collective excitations in order that the disorder effects be experimentally observable. These matters are the subject of this discussion.

The first quantitative measurements of characteristic energy losses of copper were made in 1930 by Rudberg[4] in an analysis of 50-400 ev

electrons scattered from the sample surface. Since that time, the majority of characteristic energy loss measurements have employed an energy analysis of electrons transmitted through thin films, a method first introduced by Ruthemann.[5] As shown in Table 2, the characteristic energy losses measured for copper before 1958 agree on only two values -- 7 and 20 ev. The variations in reported data reflect the different sample preparations and vacuum conditions of the many experiments. As seen in Table 3, however, the energy loss values reported since 1958 are in much better agreement. The improvement in results reflects more uniform sample preparation techniques and advanced pumping capabilities which have allowed experimentalists to study samples with similar bulk and surface properties.

It has generally been difficult to determine the origin of certain energy losses because precise knowledge concerning the electronic structure is not available, and because the various mechanisms often predict energy losses and intensities of roughly the same value. Rudberg and Slater's original suggestion that the losses were due to interband transitions[6] has been employed by Wanatabe,[7] and by Leder, Mendlowitz and Marton[8] to explain their loss spectra. On the other hand, the collective description of metals has been very successfully employed to explain characteristic energy losses of metals with free-electron valence gases.[13] In the cases of copper and nickel, two conflicting concepts of the collective excitations have been presented in the literature and each has been adopted by different investigators. One group has assigned the 7.5 ev loss in copper to a bulk plasmon excitation of the free 4s-electron gas. Others have included the 3d-electrons in the oscillation and interpreted

Table 2. Energy Losses for Copper Found Before 1958.

Rudberg[4]	3.4	6.9	12.3		25.5
Reichertz and Farnesworth[84]	3.0	6.0	12.3	20	
Marton and Leder[85]		6.9	11.3	19.6	
Kleinn[86]	3.1	6.4		21	
Wanatabe[87]		7		19.5	
Gauthé[88]		7.3		18.7	23.7
Pradul and Saporte[89]		5		20	

Table 3. Energy Losses for Copper Found Since 1958.

Powell[74]		4.4	7.2		19.9	27.1
Robins and Swan[2]		4.5	7.6		19.1	27.3
Marklund[90]		4.3	7.6	10.0	19.0	27.2
Ehrenreich and Philipp[3]	2.5	5.0	7.5			
Beaglehole[91]	2.5	5.0				
Present Work		4.5	7.5		19.5	27.5

the 7.5 ev loss as arising from a surface plasmon excitation of the combined 3d4s-electron gas.

The initial suggestion that the plasmon excitation involved only the 4s-electrons was made by Ehrenreich and Philipp.[3] Their optical data were interpreted in terms of a free-electron model with one electron per atom which was supported by observations that single-particle excitations from the s- and d-bands were insignificant below 10 ev and that no prominant transitions occurred near 10 ev to affect the collective motion. In a comprehensive treatment of electron-electron interactions and elementary excitations in solids, Pines[56] also regarded the 7.5 ev loss peak in copper as arising from free 4s-electron plasmon excitation modified only slightly by d-electron transitions. The d-electron interband transitions were suggested to cause a depression of the bulk plasmon energy from 9.3 ev, the energy predicted in the free-electron formalism after one accounts for intraband transitions in the gas. Pines therefore recognized the effect of the d-electrons in shifting the plasmon energy, but did not consider the possibility of their direct participation in the collective motion. Raether[73] further advanced this interpretation in his analysis of Ehrenreich and Philipp's optical data and also in his description of characteristic energy loss data obtained by one of his associates.[72] Theoretically, then, both observers recognized the existence of electron-plasmon interactions in the transition metals; they failed, however, to consider the excitation of a surface plasmon in interpreting the energy loss data. Thus, one objection to interpreting the 7.5 ev loss as a bulk plasmon excitation is the absence of a peak remaining in the loss spectrum which could represent the sur-

face plasmon excitation since all the lower-lying losses are known to be single-particle excitations. It is of course possible that one of these single-particle excitations obscures a surface plasmon excitation near 4 ev, but then the loss at 7.5 ev can not be interpreted as a bulk plasmon excitation in view of the sensitivity of this loss peak to surface conditions. This particular point was not mentioned by Ehrenreich and Philipp, Pines or Raether; neither did these authors explain why the surface plasmon excitation might not appear in the spectrum.

Other investigators have identified the 7.5 ev loss peak as arising from a surface plasmon excitation which indirectly included all the 3d-electrons in the collective motion. Robins and Swan[2] measured the characteristic energy losses of the transition metals between titanium and copper by examining the energy distributions of 1200 ev electrons reflected from evaporated films. When the loss spectra were examined as a group and all the electrons outside the 3p shell considered to participate in collective excitations, a consistent qualitative analysis of the effect of interband transitions in raising and lowering the plasmon energies depending on whether the 3d-electrons were tightly bound was made. In another experiment particularly valuable for showing that the 7.5 and 19.5 ev losses arise from collective excitations, Powell[74] investigated Al-Cu alloy films for various concentrations of Al in Cu. As the Al concentration increased, the free electron density decreased continuously; one loss was observed to shift from that of Cu at 20 ev to that of Al at 15 ev, and another loss to shift from 7.5 ev to 10 ev. This direct dependence on electron density indicates a collective nature for these two losses in agreement with Robins and Swan's treatment of

the copper characteristic energy loss spectra.

When the 3d-electrons are considered to participate freely in the collective excitations, the free-electron surface and bulk plasmon energies predicted for copper are 25.5 and 35.8 ev. Data obtained in this experiment were interpreted in terms of a 3d- and 4s-electron collective oscillation in which high-energy excitations of tightly bound 3d-electrons depress the bulk plasmon energy from 35.8 to 19.5 ev. The surface plasmon was identified at 7.5 ev from its intensity dependence on the surface dielectric constant. The optical data gave support for this interpretation through the surface plasmon loss function which showed a broad maximum near 8 ev. Several factors contributed heavily to this interpretation, the most important being the positive identification by electron energy loss and optical measurements of the surface plasmon excitation at 7.5 ev, the energy sometimes assigned to a bulk oscillation of free 4s-electrons. The question then remained as to whether the lack of agreement with free-electron theory was due to a frequency shift in oscillation of only the 4s-electron gas or if the 3d-electrons also participated in the plasmon oscillations. In the former case, the discrepancy could have been due to a strong lattice potential which caused the 4s-electrons to differ significantly from plane waves; in the latter case, plasmon excitations of "core" 3d-electrons are expected to reduce the plasmon energies. Both Powell's energy loss data on Al-Cu alloys and Robins and Swan's consistent analysis of energy loss spectra of the entire transition series metals support the participation of 3d-electrons in the plasmon motion, and, on this basis, the above interpretation was made. In this model, the plasmon dispersion depends

strongly on the oscillator strengths and excitation frequencies of the interband transitions available to the 3d- and 4s-electrons; the large energy shifts of the plasmon excitations from free-gas predictions give evidence of the extremely strong coupling between single electrons and the plasmon fields in transition metals.

Obviously, all the 3d-electrons in copper do not directly participate in a free-electron oscillation; a physical model of the bulk oscillation as freely involving only two of the least tightly bound d-electrons is consistent with a free-electron plasmon energy of 19.5 ev, using Equation 7 to relate plasmon energy and free-electron density. This total density of three electrons per atom is in agreement with the effective number of electrons per atom which contributes to the optical properties up to 20 ev found by Ehrenreich and Philipp[3] from considerations of the optical sum rule normally used to describe semiconductor properties. In terms of the plasmon dispersion relation which involves the frequencies and oscillator strengths of the single-electron excitations, Equation 18, the only non-vanishing oscillator strengths would be associated with the two "free" d-electrons and the single 4s-electron. This treatment is not intended to replace the plasmon dispersion relation, Equation 18; it is meant only to illustrate the mutual support between optical and electron energy loss data, and to emphasize the plasmon sensitivity to the electronic band structure and thus to thermal disruptions in that structure. The energy loss spectra can therefore be expected to change with increased sample temperature to indicate line broadening of the energy levels in a heated crystal.

Nickel

Electron energy loss and optical reflectivity measurements were made on a (100) face of a nickel single crystal using the apparatus described in Chapter III. The data and their interpretation are similar to that of copper and, in view of the detailed discussion just presented are only briefly described in this section. Characteristic energy loss measurements taken at elevated sample temperatures showed that increased half-widths resulted from increased disorder in the crystal. In view of the strong electron-plasmon coupling in the transition metals, the increased half-widths were attributed to an energy level broadening in the electronic band structure induced by thermal atomic disorder.

Characteristic Electron Energy Losses

Energy loss spectra of electrons backscattered from a clean nickel (100) surface were obtained for primary electrons with energies between 30 and 350 ev. After the crystal was electropolished to attain a smooth, undamaged surface, it was placed inside the LEED chamber and cleaned using the previously described techniques. The characteristic energy losses of clean nickel obtained with 200 ev primary electrons are shown in the energy loss spectrum of Figure 22; the diffraction pattern for this surface is seen in Figure 23(a). The energy losses in Figure 22 occur at 10, 19, and 28 ev; an apparent shifting of the lowest loss from 8.5 ev was caused by the resolution dependence of the electron optics on the energy of the electrons being analyzed. This loss was observed at 8.5 ev when the energy loss spectrum was obtained with 50 ev primary electrons.

The energy loss data for nickel were concentrated on the charac-

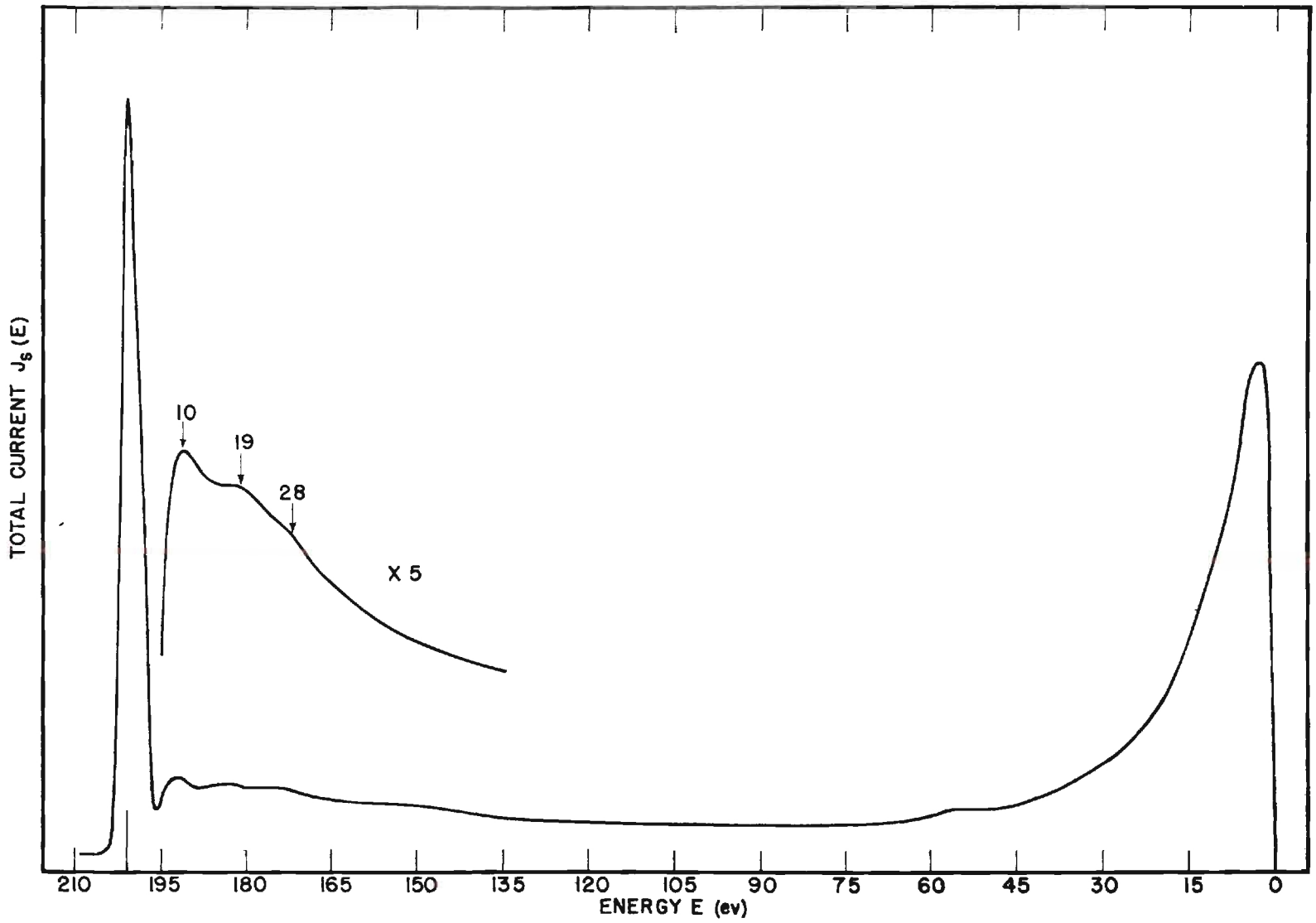

Figure 22. Electron Energy Distributions for 200-Volt Primary Electrons Incident on Clean Nickel (100) Surface.

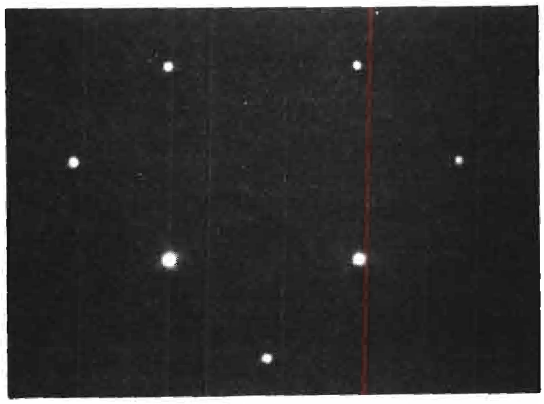

(a)

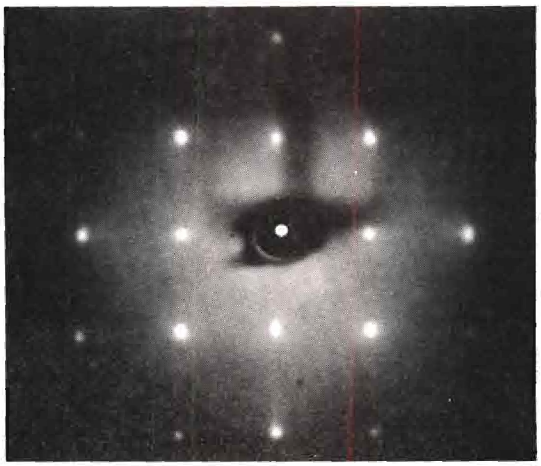

(b)

Figure 23. LEED Patterns for: (a) Clean Nickel (100) Surface, (b) Primitive Adsorption.

teristic losses to show that the collective electron motions in this transition metal are similar to those of its neighboring element copper. Except for exchange splitting in the 3d-band, the electron band structure of copper and nickel are quite similar, and, for this reason, it seemed appropriate to consider the plasmon excitations as a collective motion of both the 3d- and 4s-electrons. The bulk plasmon frequency would then be depressed below the free-electron value of 35 ev by an electron-plasmon coupling. In view of this coupling, the surface plasmon energy could not be predicted from the free-electron relations either; instead, it has to be determined by observing changes in the energy loss spectra as the surface was exposed to increasing amounts of oxygen. The reasoning here is that employed earlier in describing the copper characteristic energy losses.

Primitive (1 x 1) adsorption of oxygen on the nickel (100) face was observed after an exposure of 5×10^{-7} Torr-min as shown by the diffraction pattern of Figure 23(b). Further exposure did not give diffraction patterns but continued to affect the energy loss data. The effects of the changing dielectric constant at the vacuum interface with increased oxygen exposure are shown in the characteristic loss portion of the energy loss spectra in Figure 24. The diffraction patterns for the top two curves in Figure 24 are shown in Figure 23(a) and (b). The decreased intensity of the loss at 8.5 ev indicates that this is the surface plasmon energy in nickel. If the collective properties of the electron gas were not affected by interband transitions, the bulk plasmon energy would be 35 ev, and the surface plasmon would have an energy of 25 ev. It is evident that the free-electron model cannot be used when de-

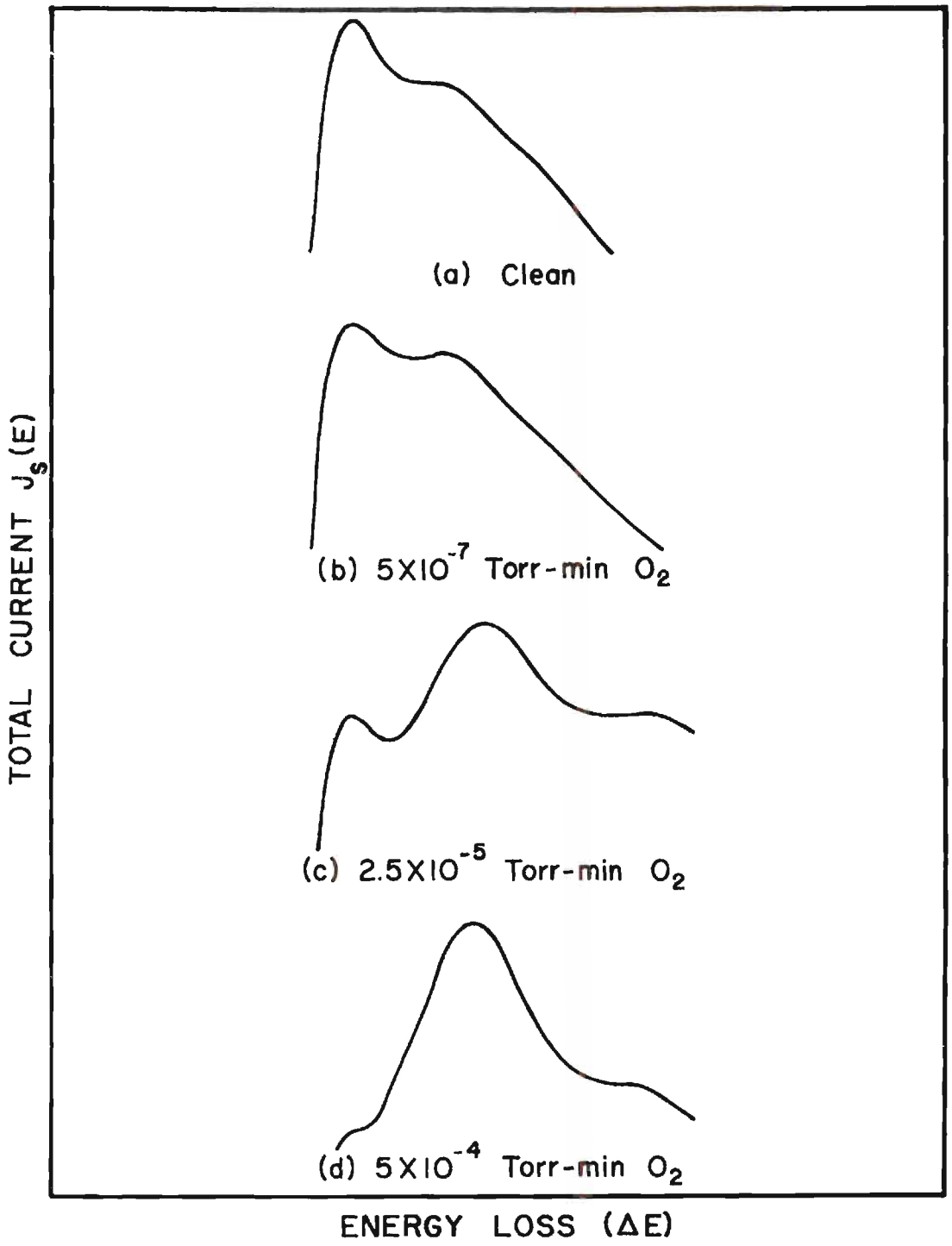

Figure 24. Variation of Surface Plasmon Intensity with Increased Oxygen Exposure on Clean Nickel (100) Surface.

scribing the collective properties of nickel since the loss at 19 ev is the bulk plasmon loss, in analogy with the identification made for copper, and the surface loss is 8.5 ev. Instead, the collective calculations must be based on an s- and d-electron model in which a strong coupling between the plasmons and high-energy interband transitions depresses ω below its free-electron value. This concept was further supported by an optical determination of the surface plasmon loss probability as a function of photon energy.

Optical Studies

The optical reflectivites of a (100) face of a nickel single crystal determined at two angles of incidence for photon energies between 1.65 and 11.8 ev are shown in Figures 25 and 26. The solid curves represents data taken on a clean surface which had been defined from LEED patterns and secondary electron energy distributions; Figures 22 and 23 (a). Similar data were obtained for the surface with roughly a full monolayer of adsorbed oxygen, exposure of 5×10^{-4} Torr-min, as indicated by the dashed curve, and for the surface where no cleaning other than annealing at 250° C had been attempted, as indicated by the dotted curve. The dielectric constants ϵ_1 and ϵ_2, the energy loss function $-\mathrm{Im}(1/\epsilon)$, and the surface loss function $-\mathrm{Im}(1/1+\epsilon)$ were derived from the reflectivity data for various surface conditions to support the identification of the surface plasmon loss energy in nickel and are shown in Figures 27, 28, 29, and 30.

The reflectivity spectra of nickel shown in Figure 25 for the various surface conditions differ qualitatively from copper only below about 2.5 ev. In nickel, the Fermi level intersects the d-bands, making possible

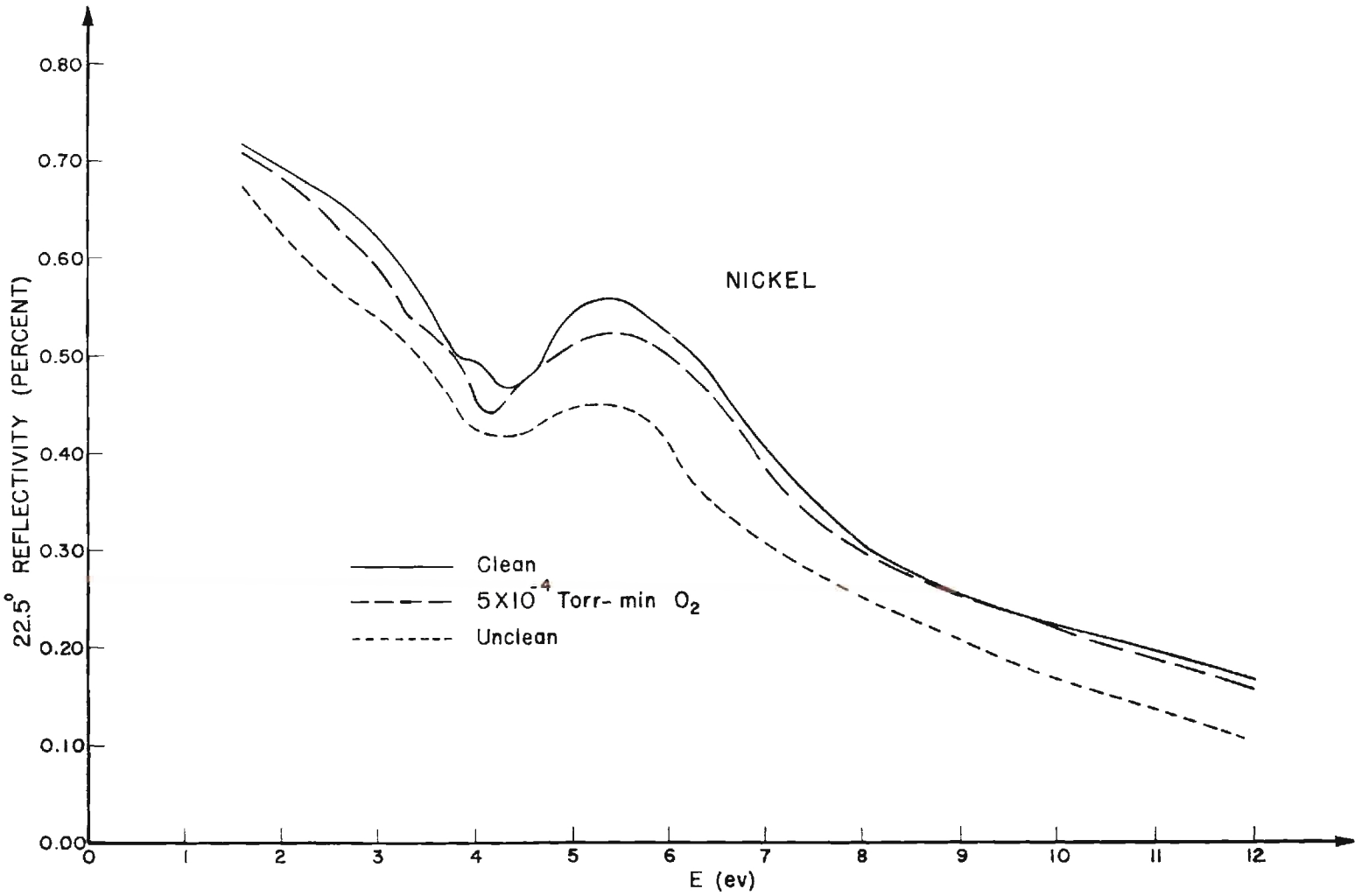

Figure 25. Reflectivity of Nickel at 22.5° Incident Angle for Different Surface Conditions.

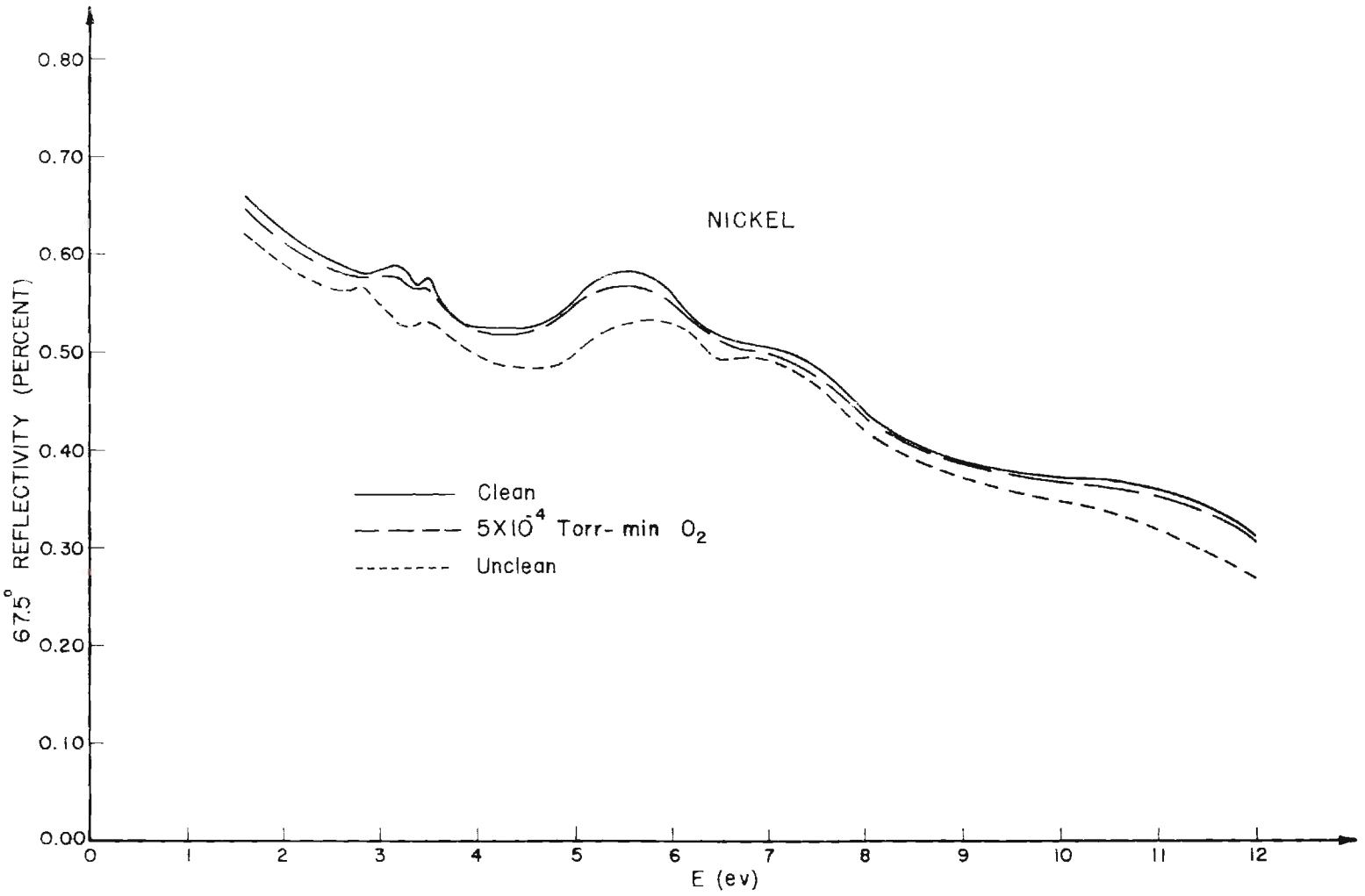

Figure 26. Reflectivity of Nickel at 67.5° Incident Angle for Different Surface Conditions.

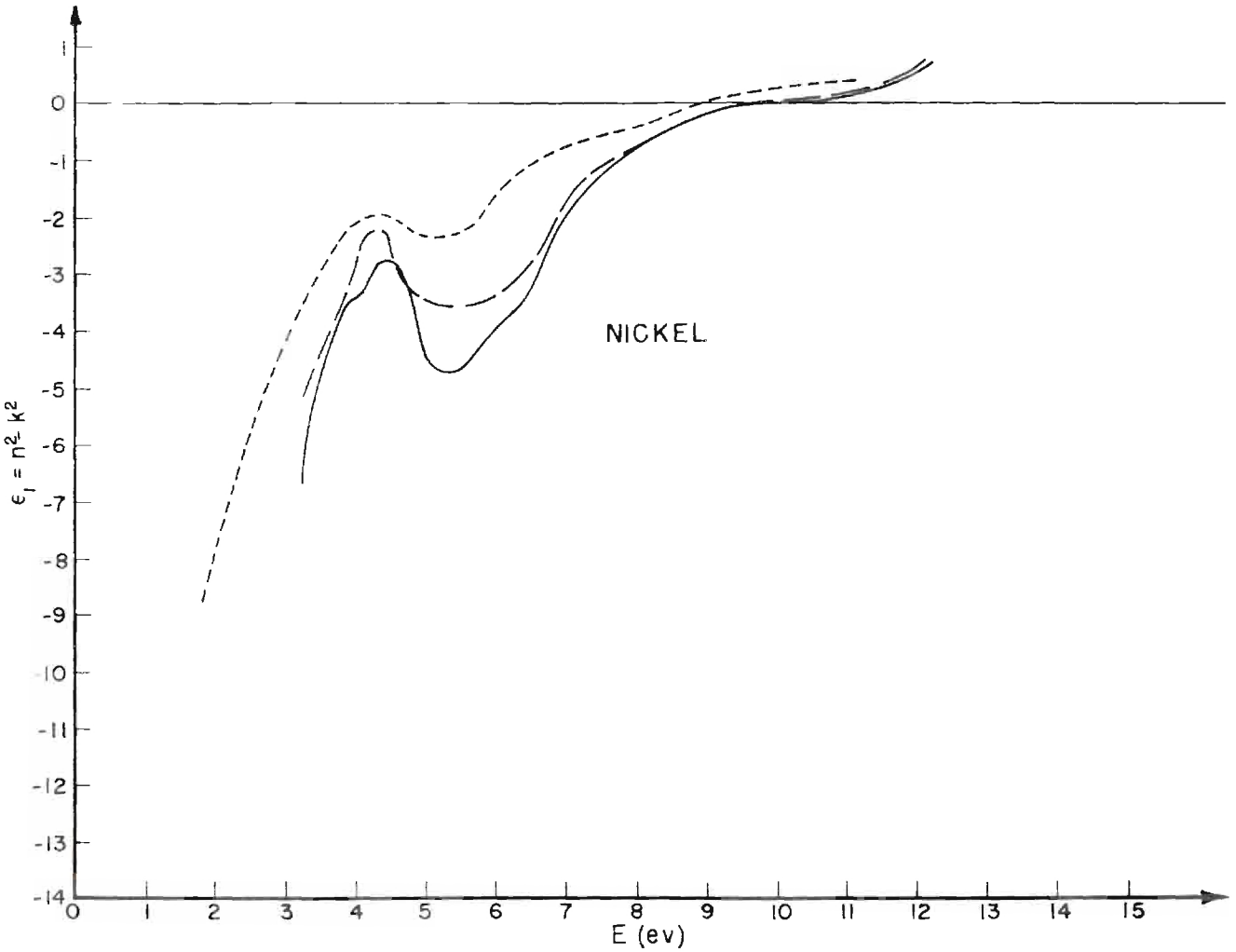

Figure 27. Real Part of Nickel Dielectric Constant for Different Surface Conditions.

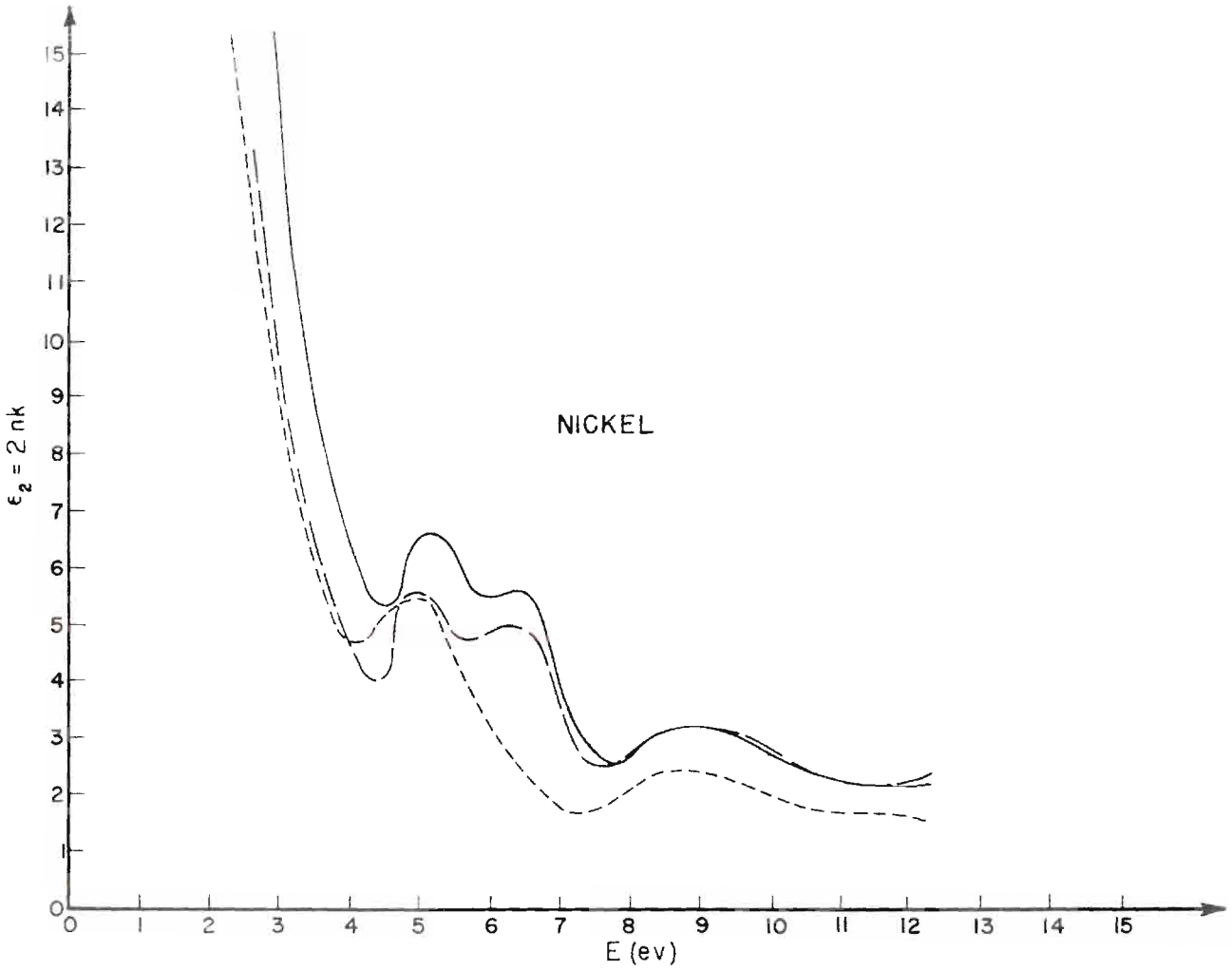

Figure 28. Imaginary Part of Nickel Dielectric Constant for Different Surface Conditions.

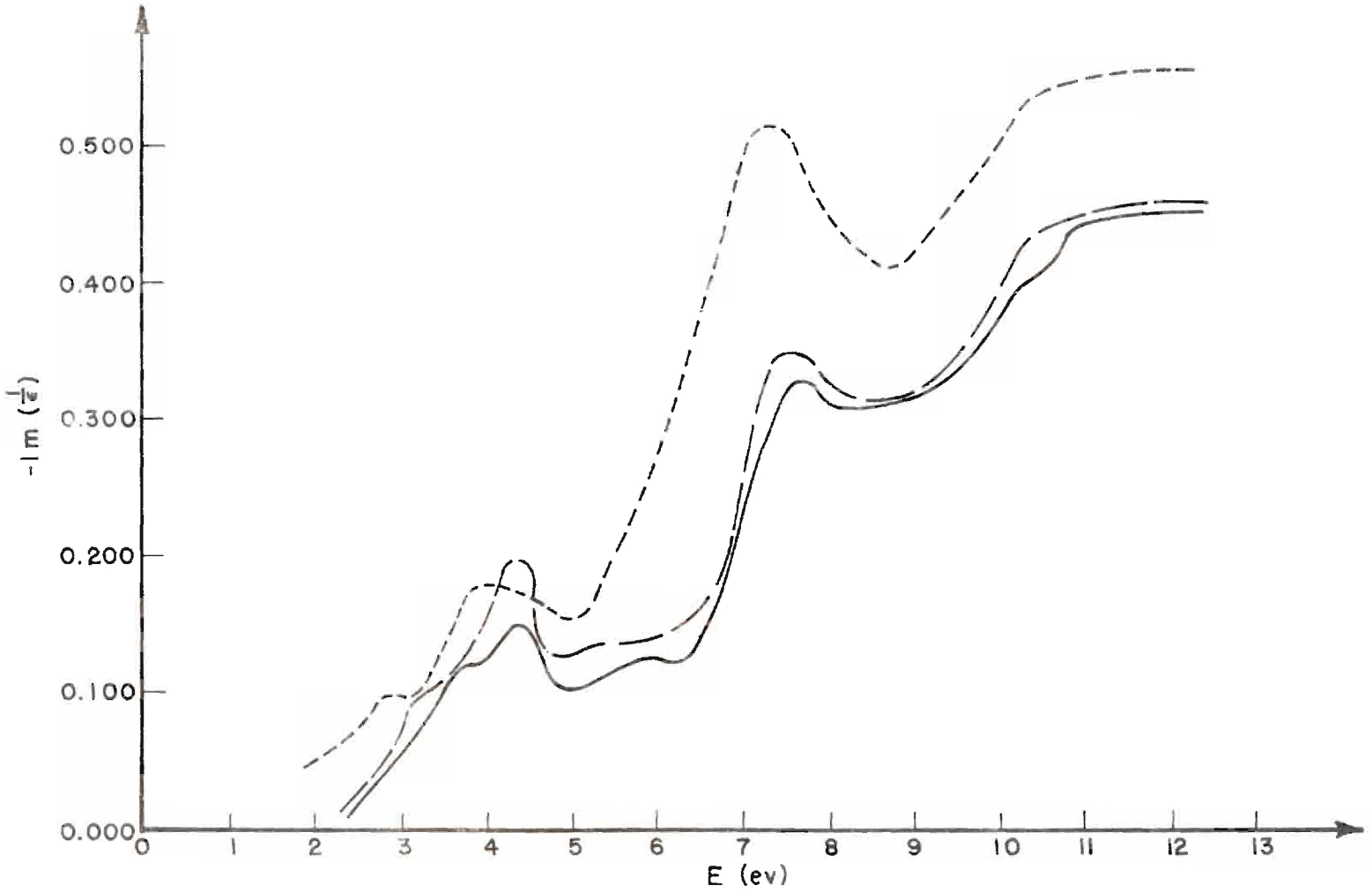

Figure 29. Optical Energy Loss Function for Nickel with Different Surface Conditions.

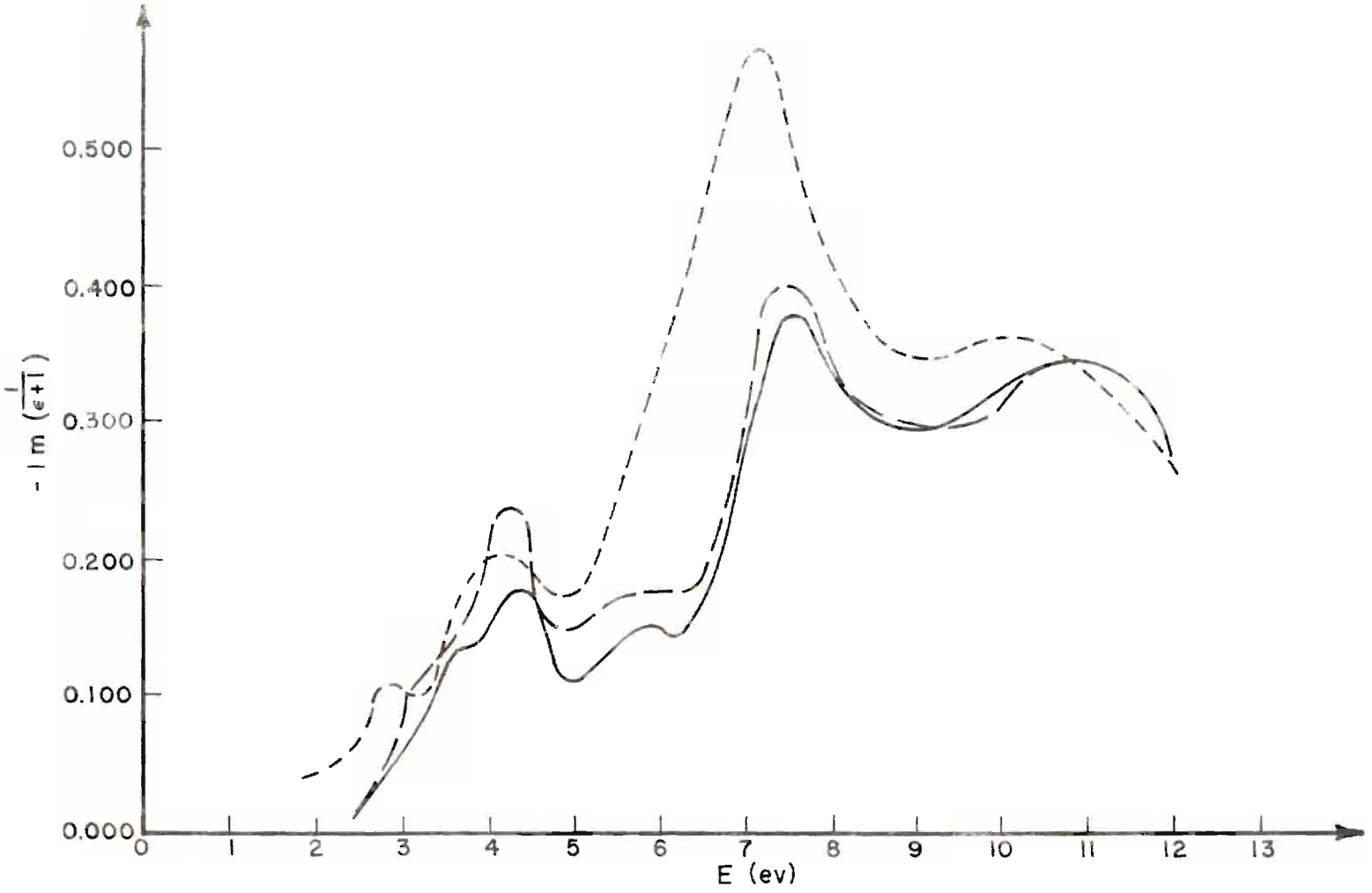

Figure 37. Surface Plasmon Loss Function for Nickel with Different Surface Conditions.

very low energy interband transitions from the 3d to 4s and 4p levels. In copper, the d-bands are found 2-4 ev below the Fermi level; above photon energies such that d-band excitations are possible, the optical properties of nickel and copper are thus very similar. The somewhat monotonic decrease in the Ni optical reflectivity is caused by these low-lying d-electron excitations. Optical data below 2 ev reported by Roberts[92] and by Beattie and Conn[93] reveal an interband transition with energy 1.4 ev and a loss at 0.3 ev probably due to free-carrier effects. As seen in Figure 28, interband transitions were resolved in ϵ_2 on the clean surface data at 5 and 6.3 ev. Hanus[94] has reported band structure calculations for nonferromagnetic nickel which interpolate very well between the results of corresponding calculations for copper and face-centered cubic iron. The 6.3 ev transition fits rather well between the high symmetry points L_2' and L_1 shown as a vertical arrow in Figure 31. No direct transition can be matched with the loss observed at 5 ev although this does not necessarily imply the existence of a non-direct transition at this energy. Above 5 ev, the reflectivity is determined by single-particle and many-electron excitations. The detailed optical properties have been discussed in the literature[95] and need not be considered further except as they pertain to identification of the collective excitations.

Optical identification of the surface plasmon involves the frequency dependence of both ϵ_1 and $-\mathrm{Im}(1/1+\epsilon)$. In Figure 27, ϵ_1 is seen equal to -1, the condition for surface plasmon oscillations at a clean surface, near 8 ev. The surface plasmon loss function plotted in Figure 30 displays a broad maximum near 7.5 ev. These results are in agreement

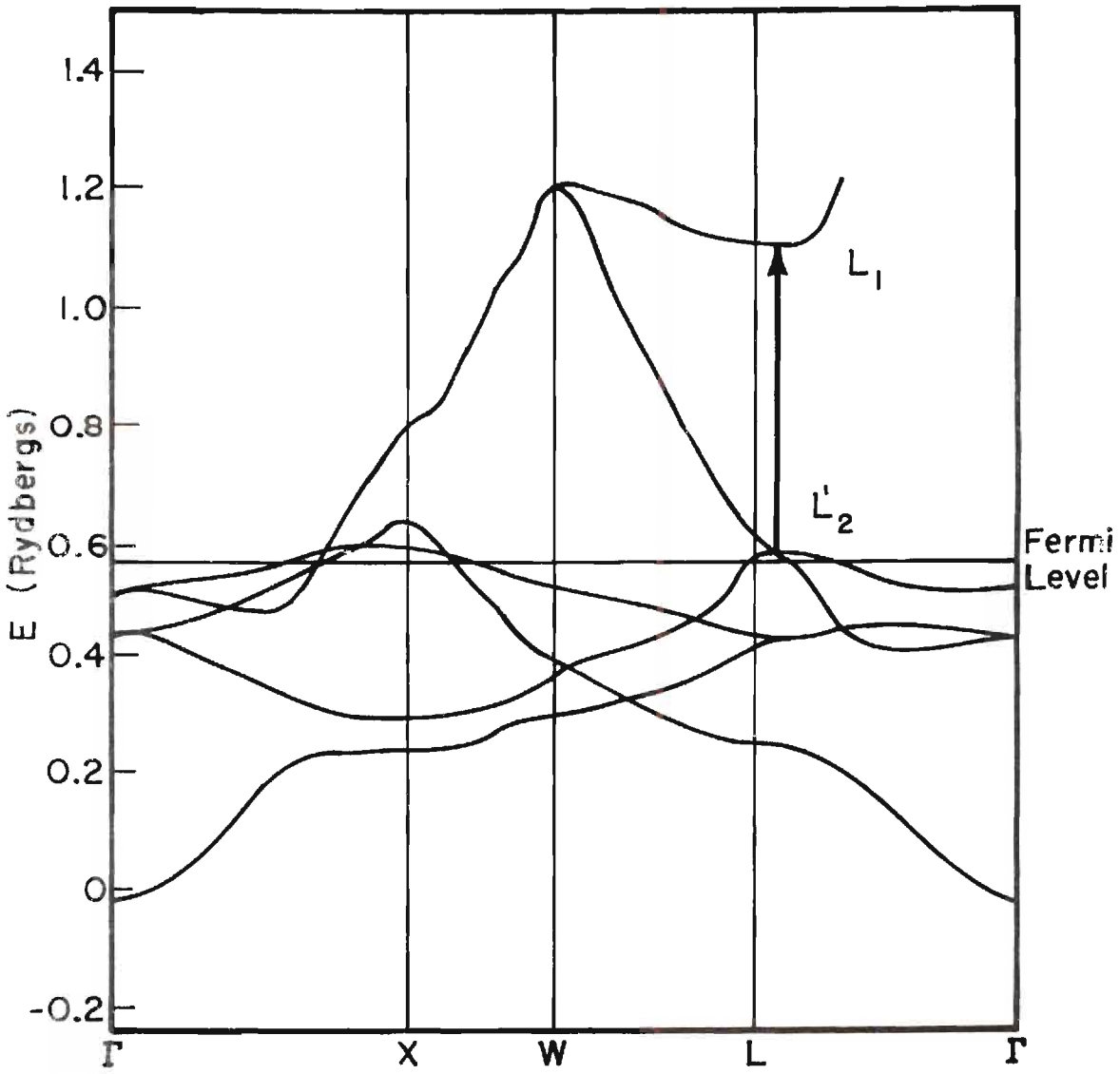

Figure 31. Energy Bands in Nickel Showing Likely Interband Transitions.

with the electron energy loss determination of the surface plasmon loss at 8.5 ev and provide the desired support for the participation of d- and s-electrons in the collective excitations. No optical data have been reported at photon energies up to 20 ev so the bulk plasmon excitation has not been optically determined.

Plasmon Excitations at Elevated Temperatures

Characteristic energy loss spectra obtained from the nickel crystal heated to temperatures near 1000°C are shown in Figure 32. These data were determined using 100 ev primary electrons -- this was the lowest primary energy which gave a well-resolved spectrum and which was not high enough to give deep penetration into the crystal. Below 700°C, the sample temperature was measured with a chromel-alumel thermocouple located inside the sample heater block; above 700°C, an optical pyrometer was used to measure the block temperature. For these reasons, the temperatures in Figure 32 may be subject to as much as ± 25°C errors although the sample and block were at equilibrium during the energy loss analyses.

Several observations are immediately made when these curves are compared at increasing sample temperatures. Significantly, no shifts in loss energies are observed; furthermore, the primary peak intensities and half-widths are not affected at the elevated temperatures. Both of these results are anticipated from previous remarks; phonon effects on electron scattering are too small to be resolved here, and, since the electron optics is not sensitive to the backscattered angle, decreases in Bragg diffraction were offset by increases in thermal diffuse scattering. Above 500°C there is a gradual "smearing" of the bulk and surface plasmon loss peaks which could result from increased half-widths. This

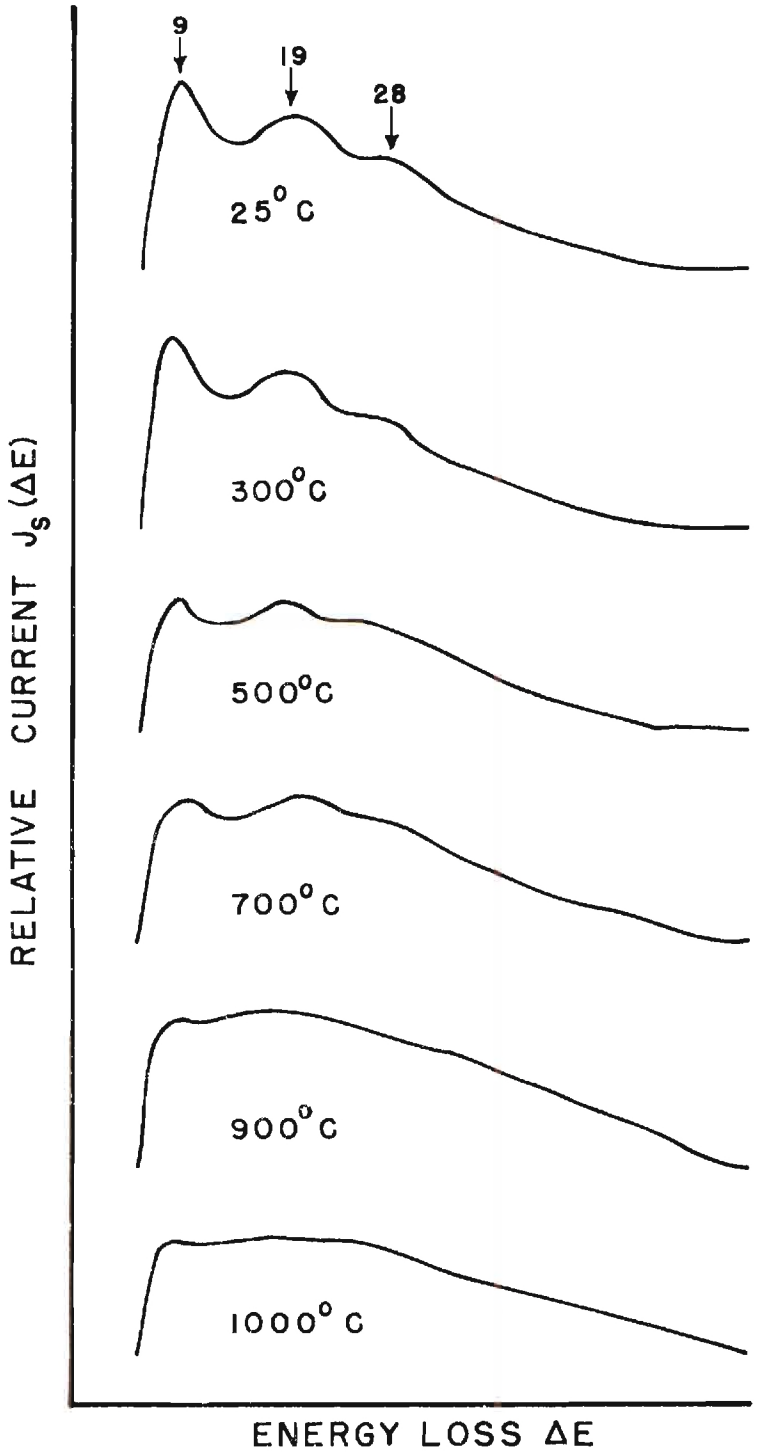

Figure 32. Variation of Characteristic Energy Loss Spectra of Nickel with Sample Temperature.

is expected from the previous discussions concerning electron-plasmon interactions and the effects of disorder on band structure in metals. Also, the surface plasmon loss peak is somewhat decreased in intensity relative to the bulk excitation. Intuitively, this seems reasonable since the sample surface temperature is higher than that of the bulk so the thermal vibrations could have more strongly affected the long-range Coulomb excitations in the surface layers.

In order to more explicitly determine what the effects of increased disorder were on the plasmon excitations, a computer technique which generated three Gaussian distributions and plotted their superposition was employed. The peak locations, heights, and half-widths could be adjusted to reproduce the observed plasmon spectrum. A basic assumption, which could be justified by comparisons between the generated and observed spectra, was made by assigning Gaussian shapes to the individual plasmon excitations. The individual plasmon loss distributions were approximated by a Gaussian distribution

$$Ae^{-(E-E_o)^2/2\Sigma^2}$$

where A is the peak height, E_o the loss energy, and Σ the half-width of the loss peak measured at that point where the peak height equals $Ae^{\frac{1}{2}}$. The increased plasmon half-widths determined from this analysis reflect the electron-plasmon coupling which is broadened through thermal perturbations on the electron energy band structure. These observations further support the participation of 3d-electrons in the collective motion since thermal effects on free-electron plasmon excitations are negligible

and would not produce the damping seen here. The results of this curve-fitting are seen in Table 4 for the three losses resolved in the room temperature data. It was found that essentially only the half-widths of the collective excitations needed to be increased to reproduce the energy loss data obtained at elevated sample temperatures.

Table 4. Parameters Describing Gaussian Distribution of Plasmon Spectrum versus Sample Temperature.

Temp	E_o	A	Σ	E_o	A	Σ	E_o	A	Σ
25° C	8.5	7.0	3.5	19	6.5	4.3	28	5.9	4.5
300° C	8.5	7.0	3.5	19	6.5	4.3	28	5.9	4.5
500° C	8.5	6.5	3.6	19	6.5	4.4	28	5.9	4.6
700° C	8.5	6.5	3.8	19	6.5	4.6	28	5.9	4.8
900° C	8.5	6.5	4.0	19	6.5	4.8	28	5.9	5.0
1000° C	8.5	6.5	4.1	19	6.5	4.9	28	5.9	5.1

Discussion

The characteristic energy losses previously reported for nickel are shown in Tables 5 and 6. In recent years, only Robins and Swan[2] have reported electron energy loss data, and only Ehrenreich, Philipp, and Olechna[95] have determined the optical constants up to 11 ev. These authors differed in their interpretation of the energy losses as Robins and Swan assigned values of 8.3 and 19.5 ev to the surface and bulk plasmon excitations of the 3d- and 4s-electron gas. Ehrenreich et al.

Table 5. Energy Losses for Nickel Found Before 1958.

Lang[86]					24
Möllenstadt[97]					22.6
Marton and Leder[85]	5.8	9.4	13.2	17.6	23.4
Kleinn[86]	5.4				21.8
Wanatabe[87]	6.5		12		23.7

Table 6. Energy Losses for Nickel Found Since 1958.

Robins and Swan[2]		4.3	8.3	19.5	27.1	68
Ehrenreich, Philipp, and Olechna[95]	1.4	5.0	10.0			
Present Work			8.5	19.0	28.0	

observed a loss near 10 ev which they interpreted as a bulk plasmon resonance arising from a free-electron concentration of nearly one electron per atom. They concluded that "the plasma frequency should be determined largely by the free-electrons and little affected by the presence of interband transitions." Thus, the same disagreement discussed in the case of copper persists in nickel.

The interpretation presented in this study was based on the results of characteristic energy loss and optical data obtained from surfaces with various degrees of cleanliness. The effect on the energy loss spectra of an increased dielectric constant at the surface was to decrease the excitation probability of the loss found at 8.5 ev in agreement with theoretical predictions concerning the surface plasmon excitation on surface conditions. This loss was therefore considered to arise from an excitation involving the electrons near the surface. The surface plasmon loss function obtained from the optical data peaked near 8 ev and supported interpretation of the loss peak as arising from a surface plasmon excitation. In view of nickel's similarity to copper, it was not surprising that these data firmly established the sensitivity of the collective oscillations to excitations of both the 3d- and 4s-electrons, and that they also comprise the major part of the characteristic energy loss spectra. In nickel, a strong plasmon interaction with individual electrons depresses the bulk plasmon energy of free 3d- and 4s-electrons from 36 to 19 ev and the surface plasmon energy from 25 to 8.5 ev. The sizes of these shifts reflect the intimate coupling existing between the long-range Coulomb excitations and the single-particle excitations characteristic of nickel's electronic band structure.

The characteristic energy loss spectra obtained at elevated sample temperatures also reflect the effects of extended thermal disorder on electronic band structure. Earlier in this study, line broadening of the energy levels in metals was seen to result from perturbations on the potential of an ideal lattice. The plasmon dispersion relation in Equation 25,

$$1 = \frac{\omega_p^2}{n} \sum_n \frac{f_{on}}{(\omega + i\Delta)^2 - (\omega_{on} + i\Gamma_{on})^2}$$

was derived to describe collective excitations in disordered systems with a strong electron-plasmon interaction. From this equation, increases in the single-particle energy level broadening at elevated temperatures were predicted to cause corresponding increases in the plasmon half-widths. In the empirical observations, the plasmon half-widths were found to increase with sample temperature in agreement with the theoretical analysis.

There are three contributions to the plasmon half-widths which had to be considered before analyzing these results. First there is the natural breadth of the collective loss peak which exists even in the complete absence of crystal imperfections. The width of a plasmon loss line is an indication of an extremely short lifetime due to a number of possible electronic interband transitions with similar excitation energies; in free gases, this loss breadth is very small as there are no strong damping or perturbing forces acting on the plasmon. An interaction of the plasmons in copper and nickel has already been seen to greatly affect

the plasmon energy -- a second consequence of this interaction is to shorten the plasmon lifetime so that its loss line has a finite half-width. This "natural" loss breadth could be determined more exactly from energy loss data obtained at very low sample temperatures with a high resolution instrument, but it is likely that the deviation from the value observed here at room temperature is small.

Another factor which affects the width of the plasmon loss peak is the experimental resolution of the retarding potential analyzing system. It has already been noted that this resolution is energy dependent so a constant half-width has not been added to each of the plasmon losses. This resolution had to be accounted for before the final contribution to the plasmon loss breadth, that due to a decreased lifetime of the interband transitions coupled to the plasmon motion, was determined. The data concerning the electron optics resolution showed that over the energy range in the plasmon spectrum, the resolution half-widths were 1.85, 1.75, and 1.60 ev for the surface, bulk, and combined loss peaks, respectively. These values contributed to the observed plasmon half-widths, and when they were subtracted from the computer analysis, the plasmon half-width variation with sample temperature seen in Figure 33 was obtained. In these curves, the small slope at room temperature indicates that the room-temperature plasmon half-widths are close to those obtained when all thermal effects are removed; these values are thus considered to arise only from electron-plasmon coupling and contrast with half-widths of roughly 0.5 ev observed on metals such as Al and Mg where the valence electrons oscillations are not coupled to disruptive single-particle excitations. The surface plasmon half-width measured

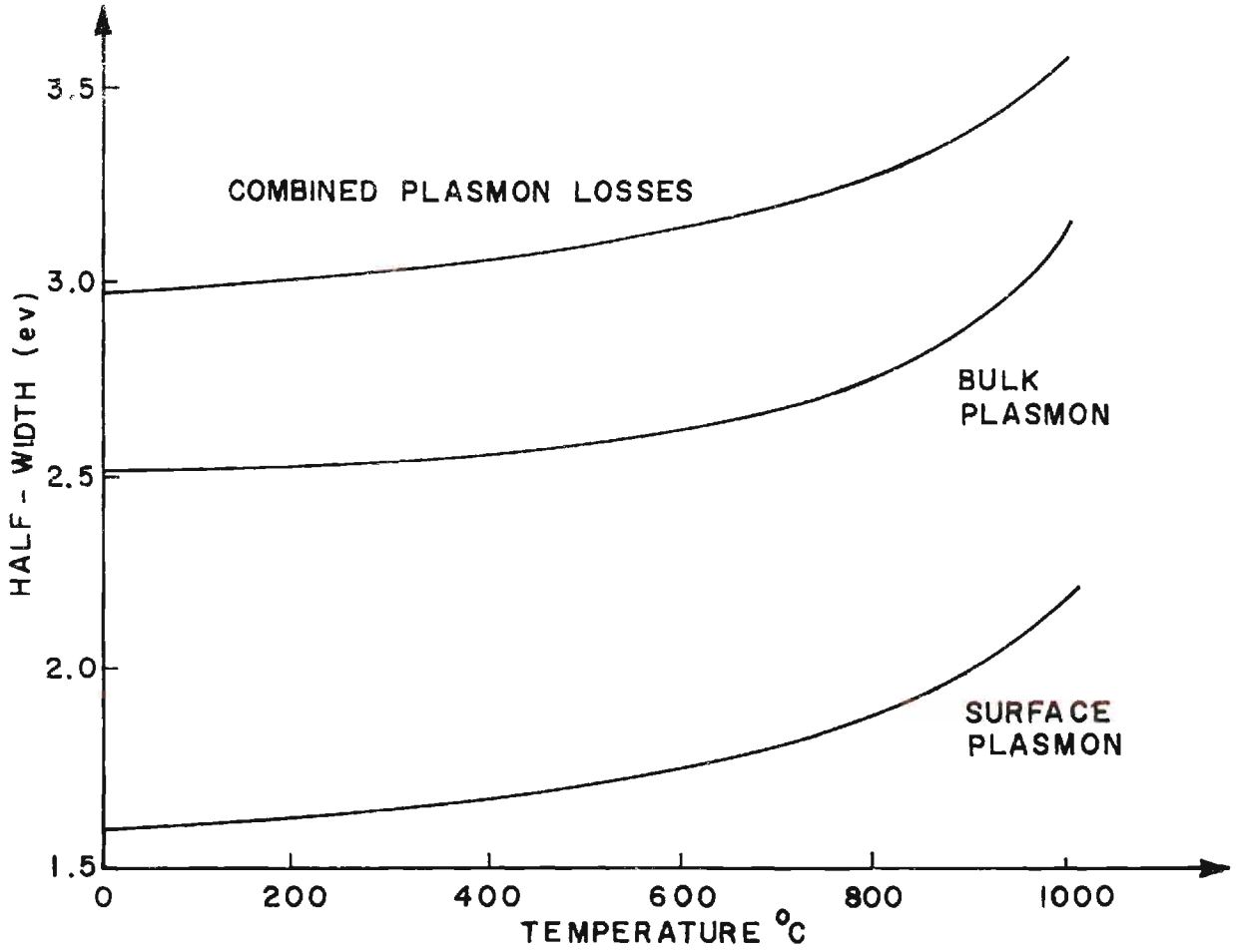

Figure 33. Variation of Nickel Plasmon Half-Widths with Sample Temperature.

for nickel at room temperature corresponds to an excited state lifetime of approximately 3×10^{-16} sec. This lifetime decreased about 50 per cent at a sample temperature 70 per cent of the bulk melting point as a result of decreases in single-particle excited state lifetimes. Similar observations were made for the loss peaks corresponding to bulk and combined plasmon excitations.

The increases in half-width above room temperature are attributed to broadening in the individual energy levels of the electronic band structure in agreement with the qualitative predictions of Equations 25 and 26 where thermal disorder was seen to decrease single-particle excitation lifetimes and consequently decrease the coupled plasmon lifetimes. Above 800°C, a rapid increase in half-widths occurs in Figure 33; since the penetration depth of 100 ev primary electrons is limited to a few layers and these layers are known to "melt" at temperatures well below the bulk melting point, this increase may be due to a radical change in the electronic structure accompanying a physical change which can not be treated as a perturbation on the ideal lattice structure. As mentioned earlier, MacRae[28] found that disorder increases much more rapidly in the surface layers than in the bulk layers at temperatures well below the melting point. Although detailed calculations regarding the temperature dependence of disorder are required before these observed effects can be further related to band structure perturbations, the qualitative effects of thermal disorder in broadening single-particle energy levels has been successfully demonstrated.

CHAPTER V

CONCLUSIONS AND RECOMMENDATIONS

The main results of this investigation can be summarized as follows. Copper and nickel characteristic energy losses were shown to be mainly composed of collective excitations. These collective modes however were strongly coupled to single electron modes so that the observed energy loss values were significantly different from the free-electron value. Because of the coupling of collective and individual electron modes it was also possible to study the effect of thermal disorder on the plasmon dispersion relation. This was done by first studying the theory of collective oscillations with emphasis on the coupling of plasmon and single electron excitations to demonstrate the potential sensitivity of the plasmon excitations to changes in the structure of the one-electron energy bands. Then perturbations on the crystalline potential were examined and shown to lead to line broadening in the band structure. This line broadening was then used to predict an increase in the plasmon loss half-widths due to the presence of single-particle excitation frequencies and oscillator strengths in the plasmon dispersion relation.

The applicability of the plasmon dispersion relation to the metals studied was demonstrated by identification of the bulk and surface plasmon energies from both electron energy loss and optical analyses of the surface plasmon excitation probability for various surface conditions. The energy loss data showed a decrease in the surface plasmon

loss probability as predicted from the dielectric theory[46] and in agreement with previous observations on Al and Mg.[15] The optical data did not reveal a similar decrease in the surface excitation probability because of the overall effect of surface conditions on the optical reflectivities. However, the behavior of the dielectric constants at the surface plasmon frequency did support the results of energy loss analyses.

The plasma oscillations were found to include both the 3d-electrons and the free 4s-electrons with a strong coupling between the plasmons and tightly bound electrons damping the collective excitations. The lifetimes of the surface and bulk plasmon excitations found at 8.5 and 20 ev in nickel were measured at room temperature as 4.1 and 2.6 x 10^{-16} sec respectively and a decrease of about 50 per cent at 70 per cent of the bulk melting point was observed. Similar data were obtained for copper. These results were explained in terms of broadening in single-particle energy levels caused by thermal disorder predicted by Jones[41] and Sergeeva[42] and suggested by the viscously damped response of harmonically bound electrons to the oscillating electric field of a plasmon excitation. This broadening arises from perturbations on the ideal crystal potential caused by the random thermal motion of the atomic ions with a resulting reduction in single-particle excitation lifetimes. The consequent reduction in plasmon lifetimes was in agreement with a theoretical description of plasmon dispersion in a thermally disordered crystal.

Throughout this dissertation, several problems were encountered suggesting further research which would beneficially extend the results described here. Characteristic energy loss data obtained from a series

of metals chosen to display different types of collective behavior could be used to study plasmon half-widths as a function of the degree of coupling with the valence electrons. These data should be obtained at low temperatures in a system which provides better energy resolution than that which was available for this work.

In this work, the effects of initial crystal disorder on inelastically scattered low-energy electrons have been described. Energy loss spectra have also been obtained from some materials in both the solid and liquid states,[99] but these materials demonstrated free-electron behavior in both phases so no information concerning changes in the electronic band structure was obtained. Investigations of the plasmon excitation spectrum of liquid transition metals would extend this study to a completely disordered system where a coupling has been shown to exist between the collective excitations and the electron band structure. Information pertinent to electronic structure in liquid metals could be obtained in this manner.

Structural modifications also affect the characteristic energy loss spectrum when there is a strong interaction between the plasmons and individual electrons. Metals exhibiting phase transformations at temperatures such that thermal effects are negligible would have different crystal potentials, energy band structures, and coupling effects on the plasmon excitation spectrum. In the theoretical description of the effects of crystal disorder, the possibility that a crystal might assume a superlattice structure was mentioned. When a superlattice exists, the matrix elements which determine the increase in energy level line widths could assume values which would give different amounts of

line broadening. If investigated with a high resolution electron spectrometer, the spectra for the different phases might reflect the different couplings between plasmons and the electron energy band structure.

Other inelastically scattered electrons are also affected by crystal disorder. Auger electrons emitted from samples at elevated temperatures would reflect broadening of energy levels in solids and could afford a test for some of the theoretical work concerning these electrons. Multiply-scattered secondary electrons would also show some temperature dependence although this behavior might not be easily analyzed.

Studies of electrons inelastically scattered from surfaces have only recently been employed to investigate solid state properties of metals and metal surfaces. This dissertation was concerned with one of many areas for research introduced by the combination of low-energy electron diffraction and low energy electron spectroscopy. Experimental and theoretical research in the areas suggested above could be used to advance the understanding of electron interactions in solids and to extend the usefulness of electron scattering as a tool for experimental studies of solid state surface properties.

APPENDICES

APPENDIX A

COLLECTIVE EXCITATIONS IN SOLIDS

The purpose of this appendix is to develop the plasmon dispersion relation for metals whose valence electrons are affected by the periodic potential in the solid. This calculation is expected to be most successful for solids with an energy separation between the core and valence electrons which is larger than the plasmon energy. Examples of the simple valence solids are the light alkali metals, alkaline earths and the solids just beyond them -- their electrons move in a periodic potential which can be accurately described by an average Hartree potential depending only on the positions of the valence electrons. In this case, the interaction of valence electrons and the plasma's electric field leads to electronic excitations within the valence band and the resulting effect on the plasmon frequency can be easily determined. For transition and noble metals, the plasmon energies are large enough so that the core electrons, isolated from plasma fields in the simple metals, are now available for interband transitions to the valence levels. This affects the potential in which the plasmons move and makes possible drastic shifts in the collective energies. For these more complicated metals, the collective theory presented here as developed by Nozieres and Pines[51] provides a qualitative description of the electron perturbations on plasmon motion and is able to successfully indicate the shift in plasmon frequency.

The potential energy due to the Coulomb interaction of the electrons,

$$\tfrac{1}{2} \sum_{i \neq j} \frac{e^2}{|\underline{r}_{ij}|}$$

has previously been written as

$$\tfrac{1}{2} \sum_{i \neq j} \sum_{k}{}' \frac{4\pi e^2}{k^2} e^{i\underline{k} \cdot (r_i - r_j)} . \qquad \text{(A-1)}$$

In terms of the Fourier components of the density fluctuations,

$$\rho_k \rho_k^* = \sum_{i,j} e^{i\underline{k} \cdot (r_i - r_j)}$$

this interaction becomes,

$$\sum_{k}{}' \frac{2\pi e^2}{k^2} (\rho_k \rho_k^* - N) \qquad \text{(A-2)}$$

where the term involving n, the number of valence electrons, is necessary to account for the sum over i = j in the expression for $\rho_k \rho_k^*$. The Hamiltonian for the valence electrons may then be written

$$H = \sum_i \left\{ \frac{P_i^2}{2m} + V(r_i) \right\} + \sum_k{}' \frac{2\pi e^2}{k^2} \left[\rho_k \rho_k^* - n \right] \qquad \text{(A-3)}$$

$$\equiv H_o + \sum_k{}' \tfrac{1}{2} M_k^2 \rho_k \rho - k$$

where we have substituted ρ_{-k} for ρ_k^*, and set $M_k^2 = \frac{4\pi e^2}{k^2}$. That this can be done follows from the definition of the ρ_k.

To introduce the plasmon field, we formally add to the Hamiltonian a term

$$H_1 = \sum_{k<k_c} \left[\tfrac{1}{2} \underline{P}_k^* \underline{P}_k - i \left(\frac{4\pi e^2}{m} \right)^{\frac{1}{2}} P_k \rho_k \right]$$

and impose on the system wavefunction Ψ the subsidiary conditions

$$\underline{P}_k \Psi = 0 \quad \text{for} \quad k < k_c$$

in order not to affect the energy spectrum of the system. We plan to transform the Hamiltonian so that the plasma oscillations appear as a finite set of simple harmonic oscillator Hamiltonians

$$H_{HO} = \tfrac{1}{2} \left[\underline{P}_k^* \underline{P}_k + \omega_B^2 \underline{Q}_k^* \underline{Q}_k \right] .$$

The difference between this plasmon frequency ω_B and the free-electron

$$H = \sum_i \left\{ \frac{P_i^2}{2m} + V(r_i) \right\} + \sum_k{}' \frac{2\pi e^2}{k^2} \left[\rho_k \rho_k^* - n \right] \qquad \text{(A-3)}$$

$$\equiv H_o + \sum_k{}' \frac{1}{2} M_k^2 \rho_k \rho_{-k}$$

where we have substituted ρ_{-k} for ρ_k^*, and set $M_k^2 = \frac{4\pi e^2}{k^2}$. That this can be done follows from the definition of the ρ_k.

To introduce the plasmon field, we formally add to the Hamiltonian a term

$$H_1 = \sum_{k<k_c}{}' \left[\frac{1}{2} \underline{P}_k^* \cdot \underline{P}_k - i \left(\frac{4\pi e^2}{m} \right)^{\frac{1}{2}} \underline{P}_k \rho_k \right]$$

and impose on the system wavefunction Ψ the subsidiary conditions

$$\underline{P}_k \Psi = 0 \quad \text{for } k < k_c$$

in order not to affect the energy spectrum of the system. We plan to transform the Hamiltonian so that the plasma oscillations appear as a finite set of simple harmonic oscillator Hamiltonians

$$H_{HO} = \frac{1}{2} \left[\underline{P}_k^* \cdot \underline{P}_k + \omega_b^2 Q_k^* Q_k \right] .$$

The difference between this plasmon frequency ω_b and the free-electron

frequency ω_p will reflect the effect of plasmon-electron coupling. Here, the Q_k and P_k are Fourier coefficients in the expansion of real field quantities

$$Q(\underline{r}) = \sum_k Q_k e^{i\underline{k} \cdot \underline{r}} \tag{A-4}$$

and obey the usual commutation relations

$$\left[\underline{P}_k, Q_\ell\right] = -i\hbar\, \delta_{k,\ell} .$$

They are also chosen to be Hermitian so that

$$P_k = P_k^* = P_{-k} .$$

We now make a canonical transformation on the Hamiltonian -- this leaves the energy spectrum eigenvalues unaltered, but the new form of the operators has classical analogs. We make the operator transformations

$$A \leftarrow S^{-1} A S$$

where

$$S = \exp\left[\frac{1}{\hbar} \sum_{k<k_c} M_k Q_k \rho_k^*\right] . \tag{A-5}$$

Using this transformation, we find the new variables

$$\underline{r}_i \rightarrow S^{-1}\underline{r}_i S = SS^{-1}\underline{r}_i + S^{-1}\underline{r}_i S - S^{-1}S\underline{r}_i$$

$$= \underline{r}_i + S^{-1}\left[\underline{r}_i, S\right]$$

$$= \underline{r}_i$$

$$Q_k \rightarrow Q_k + S^{-1}\left[Q_k, S\right] = Q_k$$

$$\underline{P}_i \rightarrow \underline{P}_i + S^{-1}\left[\underline{P}_i, S\right] = \underline{P}_i + S^{-1}\left[-i\hbar\frac{\partial s}{\partial \underline{r}_i}\right]$$

$$= \underline{P}_i + S^{-1}\left\{-i\hbar S\frac{1}{\hbar}\sum_{k<k_c} M_k Q_k i\underline{k}\right\}$$

$$= P_i + \sum_{k<k_c} \underline{k}\, M_k Q_k e^{i\underline{k}\cdot\underline{r}_i}$$

$$\underline{P}_k \rightarrow \underline{P}_k + \left[P_k, S\right] = \underline{P}_k + S^{-1}\left[-i\hbar \frac{\partial S}{\partial Q_k}\right]$$

$$= \underline{P}_k + S^{-1}\left\{-i\hbar\, S\, \frac{1}{\hbar} M_k \rho_k^*\right\}$$

$$= \underline{P}_k - iM_k\rho_k^*$$

Using these prescriptions, we obtain the transformed Hamiltonian from

$$H = \sum_i \left[\frac{P_i^2}{2m} + V(\underline{r}_i)\right] + \tfrac{1}{2}\sum M_k^2 \rho_k \rho_{-k} - \sum_k nM_k^2 \qquad \text{(A-6)}$$

$$+ \sum_{k<k_c}\left[\tfrac{1}{2}\underline{P}_k^* \underline{P}_k - iM_k \underline{P}_k \rho_k\right] .$$

Term by term, we get (the superscripts on the summations are for identification)

$$\frac{P_i^2}{2m} \rightarrow \frac{P_i^2}{2m} + \frac{1}{2m}\sum_{k,\ell,<k_c}^{a} \underline{k}\cdot\underline{\ell}\, M_k M_\ell\, Q_k Q_\ell\, e^{i(\underline{k}+\underline{\ell})\cdot\underline{r}_i}$$

$$+ \frac{1}{2m}\sum_{k<k_c} \underline{k}\cdot\underline{P}_i\, M_k\, Q_k\, e^{i\underline{k}\cdot\underline{r}_i} + \frac{1}{2m}\sum_{k<k_c} M_k Q_k\, (-\underline{k}\cdot\hbar\underline{k})\, e^{i\underline{k}\cdot\underline{r}_i}$$

$$\underline{P}_k \rightarrow \underline{P}_k + \left[P_k, S \right] = \underline{P}_k + S^{-1} \left[- i\hbar \frac{\partial S}{\partial Q_k} \right]$$

$$= \underline{P}_k + S^{-1} \left\{ - i\hbar S \frac{1}{\hbar} M_k \rho_k^* \right\}$$

$$= \underline{P}_k - iM_k \rho_k^*$$

Using these prescriptions, we obtain the transformed Hamiltonian from

$$H = \sum_i \left[\frac{P_i^2}{2m} + V(\underline{r}_i) \right] + \frac{1}{2} \sum M_k^2 \rho_k \rho_{-k} - \sum_k n M_k^2 \qquad \text{(A-6)}$$

$$+ \sum_{k<k_c} \left[\frac{1}{2} \underline{P}_k^* \underline{P}_k - iM_k \underline{P}_k \rho_k \right] .$$

Term by term, we get (the superscripts on the summations are for identification)

$$\frac{P_i^2}{2m} \rightarrow \frac{P_i^2}{2m} + \frac{1}{2m} \sum_{k,\ell,<k_c}^{a} \underline{k} \cdot \underline{\ell} \, M_k M_\ell \, Q_k Q_\ell \, e^{i(\underline{k} + \underline{\ell}) \cdot \underline{r}_i}$$

$$+ \frac{1}{2m} \sum_{k<k_c} \underline{k} \cdot \underline{P}_i \, M_k \, Q_k \, e^{i\underline{k} \cdot \underline{r}_i} + \frac{1}{2m} \sum_{k<k_c} M_k Q_k \, (- \underline{k} \cdot \hbar \underline{k}) e^{i\underline{k} \cdot \underline{r}_i}$$

$$\frac{1}{2}\sum_{k} M_k^2 \rho_k \rho_{-k} \rightarrow \frac{1}{2}\sum_{k}^{b} M_k^2 \rho_k \rho_{-k}$$

$$- \frac{1}{2}\sum_{k} nM_k^2 \rightarrow - \frac{1}{2}\sum_{k} nM_k^2$$

$$\frac{1}{2}\sum_{k<k_c} \underline{P}_k^* \underline{P}_k \rightarrow \frac{1}{2}\sum_{k<k_c} \underline{P}_k^* \underline{P}_k + \frac{1}{2}\sum_{k<k_c}^{c} M_k^2 \rho_k^* \rho_k$$

$$- \frac{1}{2}\sum_{k<k_c}^{d} iM_k \underline{P}_k^* \rho_k^* + \frac{1}{2}\sum_{k<k_c}^{e} iM_k \rho_k \underline{P}_k$$

and,

$$- i\sum_{k<k_c} M_k \underline{P}_k \rho_k \rightarrow - i\sum_{k<k_c}^{f} M_k \underline{P}_k \rho_k - \sum_{k<k_c}^{g} M_k^2 \rho_k^* \rho_k \quad .$$

In combining these terms, it is convenient to break the sum (a) into two sums, one with $\underline{l} = -\underline{k}$

$$\frac{N}{2m}\sum_{k<k_c} - \underline{k} \cdot \underline{k} \left(\frac{4\pi e^2}{k^2}\right) Q_k Q_{-k} \tag{A-7}$$

and the other with $\underline{l} \neq -\underline{k}$

$$\frac{1}{2m} \sum_{k,\ell \neq -k} \underline{k} \cdot \underline{\ell}\, Q_k Q_\ell\, M_k M_\ell\, e^{i(\underline{k} + \underline{\ell}) \cdot \underline{r}_i}$$

If we note that (g) + (c) equals that part of - (b) with $k < k_c$, and that (e) + (d) = - (f), then we can collect the remaining terms as

$$H = \sum_i \left[\frac{P_i^2}{2m} + V(r_i)\right] \qquad H_O$$

$$+ \frac{1}{2} \sum_{k<k_c} \left[\underline{P}_k^* \underline{P}_k + \frac{4\pi N e^2}{m} Q_k^* Q_k\right] \qquad H_F$$

$$+ \frac{1}{2m} \sum_i \sum_{\substack{k,\ell \neq -k, \\ k,\ell<k_c}} \underline{k} \cdot \underline{\ell}\, Q_k Q_\ell\, M_k M_\ell\, e^{i(\underline{k} + \underline{\ell}) \cdot \underline{r}_i} \qquad H_{NL}$$

$$+ \frac{1}{2m} \sum_i \sum_{k<k_c} \underline{k} \cdot (\underline{P}_i - \hbar \underline{k})\, M_k Q_k\, e^{i\underline{k} \cdot \underline{r}_i} \qquad H_{INT}$$

$$+ \frac{1}{2} \sum_{i,j \neq i} \sum_{k<k_c} M_k^2\, e^{i\underline{k} \cdot (\underline{r}_i - \underline{r}_j)} \qquad H_{SR}$$

$$- \frac{1}{2} N \sum_k M_k^2$$

The above designations are for:

H_F describing the plasmon field,

H_{INT} describing a linear interaction between electrons and plasmons,

H_{SR} describing the short-range part of the Coulomb interaction,

H_{NL} describing a non-linear interaction between electrons and plasmons.

The subsidiary conditions are also transformed from $\underline{P}_k \Psi$ to

$$(S^{-1} \underline{P}_k S)\ (S^{-1} \Psi) \ = \ 0$$

or

$$\left[\underline{P}_k - iM_k \rho_k^*\right] \Phi \ = \ 0$$

where $\Phi = S^{-1} \Psi$ is the new system wavefunction.

Our program is to now perform another canonical transformation which will eliminate H_{INT} and replace

$$\omega_p^2 \ = \ \frac{4\pi N e^2}{m}$$

with the new plasma frequency ω_B. First, we neglect the term H_{NL} since the phase factors depend on the randomly distributed electron coordinates and hence tend to cancel one another. Neglecting this term constitutes

The above designations are for:

H_F describing the plasmon field,

H_{INT} describing a linear interaction between electrons and plasmons,

H_{SR} describing the short-range part of the Coulomb interaction,

H_{NL} describing a non-linear interaction between electrons and plasmons.

The subsidiary conditions are also transformed from $\underline{P}_k\bar{\Psi}$ to

$$(S^{-1}\underline{P}_k S)\ (S^{-1}\bar{\Psi}) \ = \ 0$$

or

$$\left[\underline{P}_k - iM_k\rho_k^*\right]\Phi \ = \ 0$$

where $\Phi = S^{-1}\Psi$ is the new system wavefunction.

Our program is to now perform another canonical transformation which will eliminate H_{INT} and replace

$$\omega_p^2 \ = \ \frac{4\pi Ne^2}{m}$$

with the new plasma frequency ω_B. First, we neglect the term H_{NL} since the phase factors depend on the randomly distributed electron coordinates and hence tend to cancel one another. Neglecting this term constitutes

the random-phase-approximation always employed early on a collective-type calculation. The Hamiltonian will then describe two systems:

1) n electrons interacting through a short-range Coulomb interaction
2) a collection of plasmons of maximum wavevector k_c interacting via H_{INT} with the individual electrons

We write the new Hamiltonian as

$$H = H_o + H_F + H_{INT} + H_{SR} + \frac{1}{2} \sum_{k<k_c} (\omega_p^2 - \omega_B^2) Q_k^* Q_k - \frac{1}{2} \sum_{k<k_c} NM_k^2 \quad \text{(A-8)}$$

and chose ω_B^2 to cancel the terms

$$\frac{1}{2} \sum_{k<k_c} \left(\omega_p^2 - \omega_B^2\right) Q_k^* Q_k$$

which we added to the Hamiltonian when redescribing H_F as

$$H_F = \frac{1}{2} \sum_{k<k_c} \left[P_k^* P_k + \omega_B^2 Q_k^* Q_k \right] . \quad \text{(A-9)}$$

A perturbation expansion of any operator O_{old} is made

$$O_{old} = O_{new} + \frac{i}{h} \left[Q_{new}, S' \right] - \frac{1}{2\hbar^2} \left[\left[O_{new}, S' \right], S' \right] + \ldots \quad \text{(A-10)}$$

so we want to choose S' such that

$$\frac{i}{\hbar}\left[H_0 + H_F, S'\right] = - H_{INT}$$

i.e., cancel H_{INT} to zeroth order. Furthermore, the second-order terms from $H_0 + H_F$ just cancel one-half of the first-order terms arising from H_{INT}. This can be seen by considering

$$H_{new} = \left(H_0^{new}\right) + \left(H_F^{new}\right) + \left(H_{INT}^{new}\right) + \frac{i}{\hbar}\left[\left(H_0^{new} + H_F\right), S'\right] + \frac{i}{\hbar}\left[\left(H_{INT}^{new}\right), S'\right]$$

$$- \frac{1}{2}\hbar^2\left[\left[\left(H_0^{new} + H_F\right), S'\right], S'\right] - \frac{i}{2\hbar^2}\left[\left[H_{INT}, S'\right], S'\right]$$

where the terms arising from H_{SR} have been neglected. Look now at

$$- \frac{1}{2\hbar^2}\left[\left[\left(H_0^{new} + H_F\right), S'\right], S'\right] = \frac{i}{2\hbar}\left[\frac{i}{\hbar}\left[\left(H_0^{new} + H_F\right), S'\right]\right]$$

$$= - \frac{i}{2\hbar}\left[H_{INT}, S'\right]$$

since we have already agreed to choose

$$H_{INT} = - \frac{i}{\hbar}\left[\left(H_0^{new} + H_F\right), S'\right] .$$

Thus, the Hamiltonian, void of interaction terms to one-half of second-

order is

$$H = \left(H_O^{new} + H_F\right) + \frac{i}{2\hbar}\left[H_{INT}, S'\right] + \frac{1}{2}\sum_{k<k_c}(\omega_p^2 - \omega_B^2)Q_k Q_k^* - \frac{1}{2}\sum_{k<k_c} n M_k^2 \qquad (A\text{-}11)$$

For this canonical transformation, we choose

$$S' = \sum_{k<k_c}(A_k P_k^* + B_k Q_k)$$

where A_k and B_k are unknown electron operators. Thus if

$$(A_k)_{mn} = M_R \frac{-i\omega_{mn}}{\omega_B^2 - \omega_{mn}^2}(\rho_k)_{mn} ,$$

and

$$(B_k)_{mn} = M_R \frac{-\omega_{mn}^2}{\omega_B^2 - \omega_{mn}^2}(\rho_k)_{mn} ,$$

we will have

$$\left[H_O, S'\right]_{mn} = \left[\sum_i \left(\frac{P_i^2}{2m} + V(r_i)\right), S'\right]_{mn}$$

$$= \sum_{k<k_c} M_R \left[\frac{-i\hbar\omega_{mn}^2}{\omega_B^2 - \omega_{mn}^2} (\rho_k)_{mn} \underline{P}_k^* - \frac{\hbar\omega_{mn}^3}{\omega_B^2 - \omega_{mn}^2} (\rho_k)_{mn} Q_k \right] .$$

Here, we have used the fact that

$$[H_O, \rho_k]_{mn} = \left\{ \sum_i \frac{\hbar \underline{k}}{m} (\underline{P}_i + \hbar \underline{k}) \, e^{- i\underline{k} \cdot \underline{r}_i} \right\}_{mn}$$

$$= \hbar\omega_{mn} (\rho_k)_{mn} ,$$

$$[H_F, S']_{mn} = \left[\frac{1}{2} \sum_{\ell<k_c} (\underline{P}_\ell^* \underline{P}_\ell + \omega_B^2 Q_k^* Q_k), \sum_{k<k_c} A_k \underline{P}_k^* + B_k Q_k \right]$$

$$= \frac{1}{2} \sum_{\ell<k_c} \left[\underline{P}_\ell^* \underline{P}_\ell, \sum_{k<k_c} B_k Q_k \right] + \frac{1}{2} \sum_{\ell<k_c} \left[\omega_B^2 Q_k^* Q_k, \sum_{k<k_c} A_k P_k^* \right] .$$

Evaluating these commutators gives

$$[P_\ell^* P_\ell, \sum_{k<k_c} B_k Q_k] = [P_{-\ell} P_\ell, \sum_{k<k_c} B_k Q_k]$$

$$= - i\hbar \, [P_{-\ell} B_\ell + P_\ell B_{-\ell}] ,$$

and

$$\left[Q_{-\ell} Q_{\ell}, \sum_{k<k_c} A_k \underline{P}_{-k} \right] = i\hbar \left[Q_{\ell}^* A_{-\ell} + Q_{\ell} A_{\ell} \right] .$$

Thus,

$$\left[H_O + H_F, S' \right]_{mn} = \frac{1}{2} \sum_{\ell<k_c} \underline{P}_{\ell}^* M_{\ell} \frac{i\hbar\omega_{mn}^2}{\omega_B^2 - \omega_{mn}^2} (\rho\ell)_{mn} \qquad \text{(A-12)}$$

$$+ \frac{1}{2} \sum_{\ell<k_c} \underline{P}_{\ell} M_{\ell} \frac{i\hbar\omega_{mn}^2}{\omega_B^2 - \omega_{mn}^2} (\rho_{-\ell})_{mn}$$

$$+ \frac{1}{2} \sum_{\ell<k_c} \omega_B^2 Q_{\ell}^* M_{\ell} \frac{\hbar\omega_{mn}}{\omega_B^2 - \omega_{mn}^2} (\rho_{-\ell})_{mn}$$

$$+ \frac{1}{2} \sum_{\ell<k_c} \omega_B^2 Q_{\ell} M_{\ell} \frac{\hbar\omega_{mn}}{\omega_B^2 - \omega_{mn}^2} (\rho_{-\ell})_{mn}$$

$$- \sum_{k<k_c} P_k^* M_k \frac{\hbar\omega_{mn}^2}{\omega_B^2 - \omega_{mn}^2} (\rho_k)_{mn}$$

$$- \sum_{k<k_c} Q_k M_k \frac{\hbar\omega_{mn}^3}{\omega_B^2 - \omega_{mn}^2} (\rho_k)_{mn}$$

$$= \sum_{k<k_c} M_k \hbar \omega_B^2 \frac{\omega_{mn}}{\omega_B^2 - \omega_{MN}^2} (\rho_k)_{mn} Q_k$$

$$- \sum_{k<k_c} M_k \hbar \omega_{mn}^2 \frac{\omega_{mn}}{\omega_B^2 - \omega_{mn}^2} (\rho_k)_{mn} Q_k$$

So, finally,

$$\left[H_O + H_F, S'\right] = \sum_{k<k_c} M_k \hbar \omega_{mn} (\rho_k)_{mn} Q_k \quad . \tag{A-13}$$

We wanted this commutator to equal

$$(i\hbar H_{INT})_{mn}$$

or

$$i\hbar \left[\frac{1}{2m} \sum_i \sum_{k<k_c} \underline{k} \cdot (\underline{P}_i - \hbar \underline{k}) M_k Q_k e^{i\underline{k} \cdot \underline{r}_i}\right]_{mn}$$

$$= i\hbar \left[\sum_{k<k_c} -i \frac{M_k}{\hbar} [H_O, \rho_k] Q_k \right]_{mn} = \sum_{k<k_c} M_k Q_k \hbar \omega_{mn} (\rho_k)_{mn} \quad .$$

These expressions for $[H_O + H_F, S']$ and $(i\hbar H_{INT})$ have equal matrix elements, so the choice of A_k and B_k does satisfy the previously mentioned

$$= \sum_{k<k_c} M_k \hbar \omega_B^2 \frac{\omega_{mn}}{\omega_B^2 - \omega_{mn}^2} (\rho_k)_{mn} Q_k$$

$$- \sum_{k<k_c} M_k \hbar \omega_{mn}^2 \frac{\omega_{mn}}{\omega_B^2 - \omega_{mn}^2} (\rho_k)_{mn} Q_k$$

So, finally,

$$\left[H_O + H_F, S'\right] = \sum_{k<k_c} M_k \hbar \omega_{mn} (\rho_k)_{mn} Q_k \quad . \tag{A-13}$$

We wanted this commutator to equal

$$(i\hbar H_{INT})_{mn}$$

or

$$i\hbar \left[\frac{1}{2m} \sum_i \sum_{k<k_c} \underline{k} \cdot (\underline{P}_i - \hbar \underline{k}) M_k Q_k e^{i\underline{k} \cdot \underline{r}_i}\right]_{mn}$$

$$= i\hbar \left[\sum_{k<k_c} -i \frac{M_k}{\hbar} [H_o, \rho_k] Q_k\right]_{mn} = \sum_{k<k_c} M_k Q_k \hbar \omega_{mn} (\rho_k)_{mn} \quad .$$

These expressions for $[H_o + H_F, S']$ and $(i\hbar H_{INT})$ have equal matrix elements, so the choice of A_k and B_k does satisfy the previously mentioned

requirements on $[H_o + H_F, S']$ as long as $\omega_{mn}^2 \neq \omega_B^2$. In order to allow for this possibility, we must split all electron operators, X, into two parts

$$X = \bar{X} + \tilde{X}$$

where $\bar{X}$ is defined by

$$\bar{X}_{mn} = X_{mn} \quad \text{if} \quad |(|\omega_{mn}| - |\omega|)| > n$$

$$\bar{X}_{mn} = 0 \quad \text{if} \quad |(|\omega_{mn}| - |\omega|)| < n$$

where n will be related to the plasmon lifetime. We must also replace S' by

$$\bar{S}' = \sum_{k<k_c} \left\{ \bar{A}_k \underline{P}_{-k} + \bar{B}_k Q_k \right\}$$

in which event, the H_{INT} in the second-order term is unaffected and we have

$$H = \overset{\text{new}}{(H_o)} + \overset{\text{new}}{(H_F)} + \frac{i}{2\hbar} [\bar{H}_{INT}, \bar{S}'] + \frac{i}{\hbar} [\tilde{H}_{INT}, \bar{S}'] \qquad \text{(A-14)}$$

Now, H_{INT} has the form $V_k Q_k$ where V_k is an electron operator, so

$$H_{INT} = (\bar{V}_k + \tilde{V}_k)\, Q_k$$

and we can write the second-order terms as

$$\frac{i}{2\hbar}[\bar{H}, S'] + \frac{i}{\hbar}[\tilde{H}_{INT}, \bar{S}'] \tag{A-15}$$

$$= \frac{i}{4\hbar} \sum_{k,\ell<k_c} (2\bar{V}_\ell + 4\tilde{V}_\ell)\, \bar{A}_k Q_\ell P_{-k} - \bar{A}_k (2\bar{V}_\ell + 4\tilde{V}_\ell)\, P_{-k} Q_\ell$$

$$+ 2Q_k Q_\ell [V_\ell + \tilde{V}_\ell, \bar{B}_k]$$

$$= \frac{i}{4\hbar} \sum_{k,\ell<k_c} 2[(V_\ell + \tilde{V}_\ell), \bar{A}_k] \{Q_\ell, \underline{P}_{-k}\} + 2[Q_\ell, \underline{P}_{-k}] \{V_\ell + \tilde{V}_\ell, A_k\}$$

$$- Q_k \underline{P}_{-k}\, 2(V_\ell + \tilde{V}_\ell)\bar{A}_k + \underline{P}_k Q_\ell A_k 2(V_\ell + \tilde{V}_\ell) + 2Q_k Q_\ell [V_\ell + \tilde{V}_\ell, \bar{B}_k]$$

$$= \frac{i}{4\hbar} \sum_{k,\ell<k_c} [V_k + \tilde{V}_k, \bar{A}_k] \{Q_k, \underline{P}_{-\ell}\} + [Q_k, \underline{P}_{-\ell}] \{V_k + \tilde{V}_k, \bar{A}_k\}$$

$$+ 2Q_k Q_\ell [V_k + \tilde{V}_k, B] \quad ,$$

where the curly brackets indicate anticommutation relations.

Thus,

$$\frac{i}{2\hbar}[\bar{H}, \bar{S}'] + \frac{i}{\hbar}[\widetilde{H}_{INT}, \bar{S}']$$

$$= \frac{i}{4\hbar}\sum_{k,\ell<k_c}\left\{(Q_k\underline{P}_{-\ell} + \underline{P}_{-\ell})[V_k + \widetilde{V}_k, \bar{A}_{-k}]\right.$$

$$+ 2Q_kQ_\ell[V_k + \widetilde{V}_k, B_{-k}]$$

$$\left. - \frac{1}{4}\sum_{k<k_c}[(V_k + \widetilde{V}_k)\bar{A}_{-k} + \bar{A}_{-k}(V_k + \widetilde{V}_k)]\right. ,$$

where the second term is a screened long-range electron interaction, independent of the plasmons. The first term is quadratic in the plasmon variables, and we shall choose it to cancel the original leftover terms,

$$\frac{1}{2}\sum_{k<k_c}(\omega_p^2 - \omega_B^2)\,Q_kQ_k^* \quad .$$

Separating the sum into two parts with $\underline{l} = -\underline{k}$ and $\underline{l} \neq -\underline{k}$, we get for $\underline{l} = -k$,

$$\frac{1}{4\hbar}\sum_{k<k_c}\left\{(Q_k\underline{P}_k + \underline{P}_kQ_k)[V_k + \widetilde{V}_k, \bar{A}_{-k}] + 2Q_kQ_{-k}[V_k + \widetilde{V}_k, \bar{B}_{-k}]\right\}$$

We now evaluate the commutators for the diagonal elements:

$$[V_k, \bar{A}_{-k}]_{oo} = \sum_P (V_k)_{op} (\bar{A}_{-k})_{po} - \sum_P (\bar{A}_{-k})_{op} (V_k)_{po}$$

$$= \sum_P M_k^2 \frac{\omega_{po}^2}{\omega_B^2 - \omega_{po}^2} \left[(\rho_k)_{op} (\rho_k)_{po} - (\rho_k)_{po} \right]$$

$$= 0$$

so there are no cross-terms in plasmon variables in the diagonal elements.

Similarly,

$$\left[V_k, B_{-k} \right]_{oo} = \sum_P (V_k)_{op} (\underline{B}_k)_{po} - \sum_P (B_{-k})_{op} (V_k)_{po}$$

$$= -2i \sum_P M_k^2 \frac{\omega_{po}^3}{\omega_B^2 - \omega_{po}^2} (\rho_k)_{op}^2 .$$

Thus, the electron-plasmon part of the Hamiltonian is

$$H_{EP} = \left[\frac{i}{4\hbar} \sum_{k<k_c} (-2i) \sum_P \frac{4\pi e^2}{k^2} \omega_{po}^2 (\rho_k)_{op}^2 \frac{\omega_{po}^2}{\omega_B^2 - \omega_{po}^2} \right] 2Q_k Q_{-k} \tag{A-16}$$

$$= \sum_{k<k_c} \left\{ \frac{\omega_p^2}{N} \sum_P \left[f_{op}(k) \frac{\omega_{po}^2}{\omega_B^2 - \omega_{po}^2} \right] \right\} \frac{Q_k Q_{-k}}{2}$$

recalling that

$$f_{op}(k) = \frac{2m}{\hbar k^2} \omega_{po} \left| (\rho_k)_{op} \right|^2 \quad \text{and} \quad \omega_p^2 = \frac{4\pi N e^2}{m} \quad .$$

The frequency ω_B at which the plasma oscillates is then found by setting

$$H_{EP} = -\frac{1}{2} \sum_{k<k_c} (\omega_p^2 - \omega_B^2) \, Q_k Q_{-k}$$

or

$$\omega_B^2 - \omega_p^2 - \frac{\omega_p^2}{N} \sum_n f_{on}(k) \frac{\omega_{on}^2}{\omega_B^2 - \omega_{on}^2} = 0 \quad .$$

Rewriting this gives

$$\omega_B^2 - \omega_p^2 + \frac{\omega_p^2}{N} \sum_n f_{on}(k) \left(\frac{\omega_B^2 - \omega_{on}^2}{\omega_B^2 - \omega_{on}^2} \right) - \frac{\omega_p^2}{N} \sum_n f_{on} \left(\frac{\omega_B^2}{\omega_B^2 - \omega_{on}^2} \right) = 0$$

or

$$\omega_B^2 - \omega_p^2 \frac{1}{N} \sum_n f_{on} \frac{\omega_p^2}{\omega_B^2 - \omega_{on}^2} \qquad \text{(A-17)}$$

since

$$\sum_n f_{on}(k) = N \quad .$$

Thus we must have

$$\sum_n f_{on}(k) \frac{\omega_p^2}{\omega_B^2 - \omega_{on}} = N$$

or

$$1 = \frac{\omega_p^2}{N} \sum_n \frac{f_{on}}{\omega_B^2 - \omega_{on}^2} \qquad \text{(A-18)}$$

as the plasmon dispersion relation considering the plasmon-electron interaction.

APPENDIX B

ELECTRON ENERGY STATES IN A DISORDERED CRYSTAL

The motion of electrons in a disordered system can be treated by a perturbation technique in which the perturbing force arises from randomly distributed scattering centers. The unperturbed Hamiltonian H_o, represents the electrons in a periodic field where orthonormal Bloch functions, $\psi_k(r)$, describe individual electronic states of energy E_k. The essence of the perturbation calculation consists of finding formulae for the energies, wavefunctions, and density of stationary states in terms of the known energy values and wavefunctions of the unperturbed system. The Green's function formalism has proved very useful in these efforts.[41]

The Schroedinger equation describing electronic motion in a periodic potential $V_o(r) = V_o(r + R)$ is

$$\left(\frac{\hbar}{i}\frac{\partial}{\partial t} - \frac{h^2}{2m}\nabla^2 + V_o(r)\right)\psi(r,t) = 0 \ . \qquad \text{(B-1)}$$

The Green's function G_o of the operator H_o is the kernel of the integral operator which inverts H_o and is thus a solution of

$$\left(\frac{\hbar}{i}\frac{\partial}{\partial t} - \frac{h^2}{2m}\nabla^2 + V_o(r)\right) G_o(r,r';t,t') = \delta(r-r')\delta(t-t') \ . \qquad \text{(B-2)}$$

Substitution verifys that

$$G_o(r,r';t,t') = \frac{i}{\hbar} \sum_k \psi_k(r)\psi_k^*(r')e^{-\frac{i}{\hbar}E_k(t - t')}\theta(t - t') \qquad \text{(B-3)}$$

is a solution of this equation where $\psi_k(r)$ are Bloch solutions of the Schroedinger equation, and where

$$\theta = 1, \quad t > t'$$

$$\theta = 0, \quad t < t'.$$

G_o can be expressed in terms of energy E by Fourier transforming with respect to $(t - t')$:

$$G_o(r,r';E) = \frac{i}{\hbar} \sum_k \int_o^\infty \psi_k(r)\psi_k^*(r')e^{-\frac{i}{\hbar}E_k(t - t')} e^{\frac{i}{\hbar}E(t - t')} d(t-t') \qquad \text{(B-4)}$$

$$= \frac{i}{\hbar} \sum_k \int \psi_k(r)\psi_k^*(r')e^{\frac{i}{\hbar}(E - E_k)(t - t')} d(t-t')$$

$$= \frac{i}{\hbar} \sum_k \frac{\psi_k(r)\,\psi_k^*(r')}{E - E_k + i\epsilon}$$

The $i\epsilon$ in the denominator is necessary to define the direction in which the pole at $E - E_k$ is to be taken; the sign is chosen so that the solution corresponds to outgoing waves. Fourier space proves to be most useful for performing these calculations: the transformation to k-space is given by

$$G_o(\ell,m;E) = \int G_o(r,r';E)\psi_\ell^*(r)\psi_m(r')\, drdr' \qquad \text{(B-5)}$$

$$= \sum_k \frac{\delta_{k\ell}\delta_{km}}{E - E_k + i\epsilon}$$

so that

$$G_o(k,k;E) = \frac{1}{E - E_k + i\epsilon} \qquad \text{(B-6)}$$

In a disordered crystal, the potential $V(r)$ arises from N positive ionic charges randomly distributed through a unit volume. If the electron-electron interactions are assumed to be accounted for by screening the ionic charges, the potential $V(r)$ can be represented as a sum over all the atomic positions R_α; thus

$$V(r) = \sum_\alpha U(r - R_\alpha) \, .$$

The periodic potential results are carried straightforwardly into this problem except the eigenfunctions used are solutions of

$$\left(\frac{\hbar}{i}\frac{\partial}{\partial t} - \frac{\hbar^2}{2m}\nabla^2 + \sum_{\alpha} U(r - R_{\alpha})\right)\psi_n = 0 . \tag{B-7}$$

For the field defined by V(r), the Green's function G(r,r';E) is given by

$$\left(\frac{\hbar}{i}\frac{\partial}{\partial t} - \frac{\hbar^2}{2m}\nabla^2 + \sum_{\alpha} U(r-R_{\alpha})\right) G(r,r';t,t') = \delta(r-r')\delta(t-t') . \tag{B-8}$$

Hence

$$G(r,r';E) = \sum_{n} \frac{\psi_n(r)\psi_n^*(r')}{E - E_n + i\epsilon} \tag{B-9}$$

and

$$G(k,k;E) = \int\int \sum \frac{\psi_n(r)\psi_n^*(r)}{E - E_n + i\epsilon}\, \psi_k^*(r)\, \psi_k(r')\, dr dr' \tag{B-10}$$

$$= \sum_{n} \frac{1}{E - E_n + i\epsilon} \int \psi_n(r)\psi_k^*(r)\, dr \int \psi_n^*(r')\psi_k(r')\, dr'$$

$$= \sum_n \frac{|\Phi_n(k)|^2}{E - E_n + i\epsilon}$$

where

$$\Phi_n(k) = \int \psi_n(r)\psi_k^*(r)dr$$

is the wavefunction of the state n in k-space. These Φ's are normalized for

$$\frac{1}{(2\pi)^3}\int |\Phi_n(k)|^2\, dk = \frac{1}{(2\pi)^3}\int \psi_n^*(r)\, drdr' \int \psi_k^*(r)\psi_k(r')\, dk$$

$$= \int \psi_n(r)\, \psi_n^*(r')\, drdr'\, \delta(r - r')$$

$$= \int |\psi_n(r)|^2\, dr = 1 \quad .$$

Therefore,

$$\frac{1}{(2\pi)^3}\int G(k,k;E)\, dk = \sum_n \frac{1}{E - E_n + i\epsilon} \qquad \text{(B-11)}$$

and if the sum over states can be replaced by an integral, a density of states $N(E_n)$ appears. That is,

$$\int G(k,k;E)\,\frac{dk}{(2\pi)^3} = \int \frac{N(E_n)\,d\,E_n}{E - E_n + i\varepsilon} \qquad \text{(B-12)}$$

The right hand side can be evaluated to give N(E) by letting $\varepsilon \to 0$ and using the relation

$$\lim_{\varepsilon \to +0} \frac{1}{\lambda \pm i\varepsilon} = \frac{P}{\lambda} \mp i\pi\delta(\lambda), \qquad \text{(B-13)}$$

where P indicates principal value. Taking the imaginary part of both sides gives

$$N(E) = -\frac{1}{8\pi^4}\,\mathrm{Im}\int G(k,k;E)dk\ . \qquad \text{(B-14)}$$

Later the approximation that G depends only on k through the energy E_k will be made; it is convenient, then, to transform from the integration over dk to an integration over energy. This is done by writing $dk = dS_n dk_\perp$ where dS_n is an element of area on the constant energy surface $E_n(k) = E$ and $k_\perp$ is the component of k normal to this surface. Because $\nabla_k E_n$ is also normal to this energy surface, $dE_k = |\nabla_k E_n| dk_\perp$, so that

$$N(E) = -\frac{\mathrm{Im}}{8\pi^4} \int_{E_n=E} \int G(E_k;E)\,\frac{dS_n dE_k}{|\nabla_k E_n|} \qquad \text{(B-15)}$$

In the periodic field the density of states $N_o(E)$ not counting spin is given by

$$N_o(E_k) = \frac{Im}{8\pi^3} \int_{E_n=E_k} \frac{dS_n}{|\nabla_k E_n|} \tag{B-16}$$

so in terms of the unperturbed density of states, the density of states in the disordered crystal is given by

$$N(E) = \frac{Im}{\pi} \int G(E_k,E) N_o(E_k) dE_k \ . \tag{B-17}$$

An expression for G is now needed to determine the effects of disorder on $N_o(E)$.

If E is regarded as complex, then G(k,k;E) as defined in Eq. B-11 is an analytic function of E in the region above a line parallel to the real axis and ic below the axis. If the analytical continuation of G below this line is supposed to have form

$$G(k,k;E) = \frac{1}{E - E_k - \Sigma(k,E) + i\Gamma(k,E)} \ , \tag{B-18}$$

then from Eq. B-14

$$N(E) = -\frac{Im}{i\pi^4} \int \frac{}{E - E_k - \Sigma + i\Gamma} \tag{B-19}$$

$$= \frac{1}{8\pi^4} \int \frac{\Gamma(k,E)dk}{(E - E_k + \Sigma)^2 + \Gamma^2}$$

This relation will be useful only if Σ and Γ can be determined. From the way in which they were included in Eq. B-18, an association of Σ with energy level displacement and Γ with broadening in the disordered state can be anticipated. Analytic expressions for Σ and Γ can be obtained from a perturbation calculation of G.

The calculation proceeds by noting that

$$\psi(r) = \psi_o(r) + \int G_o(r,r';E)V(r')\psi(r')dr' \qquad \text{(B-20)}$$

and

$$\psi(r) = \psi_o(r) + \int G(r,r';E)V(r')\psi_o(r')dr' \qquad \text{(B-21)}$$

as can be easily verified by applying the operators $(H_o + V_o - E + i\epsilon)$ and $(H + V - E + i\epsilon)$ to Eqs. B-20 and B-21, respectively. The results of operating on the integrals are obtained by using the equations that define the Green's functions G_o and G, Eqs. B-2 and B-8. Now, placing Eq. B-21 into Eq. B-20 gives (suppressing all variables)

$$\psi = \psi_o + \int G_o V'(\psi_o + \int GV'\psi' dr') \, dr' \qquad \text{(B-22)}$$

$$= \psi_o + \int G_o V'\psi_o dr' + \int\int G_o V' G V \psi' dr' dr'$$

$$= \psi_o + \int (G_o + G_o VG)\, V\psi_o dr'$$

so comparison with Eq. 21 yields an exact operator relation

$$G = G_o + G_o\, VG\ . \tag{B-23}$$

Next, matrix elements of G between the original unperturbed Bloch functions are found. $G(\ell, k; E)$ is determined from

$$\langle \ell | G_o + G_o VG | k \rangle = \langle \ell | G_o VG | k \rangle \tag{B-24}$$

since only the diagonal elements of G_o are nonzero in this representation. Also

$$\langle \ell | G_o VG | k \rangle = \sum_i \langle \ell | G_o | i \rangle \langle i | VG | k \rangle \tag{B-25}$$

$$= \sum_i \langle \ell | G_o | i \rangle \sum_m \langle i | V | m \rangle \langle m | G | k \rangle$$

$$= \delta_{i\ell} \langle \ell | G_o | i \rangle \sum_m \langle \ell | V | m \rangle \langle m | G | k \rangle$$

so that

$$G(\ell,k;E) = \sum_m G_o\ell,\ell;E)\ V_{\ell m}G(m,k;E) \quad . \tag{B-26}$$

The diagonal elements are similarly obtained except the G_o matrix elements do not vanish. Thus,

$$G(k,\ k;\ E) = G_o(k,\ k,\ E) + \sum_\ell G_o(k,\ k;\ E)V_{k\ell}G(\ell,k;E) \quad . \tag{B-27}$$

In order to substitute for $G(\ell,k;E)$ in Eq. B-27 from Eq. B-26, the sum in Eq. B-27 must be broken into diagonal and off-diagonal elements:

$$G(k,k;E) = G_o(k,k;E) + G_o(k,k;E)\ V_{kk}G(k,k,E) \tag{B-28}$$

$$+ \sum_{\ell\neq k} G_o(k,k;E)\ V_{k\ell}G(\ell,k;E)$$

so Eq. B-27 becomes

$$G(k,k;E) = G_o(k,k;E) + G_o(k,k;E)\ V_{kk}G(k,k;E)$$

$$+ \sum_{\ell\neq k} G_o(k,k;E)\ V_{k\ell} \sum_m G_o(\ell,\ell;E)\ V_{\ell m}G(m,k;E) \quad .$$

Thus far no approximations have been made; to proceed, however, all off-diagonal elements of G will be set to zero since they

introduce higher than second order powers of V (see Eq. B-26). To this approximation, the last equation becomes

$$G_o(k,k;E) = G(k,k;E)\left[1 - V_{kk}G_o(k,k;E) - G_o(k,k;E)\sum_{\ell\neq k} V_{k\ell}G_o(\ell,\ell;E)\right]$$

or

$$\frac{1}{G_o(k,k;E)} - V_{kk} - \sum_{\ell\neq k}^{\prime} |V_{k\ell}|^2 G_o(\ell,\ell;E) = \frac{1}{G(k,k;E)} \qquad \text{(B-30)}$$

Substituting for G and G_o from Eqs. B-18 and B-6 and taking the limit $\epsilon\to 0$ gives

$$\Sigma - i\Gamma = V_{kk} + \lim_{\epsilon\to 0} \sum_{\ell\neq k}^{\prime} \frac{|V_{k\ell}|^2}{E - E_\ell + i\epsilon} \qquad \text{(B-31)}$$

as a defining equation for Σ and Γ. Thus, an expression for N(E) has been found in terms of $N_o(E)$.

If $U(r - R_\alpha)$ represents the difference in potential energy of an electron due to displacement of the atom at R_α from its periodic lattice site, then V(r) will represent the total perturbing potential seen by the electron. The matrix elements of V can then be obtained by using Bloch functions of the periodic field V_o. Hence

$$V_{k\ell} = \sum_{\alpha} \langle \psi_{\ell} | U(r - R_{\alpha}) | \psi_{k} \rangle \tag{B-32}$$

and if r is translated to $r + R_{\alpha}$,

$$V_{k\ell} = \sum_{\alpha} e^{i(k-\ell) \cdot R_{\alpha}} \int \psi_{\ell}^{*} U(r) \psi_{k} \, dr \tag{B-33}$$

since

$$\psi_{\ell}(r + R_{\alpha}) = e^{i\ell \cdot R_{\alpha}} \psi_{\ell}(r) \quad .$$

Similarly,

$$V_{\ell k} = \sum_{\beta} \Phi_{\ell k} e^{i(\ell - k) \cdot R_{\beta}} \tag{B-34}$$

so that

$$|V_{k\ell}|^2 = |\Phi_{k\ell}|^2 \sum_{\alpha,\beta} e^{i(k - \ell) \cdot (R_{\alpha} - R_{\beta})} \tag{B-35}$$

where

$$\Phi_{k\ell} = \int \psi_\ell^* (r)\, U(r) \psi_k(r) dr \ . \qquad \text{(B-36)}$$

In order to evaluate $|V_{k\ell}|^2$, the explicit form of the $\Phi_{k\ell}$ and all atomic positions would have to be known. Clearly this information is unavailable; however, certain general properties of $|V_{k\ell}|^2$ can still be inferred. If the disordered crystal were to form a superlattice, then the sum in Eq. B-35 would add to zero for arbitrary $k - \ell$. In the special case that $k - \ell$ formed a reciprocal superlattice vector, each term in the sum would be unity and the entire sum would equal N^2, where N is the number of atoms per unit volume. In general, $k - \ell$ is not a reciprocal lattice vector and $|V_{k\ell}|^2$ will take on values between those corresponding to the extremes of complete disorder and local order. The band structure in the solid will undergo changes in the disordered system which reflect the different possible $|V_{k\ell}|^2$.

In Eq. B-15, the method for changing the sum over E_ℓ in Eq. B-31 into an integral over the energy range was demonstrated. Applying these results to Eq. B-31 gives

$$V_{kk} + \lim_{\epsilon \to +0} \frac{1}{(2\pi)^3} \iint \frac{|V_{k\ell}|^2}{E - E_\ell + i\epsilon} \frac{dS_\ell}{|\nabla_k E_\ell|} dE_\ell = \Sigma(k,E) - i\Gamma(k,E). \qquad \text{(B-37)}$$

By applying Eq. B-13 to evaluate the integral over dE_ℓ and defining

$$\Gamma = -F(k,E_\ell) = \frac{1}{(2\pi)^3}\int_{E_\ell} |V_{k\ell}|^2 \frac{dS_\ell}{|\nabla_k E_\ell|} , \qquad \text{(B-38)}$$

Eq. B-37 above leads to

$$\Sigma(k,E) = V_{kk} + P\int \frac{F(k,E_\ell)}{E-E_\ell} \qquad \text{(B-39)}$$

and

$$\Gamma(k,E) = \pi F(k,E_\ell) . \qquad \text{(B-40)}$$

Earlier, the way in which Σ and Γ were introduced into the expression for G lead to an association of Σ with displacement of energy levels and Γ with their broadening as disorder was increased. In general, then, from the remarks concerning $|V_{k\ell}|^2$, when a superlattice exists, $|V_{k\ell}|^2$ and hence F and Γ will be zero. Thus, there will be no level broadening although the displacement of the levels, Σ, will not vanish. The existence of a superlattice is not to be expected, however, so consider the density of states in an unperturbed system depicted below in Fig. B-1. Here, $N_o(E) = 0$ for $E_1 < E < E_o$. From Eq. B-38 $F(k,E)$ is seen to be zero since the integration is to be performed over a constant energy surface in the ordered system where $N_o(E) = 0 \approx \frac{dS}{|\nabla E|}$. Since $F \to 0$ at the band

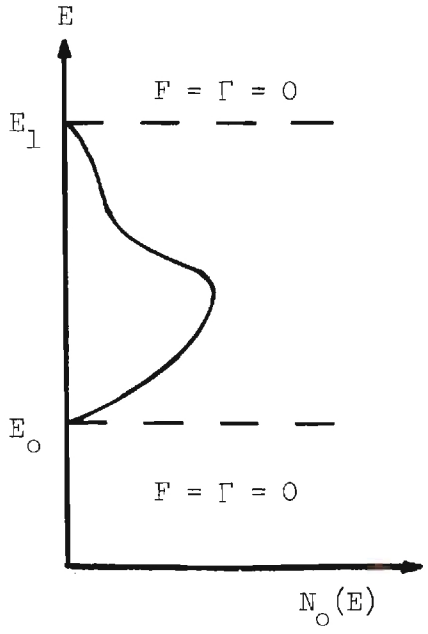

Figure B-1. Energy Band in Unperturbed System.

edges, $\Gamma \to 0$ too, and $\dfrac{\Gamma}{(E - E_k - \Sigma)^2 + \Gamma^2} \to \delta(E - E_k - \Sigma)$. Thus,

$$N(E) = \frac{1}{8\pi^3} \int_{E=E_k+\Sigma} \frac{dS}{|\nabla_k E|} \tag{B-41}$$

from Eq. B-18.

If Σ can be assumed to depend on k only through E_k, then comparison with the expression for the unperturbed density of states

$$N_o(E_k) = \frac{1}{8\pi^3} \int_{E_k=E_n} \frac{dS_n}{|\nabla_k E_n|} \tag{B-42}$$

gives $N(E) = N_o(E_k)$ where E_k is the solution of $E - E_k - \Sigma = 0$. Consequently, the largest energy $E_\rangle$ in the disordered system is obtained from the solution of

$$E_\rangle - E_1 - \Sigma(E_\rangle, E_1) = 0 \tag{B-43}$$

and the lowest energy $E_\langle$ is obtained from

$$E_\langle - E_o - \Sigma(E_\langle, E_o) = 0 . \tag{B-44}$$

The disorder in the system has thus introduced extra levels near the band edges; the sign and size of Σ determines exactly how the density of states is affected.

If $U(r - R_\alpha)$ is chosen appropriately, V_{kk} can be set to zero and then at the top of the band where $E \rangle E_\ell$, the integration involves no poles, so

$$\Sigma(E) = + P \int_{E_o}^{E_1} \frac{\langle |V_{k\ell}|^2 \rangle_{E_\ell} N_o(E_\ell) dE_\ell}{E - E_\ell} \tag{B-45}$$

$$\approx \langle |V_{k\ell}|^2 \rangle_o N_o \Delta E_o$$

where N_o is representative of the number of energy states and ΔE_o

reflects the energy bandwidth. In this case, the top of the band in the disordered system is broadened by introduction of extra energy levels located Σ above the highest energy in the ordered system. Similarly, if $E < E_o$, then

$$\Sigma(E) = - P \int_{E_o}^{E_1} \frac{\langle |V_{k\ell}|^2 \rangle_{E_\ell} N_o(E_\ell) dE_\ell}{E_\ell - E} \qquad \text{(B-46)}$$

$$\approx - \langle |V_{k\ell}|^2 \rangle_o N_o' \Delta E_o'$$

so the extra levels are introduced Σ below those in the ordered system.

From Eq. B-38, one can anticipate that the energy dependence of $F(k,E)$ is determined mainly by the character of the density of states in the unperturbed crystal. For an ideal crystal, a free-electron like density of states could be assumed to be the smooth function depicted in Fig. B-2.

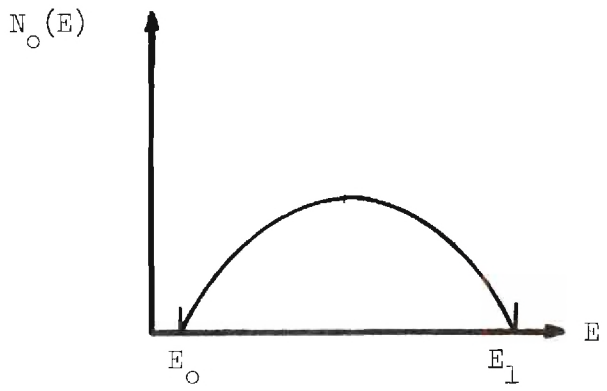

Figure B-2. Density of States in an Ideal Lattice.

The maximum in the curve will lead to a maxima in the damping, Γ, for those energy levels nearest the center of the band. Furthermore, Sergeeva has shown that, for the density of states assumed above, the behavior of the energy level displacement, Σ, is typically that shown in Fig. B-3.

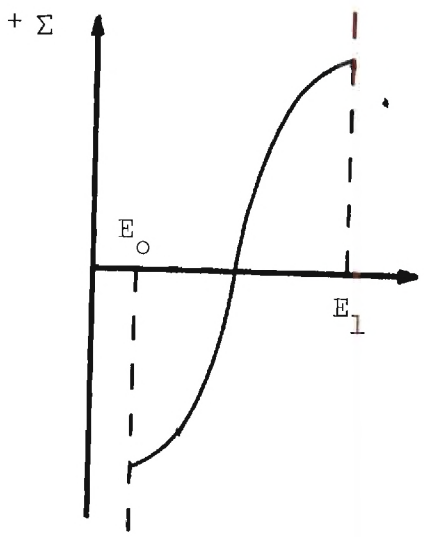

Figure B-3. Energy Level Displacement in Disordered Crystal.

For this model, then, the maximum damping and minimum displacement of energy levels in the disordered system occurs near the center of the band. Also, the minimum damping and maximum displacement occur near the band edges.

For these reasons, the density of states at any particular energy, say the Fermi level for convenience, in the disordered crystal will depend on the position of that energy in the unperturbed energy spectrum. In particular, if E_F is near the center of the band, $N(E_F)$

is reduced because of the increased broadening of the nearby energy levels. Conversely, if E_F is located near a band edge, $N(E_F)$ will be increased because the original state density is smaller than that near the center of the band.

APPENDIX C

ANALYSIS OF OPTICAL REFLECTIVITY DATA

The particular method employed in this study for obtaining the optical constants n and k was chosen to be compatible with both the existing LEED system and the dimensions of the single crystals used in the electron energy loss measurements. The optical reflectivity was obtained at two angles of incidence for photon wavelengths between 1050 and 8000 Å and these functions were simultaneously fitted by a least-squares computer program which searched the n-k plane to find the point of minimum error between the calculated and measured reflectivities. From the n and k values, the dielectric function $\epsilon(\omega)$, the energy loss function $-\mathrm{Im}(1/\epsilon)$, and the surface plasmon loss function $-\mathrm{Im}(1/1+\epsilon)$ were evaluated. These results were used to identify the surface plasmon losses in copper and nickel. In this appendix, the analytical methods necessary for treating the optical data are presented in a manner such that the most significant results and relationships remain obvious.

We want to discuss the propagation of electromagnetic waves into and through solids. The Maxwell equations

$$\nabla \cdot \underline{D} = 4\pi\rho_{free}\,, \quad \underline{D} = \underline{E} + 4\pi\underline{P} \tag{C-1}$$

$$\nabla \times \underline{E} = -\frac{1}{c}\frac{\partial \underline{B}}{\partial t}\,, \quad \underline{H} = \underline{B} - 4\pi\underline{M}$$

$$\nabla \cdot \underline{B} = 0$$

$$\nabla \times \underline{H} = \frac{1}{c} \frac{\partial \underline{B}}{\partial t} + \frac{4\pi}{c} \underline{j}_{free}$$

describe the response of the system to the disturbance. Suppose the medium is excited by monochromatic fields originating in external sources, and make the simplifying assumptions that all the macroscopic vectors $\underline{E}$, $\underline{P}$, $\underline{B}$, $\underline{M}$, and $\underline{j}_{free}$ oscillate sinusoidally at each point with the frequency of the incident fields. We then have the complex representation

$$\underline{E} = \underline{E}_s e^{-i\omega t} \quad , \quad \underline{P} = \underline{P}_s e^{-i\omega t} \quad , \quad \underline{j}_{free} = \underline{j}_s e^{-i\omega t}$$

and assume that at each point of the medium

$$\underline{P}_s = X_e \underline{E}_s, \quad \underline{M}_s = X_m \underline{H}_s, \quad \underline{j} = \sigma \underline{E}_s$$

This implies that the electric and magnetic polarization depend, respectively, only on the electric and magnetic field and that the free current density also depends only on the electric field. In general, these assumptions are not valid but in the absence of strong static fields, they are acceptable. Furthermore, the susceptibilities and conductivity above are in general complex, so that $\underline{P}$ and $\underline{E}$, say, do not oscillate with the same phase. In particular, they depend on frequency and density.

We first rewrite Maxwell's equations with only E and H and then eliminate H to obtain a description of E. If we assume time independent solutions of form

$$\underline{E}_s = \underline{E}_o e^{i\underline{k}_c \cdot \underline{r}} , \quad \underline{H}_s = \underline{H}_o e^{i\underline{k}_c \cdot \underline{r}} \tag{C-2}$$

and note that

$$\nabla \cdot (\underline{c} e^{i\underline{k} \cdot \underline{r}}) = i\underline{k} \cdot \underline{c} e^{i\underline{k} \cdot \underline{r}}$$

and

$$\nabla \times (\underline{c} e^{i\underline{k} \cdot \underline{r}}) = i\underline{k} \times \underline{c} e^{i\underline{k} \cdot \underline{r}}$$

then the Maxwell equations reduce to

$$\underline{k}_c \cdot \underline{E}_o = 0 , \quad \underline{k}_c \cdot \underline{H}_o = 0 \tag{C-3}$$

$$\underline{k}_c \times \underline{E}_o = \frac{\omega\mu}{c} \underline{H}_o \tag{C-4}$$

$$\underline{k}_c \times \underline{H}_o = - \left(\epsilon + i \frac{4\pi\sigma}{\omega}\right) \frac{\omega}{c} \underline{E}_o \tag{C-5}$$

Now, substituting for $\underline{H}_o$ from (C-4) into (C-5) gives

$$(\underline{k}_c \cdot \underline{k}_c)\ \underline{E}_o = \mu(\epsilon + i\,\frac{4\pi\sigma}{\omega})\,\frac{\omega^2}{c^2}\,\underline{E}_o$$

so

$$k_c \cdot k_c = n_c^2\, k_o^2$$

where

$$k_o = \frac{\omega}{c}\,, \quad n_c^2 = \epsilon\mu + i\,\frac{4\pi\sigma\mu}{\omega}\ .$$

We call k_o the vacuum wave number, and n_c the complex refractive index of the medium. We indicate the real and imaginary parts of these quantities by $n_c = n + i\chi$, $\underline{k}_c = k + i\underline{a}$, so that

$$k^2 - a^2 = k_o^2(n^2 - k^2) \tag{C-6}$$

$$\underline{k} \cdot \underline{a} = k_o^2\, nk$$

These terms are: n, the refractive index; χ, the extinction index; $\underline{k}$, the wave vector; and $\underline{a}$, the attenuation vector.

When electromagnetic waves pass from one medium into another, certain boundary conditions must be satisfied, giving rise to the phenomena of reflection and refraction. In the case of radiation on incident

upon a boundary containing no currents or charges of external origin, the boundary conditions are that the normal components of B and D are continuous and that the tangential components of E and H are continuous. In order to satisfy these conditions, it is necessary to assume the existence of a reflected wave in the first medium and of a transmitted wave in the second. We write

$$\underline{E} = \mathrm{Re}\left[\tilde{\underline{E}}_o e^{i(\tilde{\underline{k}}\cdot\underline{r}-\omega t)}\right] \quad \text{for the incident wave}$$

$$\underline{E}' = \mathrm{Re}\left[\tilde{\underline{E}}'_o e^{i(\tilde{\underline{k}}'\cdot\underline{r}-\omega t)}\right] \quad \text{for the transmitted wave, and}$$

$$\underline{E}'' = \mathrm{Re}\left[\tilde{\underline{E}}_o e^{i(\tilde{\underline{k}}''\cdot\underline{r}-\omega t)}\right] \quad \text{for the reflected wave .}$$

The similar time dependence follows from the requirement that the boundary conditions must be satisfied at all points on the boundary at all times.

From Maxwell's equations, we can write the boundary conditions as

$$\underline{n}\cdot[\tilde{\epsilon}_A\tilde{\underline{E}}_A - \tilde{\epsilon}_B\tilde{\underline{E}}_B] = 0 \qquad \text{(C-7)}$$

$$\underline{n}\cdot[\tilde{\mu}_A\tilde{\underline{H}}_A - \tilde{\mu}_B\tilde{\underline{H}}_B] = 0 \qquad \text{(C-8)}$$

$$n\times[\tilde{\underline{E}}_A - \tilde{\underline{E}}_B] = 0 \qquad \text{(C-9)}$$

$$\underline{n} \times [\underset{\sim}{\underline{H}}_A - \underset{\sim}{\underline{H}}_B] = 0 \qquad \text{(C-10)}$$

If we go back to equations (C-4) and (C-5) and recall that we are restricting ourselves to boundaries where there are no free charges we can rewrite (C-4) as $k \times E = \omega\mu H$ so (C-10) above becomes

$$\underline{n} \times [\underset{\sim}{\underline{H}}_o + \underset{\sim}{\underline{H}}_o'' - \underset{\sim}{\underline{H}}_o'] = 0$$

or

$$\underline{n} \times [(\underset{\sim}{\underline{k}} \times \underset{\sim}{\underline{E}}_o') + (\underset{\sim}{\underline{k}}'' \times \underset{\sim}{\underline{E}}_o'') - (\underset{\sim}{\underline{k}}' \times \underset{\sim}{\underline{E}}_o')] = 0$$

$$\underset{\sim}{\underline{k}}(\underline{n} \cdot \underset{\sim}{\underline{E}}_o) - \underset{\sim}{\underline{E}}_o(\underline{n} \cdot \underset{\sim}{\underline{k}}) + \underset{\sim}{\underline{k}}''(\underline{n} \cdot \underset{\sim}{\underline{E}}_o'') - \underset{\sim}{\underline{E}}_o''(\underline{n} \cdot \underset{\sim}{\underline{k}}'')$$

$$- \underset{\sim}{\underline{k}}'(\underline{n} \cdot \underset{\sim}{\underline{E}}_o') + \underset{\sim}{\underline{E}}_o'(\underline{n} \cdot \underset{\sim}{\underline{k}}') = 0$$

Now consider the case when the electric field is polarized perpendicular to the plane of incidence. The terms $(\underline{n} \cdot \underline{k})$ will vanish and we are led to

$$k_y(E_{os} - E_{os}'') = k_y' E_{os}' \qquad \text{(C-11)}$$

and $E_{os} + E_{os}'' = E_{os}'$ from equation (C-10). Here we have made use of the fact that

$$(\tilde{\underline{k}} \cdot \underline{n}) = -(\tilde{\underline{k}}' \cdot \underline{n})$$

since the phase factors of all the fields must be equal there and we have already shown the time dependence to be the same. If we look at a diagram for the case when $\underline{E}$ is perpendicular to the plane of incidence, Figure C-1 below, it then follows that the components of $\underline{k}$, $\underline{k}'$, $\underline{k}''$, in the boundary plane must be equal so $\tilde{\underline{k}} \times \underline{n} = \tilde{\underline{k}}' \times \underline{n} = \tilde{\underline{k}}'' \times \underline{n}$ or $\tilde{\underline{k}}_x = \tilde{\underline{k}}_x' = \tilde{\underline{k}}_x''$ in Figure C-1.

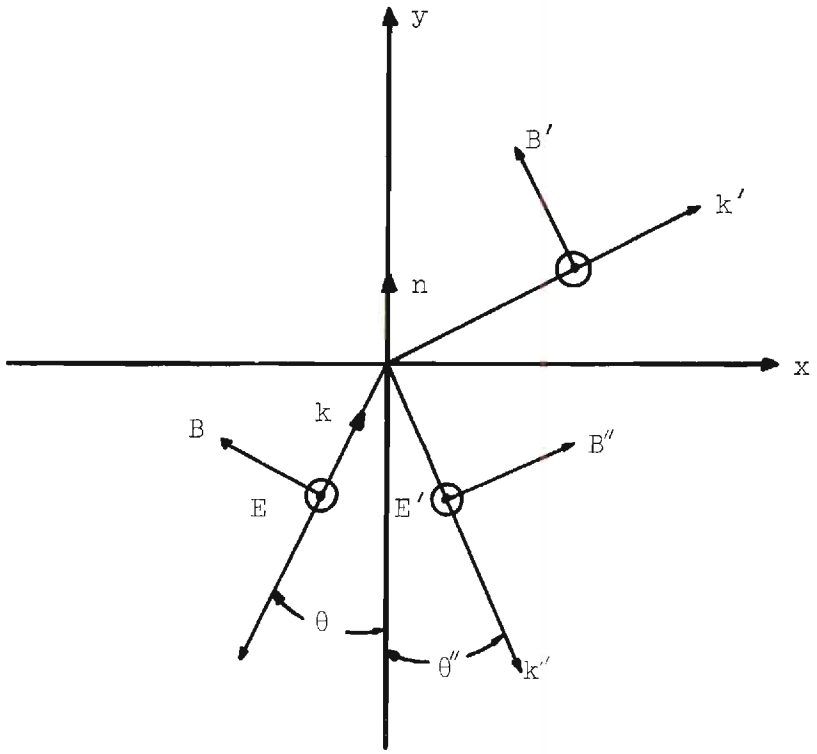

Figure C-1. Incident Electric Field Perpendicular to the Plane of Incidence.

Now, the amplitude reflection coefficient r_s and the amplitude transmission coefficient t_s are defined by

$$\tilde{E}_{os}'' = \tilde{r}_s \tilde{E}_{os} \,, \quad \tilde{E}_{os}' = \tilde{t}_s \tilde{E}_{os} \tag{C-12}$$

so for the case of perpendicular incidence considered here

$$\tilde{r}_s = \frac{\tilde{E}_{os}''}{\tilde{E}_{os}} = \frac{\tilde{k}_y - \tilde{k}_y'}{\tilde{k}_y + \tilde{k}_y'} \tag{C-13}$$

since

$$\tilde{k}_y(\tilde{E}_{os} - \tilde{E}_{os}'') = \tilde{k}_y'(\tilde{E}_{os} + \tilde{E}_{os}'')$$

or

$$\tilde{E}_{os}'' = \tilde{E}_{os}\left(\frac{\tilde{k}_y - \tilde{k}_y'}{\tilde{k}_y + \tilde{k}_y''}\right)$$

Also,

$$\tilde{t}_s = \frac{\tilde{E}_{os}'}{\tilde{E}_{os}} = \frac{2\tilde{k}_y}{\tilde{k}_y + \tilde{k}_y'} = 1 + \tilde{r}_s \tag{C-14}$$

since

$$\tilde{k}_y'\tilde{E}_{os}' = \tilde{k}_y(2\tilde{E}_{os} - \tilde{E}_{os}')$$

or

$$E_{os}' = \frac{2\tilde{k}_y \tilde{E}_{os}}{\tilde{k}_y + \tilde{k}_y'}$$

When the electric field vector lies in the plane of incidence, it is more convenient to make the calculation in terms of the magnetic field vector which is then perpendicular to the plane. Proceeding in a manner exactly as above, we find

$$\tilde{H}_{os}'' = \tilde{r}_p \tilde{H}_{os} \tag{C-15}$$

$$\tilde{H}_{os}' = \tilde{t}_p \tilde{H}_{os}$$

where

$$\tilde{r}_p = \frac{\tilde{k}_y - \tilde{k}_y'}{\tilde{k}_y + \tilde{k}_y'} \tag{C-16}$$

and

$$\tilde{t}_p = \frac{2\tilde{k}_y}{\tilde{k}_y + \tilde{k}_y'} = 1 + \tilde{r}_p \tag{C-17}$$

The general case of elliptical polarization can be handled by an

appropriate linear combination of these results since any field can be decomposed into parts parallel and perpendicular to the plane of incidence.

When we speak of optical measurements on a material, we are considering an experimental determination of the ratio of the reflected or transmitted intensity to the incident intensity. These intensities are proportional to an energy flow, and in this connection, the reflectivity of the material is defined by

$$R = - \frac{\bar{\underline{S}}'' \cdot \underline{n}}{\bar{\underline{S}} \cdot \underline{n}} \tag{C-18}$$

where $\bar{\underline{S}}$ is the average value of the Poynting vector which describes the energy flow in the two media.

In the case when the first medium is a dielectric, $k_2 = k_2'' = 0$, and the total field there is the sum of the incident and reflected waves. The average energy flow is then

$$\bar{\underline{S}}_{in} = \tfrac{1}{2} \mathrm{Re}(\tilde{\underline{E}}^* + \tilde{\underline{E}}''^*) \times (\tilde{\underline{H}} + \tilde{\underline{H}}'') \tag{C-19}$$

$$= \tfrac{1}{2} \mathrm{Re} \left\{ \tilde{\underline{E}}_o^* e^{-i\underline{k}_1 \cdot \underline{r}} \times \tilde{\underline{H}}_o e^{i\underline{k}_1 \cdot \underline{r}} + \tilde{\underline{E}}_o''^* e^{-i\underline{k}_1'' \cdot \underline{r}} \times \tilde{\underline{H}}_o'' e^{i\underline{k}_1'' \cdot \underline{r}} \right.$$

$$\left. + \tilde{\underline{E}}_o^* e^{-i\underline{k}_1 \cdot \underline{r}} \times \tilde{\underline{H}}_o'' e^{i\underline{k}_1 \cdot \underline{r}} + \tilde{\underline{E}}_o''^* e^{-i\underline{k}_1 \cdot \underline{r}} \times \tilde{\underline{H}}_o e^{i\underline{k}_1 \cdot \underline{r}} \right\}$$

$$+ \left(\tilde{\underline{E}}_o^* \times \tilde{\underline{H}}_o''\right) e^{-i(\underline{k}_1 - \underline{k}_1'')\cdot\underline{r}} + \left(\tilde{\underline{E}}_o''^* \times \tilde{\underline{H}}_o\right) e^{-i(\underline{k}_1 - \underline{k}_1)\cdot\underline{r}} \Big\}$$

$\bar{\underline{S}}_{in} = \bar{\underline{S}} + \bar{\underline{S}}'' + \underline{S}_{int}$ with obvious definitions.

The experiments with which we are usually concerned are such that the first medium is a vacuum, hence a lossless dielectric, and we can have the incident electric field either parallel or perpendicular to the plane of incidence. Under these conditions, we can write

$$\tilde{\underline{E}}_o^* = \tilde{\underline{E}}_{os}^* = \tilde{\underline{E}}_{os}^* e^{-i\underline{k}_1\cdot\underline{r}}$$

$$\tilde{\underline{H}}_o = \tilde{\underline{H}}_{os} = \tilde{\underline{H}}_{os} e^{i\underline{k}_1\cdot\underline{r}}$$

can compute

$$\bar{\underline{S}} = \tfrac{1}{2} \operatorname{Re}\left[\tilde{\underline{E}}_o^* \times \tilde{\underline{H}}_o\right] \tag{C-19}$$

$$= \tfrac{1}{2}\left[\tilde{\underline{E}}_{os}^* \times \tilde{\underline{H}}_{os}\right] + \tfrac{1}{2}\left[\tilde{\underline{E}}_{os} \times \tilde{\underline{H}}_{os}^*\right] .$$

We can also find the energy flow in the reflected wave

$$\bar{\underline{S}}'' = \tfrac{1}{2} \operatorname{Re}\left[\tilde{\underline{E}}_o^{*''} \times \tilde{\underline{H}}_o''\right] \tag{C-20}$$

$$= \tfrac{1}{2}\left[\tilde{\underline{E}}_{os}''^* \times \tilde{\underline{H}}_{os}'' + \tilde{\underline{E}}_{os}'' \times \tilde{\underline{H}}_{os}''^*\right]$$

$$= \frac{1}{2\omega\mu_o} (\tilde{E}_{os}''^{*} \tilde{E}_{os}'')\underline{k}_1'' + \frac{1}{2\epsilon\omega} (\tilde{H}_{os}''^{*} \tilde{H}_{os}'')\underline{k}_1''$$

$$= \frac{1}{2\omega\mu_o} \tilde{r}_s^{*}\tilde{r}_s (\tilde{E}_{os}^{*}\tilde{E}_{os})\underline{k}_1'' + \frac{\tilde{r}_p^{*}\tilde{r}_p}{2\epsilon\omega} (\tilde{H}_{os}^{*}\tilde{H}_{os})\underline{k}_1''$$

using the definition of $\tilde{r}_s$ and $\tilde{r}_p$.

The interference terms $\underline{\tilde{S}}_{int}$ can be calculated in a similar manner, but the calculation is much more complicated. The result shows that this part gives an energy only parallel to the boundary plane, and arises only from the overlap in the incident and reflected beams. In a typical reflectance experiment, collimated beams are used and the only overlap occurs near the surface. Phase cancellation will cause this part to approach zero at normal distances from the surface allowing us to ignore it.

Now, we have already related the amplitude reflection coefficients to the $\tilde{k}_y$'s, so if we can show what these $\tilde{k}_y$'s reveal about the complex index of refraction, we will have shown how to obtain this index from optical reflectivity measurements.

From Maxwell equations (C-4) and (C-5) we obtain

$$\underline{\tilde{k}} \times (\underline{\tilde{k}} \times \underline{\tilde{E}}) = \omega\tilde{\mu}\underline{\tilde{k}} \times \underline{\tilde{H}} = -\omega^2\tilde{\mu}\tilde{\epsilon}\underline{\tilde{E}}$$

$$= \underline{\tilde{k}}(\tilde{k} \cdot \underline{\tilde{E}}) - \underline{\tilde{E}}(\tilde{k} \cdot \underline{\tilde{k}})$$

Therefore, $\underline{\tilde{k}} \cdot \underline{\tilde{k}} = \tilde{\mu}\,\tilde{\epsilon}\,\omega^2 = \tilde{k}_e\tilde{k}_m \frac{\omega^2}{c^2}$ since

$$\tilde{\mu} = \mu_o \tilde{k}_m \quad \text{and} \quad \tilde{\epsilon} = \epsilon_o \tilde{k}_e \quad \text{and} \quad \mu_o \epsilon_o = \frac{1}{c^2} \ .$$

But by the previous definition of the complex index of refraction,

$$n_c = n + i\chi \ , \quad \underline{\tilde{k}} \cdot \underline{\tilde{k}} = \frac{\omega^2}{c^2} n_c^2$$

so

$$\underline{\tilde{k}} \cdot \underline{\tilde{k}} = \tilde{k}_x^2 + \tilde{k}_y^2 = \underline{\tilde{k}} \cdot \underline{\tilde{k}}'' = \tilde{k}_x''^2 + \tilde{k}_y''^2 = \frac{\omega^2}{c^2} (n + i\chi)^2$$

and

$$\underline{\tilde{k}} \cdot \underline{\tilde{k}}' = \tilde{k}_x'^2 + \tilde{k}_y'^2 = \frac{\omega^2}{c^2} (n'+i\chi')^2$$

We can solve this for $\tilde{k}_y' = \left[\frac{\omega^2}{c^2} (n' + i\chi')^2 - \tilde{k}_x'^2\right]^{\frac{1}{2}}$ and substitute into the expression for $\tilde{r}_s$ to yield

$$\underline{\tilde{r}}_s = \frac{\tilde{k}_y - \tilde{k}_y'}{\tilde{k}_y + \tilde{k}_y'} = \frac{\tilde{k}_y - \left[\frac{\omega^2}{c^2} (n'+i\chi')^2 - k_x'^2\right]^{\frac{1}{2}}}{\tilde{k}_y + \left[\frac{\omega^2}{c^2} (n'+i\chi')^2 - k_x'^2\right]^{\frac{1}{2}}} \qquad \text{(C-21)}$$

Now, if we are dealing with a lossless first medium, e.g., a vacuum, then from Snell's law or from the previously found relation $\tilde{\underline{k}}_x = \tilde{\underline{k}}_x' = \tilde{\underline{k}}_x''$, we get $|\underline{k}_1| \sin\theta = |\underline{k}_1'| \sin\theta$ and $|\underline{k}_2| \sin\theta = |\underline{k}_2'| \sin\theta'$ so if $\tilde{\underline{k}}_2 = 0$, then $|\underline{k}_2| \sin\theta = 0 = |\underline{k}_2'| \sin\theta'$ in Figure 1, so $\theta' = 0$ or $\tilde{k}_2' = 0$. In this case, then,

$$\tilde{k}_x'^2 = \tilde{k}_x' \tilde{k}_x'^* = [|\underline{k}_1'| \sin\theta']^2$$

so $\tilde{k}_1'^2 = |\underline{k}_1|^2 \sin^2\theta$. We have also $\tilde{k}_y = |k_1| \cos\theta$, so

$$\tilde{r}_s = \frac{|k_1|\cos\theta - \left[\frac{\omega^2}{c^2}(n' + i\chi')^2 - \sin^2\theta\ |k_1|^2\right]^{\frac{1}{2}}}{|k_1|\cos\theta + \left[\frac{\omega^2}{c^2}(n' + i\chi')^2 - \sin^2\theta\ |k_1|^2\right]^{\frac{1}{2}}} \qquad \text{(C-22)}$$

$$\tilde{r}_s = \frac{\cos\theta - \left[\frac{\omega^2}{c^2}\frac{(n' + i\chi')^2}{|k_1|^2} - \sin^2\theta\right]^{\frac{1}{2}}}{\cos\theta + \left[\frac{\omega^2}{c^2}\frac{(n' + i\chi')^2}{|k_1|^2} - \sin^2\theta\right]^{\frac{1}{2}}} \qquad \text{(C-23)}$$

But in the vacuum $|k_1|^2 = \frac{\omega^2}{c^2} n^2$ and

$$\tilde{r}_s = \frac{\cos\theta - \left[\left(\frac{N'}{n}\right)^2 - \sin^2\theta\right]^{\frac{1}{2}}}{\cos\theta + \left[\left(\frac{N'}{n}\right) - \sin^2\theta\right]^{\frac{1}{2}}} \qquad \text{(C-24)}$$

where $N' = n' + ik'$.

From this reflection coefficient, the reflectivity for normal incidence is easily found as

$$R_{normal} = \left|\frac{n - \tilde{N}'}{n + \tilde{N}'}\right|^2 = \frac{(n - n')^2 + k'^2}{(n + n')^2 + k'^2} \qquad (C\text{-}25)$$

but for off-normal incidence, the problem is more complicated. After introducing a complex cosine by the relation

$$n'\cos\theta = (n'^2 - \sin^2\theta)^{\frac{1}{2}} = a - ib$$

the formula for off-normal reflectance is found as

$$R_s = \frac{a^2 + b^2 - 2a\cos\theta + \cos^2\theta}{a^2 + b^2 + 2a\cos\theta + \cos^2\theta} \qquad (C\text{-}26)$$

where

$$a^2 = \tfrac{1}{2}\left\{[n^2 - k^2 - \sin^2\theta)^2 + 4n^2k^2]^{\frac{1}{2}} + (n^2 - k^2 - \sin^2\theta)\right\}$$

and

$$b^2 = \tfrac{1}{2}\left\{[n^2 - k^2 - \sin^2\theta)^2 + 4n^2k^2] - (n^2 - k^2 - \sin^2\theta)\right\}$$

thus yielding the optical constants n and k from reflectivity measurements.

In the remainder of this appendix, computer techniques employed to analyze the optical reflectivity data are described. Once the reflectivities at 22.5° and 67.5° were known, approximate values of n and k which gave those reflectances were determined by superimposing isoreflectance curves calculated at the two angles for a substantial range of n and k values. The common point of the curves represented an approximate solution of the Fresnel equations for the observed reflectances which could then be used to determine a more refined solution.

The final analysis was a least-squares, iterative approach by computer to a solution of the Fresnel equations which gave the smallest error between calculated and observed reflectivity values at the two angles. The computer technique calculated reflectivities at 22.5° and 67.5° for sixteen nearest-neighbors in the n-k plane and compared these values with the observed data. That point which gave the least squared error was chosen as a new approximate solution and the procedure was repeated. When the "approximate" solution gave the smallest error of all the points nearby in the n-k plane, that point was assumed to be the most accurate solution for the input reflectivity data. Roughly ten iterations were required to produce the final solution when accurate data and good initial approximations were available. From these final n and k values, the real and imaginary parts of the dielectric constant and the bulk and surface plasmon excitation probabilities were calculated. This method was used to analyze the optical data at photon energies selected to describe the dielectric response at all

interesting energies. In the computer program reproduced here, the input data are arranged as 22.5° reflectivity, 67.5° reflectivity, photon energy, approximate n solution and approximate k solution. The program output lists all the calculated errors at each n-k point tested before the final solution was reached so that trends in the data analysis can be used to shorten the required computer time.

The response of a medium to an electromagnetic disturbance may be described in part by the complex dielectric constant $\epsilon(\omega)$. The frequency dependence of this parameter characterizes the physical properties of the medium and may be used to obtain valuable information concerning its fundamental electronic structure. This dielectric constant may be separated into real and imaginary parts, $\epsilon(\omega) = \epsilon_1(\omega) + i\epsilon_2(\omega)$. The real part ϵ_1 describes dispersion of the electromagnetic wave, the imaginary part ϵ_2 describes dissipation. ϵ itself is not directly determined from optical measurements; instead one determines the related optical constant n and, the refractive index, and attenuation index, respectively. The relations between ϵ and n and k are then easily determined by considering Maxwell's equations for a medium in which refraction and attenuation of an electromagnetic field are permitted. One finds

$$\epsilon_1 = n^2 - k^2$$

and

$$\epsilon_2 = 2nk \ .$$

Using $\epsilon(\omega)$ to describe the system response one seeks to determine the excitation frequencies and probabilities for single-particle transitions and the excitation energies of collective resonances in the solid.

The excitation of bulk and surface collective resonances by the incident photon is revealed by the behavior of $\epsilon(\omega)$. For metals adequately described as a free electron gas, these excitation energies can be calculated from

$$\hbar\omega_p = \hbar \left(\frac{4\pi ne^2}{m}\right)^{\frac{1}{2}}$$

for the bulk oscillation, and from

$$\hbar\omega_s = \frac{1}{\sqrt{1+\epsilon'}} \hbar\omega_p$$

for the surface oscillation. Here ϵ' is the dielectric constant of the metal-vacuum interface, so the energy of the surface plasmon is dependent on the sample surface conditions. The probabilities for excitation of these collective modes are proportional to

$$-\mathrm{Im}\left(\frac{1}{\epsilon}\right) \text{ and } -\mathrm{Im}\left(\frac{1}{\epsilon+1}\right)$$

for the bulk and surface plasmon oscillations respectively. A further condition that these oscillations exist as a well-defined excitation is

that $\varepsilon(\omega) = 0$ and $\varepsilon(\omega) = -\varepsilon'$ at the oscillation frequencies of the bulk and surface plasmons. When damping of the collective excitation by single-particle excitations is small, $\varepsilon_2 \approx 0$, and so the resonance frequencies would be found when $\varepsilon_1 \approx 0$ and $\varepsilon_1 \approx -1$ for the bulk and surface plasmon oscillations of a clean metal sample. For metals where the free electron model is not applicable because of strong core-valence coupling, this analysis must be applied cautiously.

```
COMMENT THIS PROGRAM DOES A LEAST SQUARES FIT TO OPTICAL
        REFLECTIVITY DATA IN ORDER TO DETERMINE THE "N" AND "K"
        OF THE COMPLEX INDEX OF REFRACTION    ;
FILE IN     FLIN  (2,10)  ;
FILE OUT FLOT 16(2,15);
FORMAT IN  FMT14 (F8.6, X2, F8.6, X2, F5.2 , X5 , F5.2, X5, F5.2);


FORMAT OUT F03(X2,F4.2,X6,F4.2);


FORMAT OUT FMT05 ("PROCESSOR",X6,"I/O");


FORMAT OUT FMT06 (F5.3, X4, F5.3,X7, F5.2, X9, F11.9 ,X7, F5.2 )    ;


FORMAT OUT FMT07 ( "NVAL",X5,"KVAL", X5,"POLARIZATION",X5,"SUMSQ",
                    X8, "ENERGY"// )    ;

FORMAT OUT FMT08 (X2, F6.3, X4, F6.3, X4, F6.3, X8, F6.3 )    ;


FORMAT OUT FMT09 ( "EPSILON1",X2,"EPSILON2",X2,"ENERGY LOSS",X2,

"ENERGY SURFACE LOSS"/);


INTEGER  I, J, M, D,G ;
REAL N, K, PHI, P, MIN,          E1, E2, EL, ESL    ;
REAL ARRAY  ND, KD, RAC, RAD, A  [0:25] ;
REAL ARRAY RAOBS1, RAOBS2,ENER,NS, XS [0:25] ;
LABEL       LOOP   ;
```

```
REAL PROCEDURE TAN(PHI)    ;
VALUE PHI    ;
REAL PHI    ;
BEGIN
TAN       ← SIN(PHI) / COS(PHI)    ;
END TAN    ;
DEFINE      NMK = ((N*2)-(K*2)-((SIN(PHI))*2))   #   ;
DEFINE      NMKP = SQRT ( ( NMK*2 ) + ( 4 × (N*2 ) × (K*2) ) )   #    ;
DEFINE      A   = SQRT ( 0.5 × ( NMKP + NMK ) ) #   ;
DEFINE      BSQ   =      0.5 × ( NMKP - NMK )    #   ;
DEFINE      RP   = RPNUM / RPDEN   #     ;
DEFINE      RPNUM   =  RS × (( (A -(SIN(PHI) × TAN(PHI)))*2) + BSQ )#   ;
DEFINE      RPDEN   = (( (A +(SIN(PHI) × TAN(PHI)))*2) + BSQ )#    ;
DEFINE      RA   = 0.5 × ((RP × (1+P))+(RS × (1-P)))   #      ;
DEFINE      RS    =  (( A - COS(PHI))*2 + BSQ ) /((A +COS(PHI))*2 + BSQ)#;
WRITE (FLOT[NO]);
FOR I ← 1 STEP 1 UNTIL 2 DO
READ ( FLIN, FMTI4, RADBS1[I],RADBS2[I],ENER[I],NS[I],KS[I]);
CLOSE (FLIN,RELEASE);
FOR I ← 1 STEP 1 UNTIL 2 DO
WRITE(FLOT,FMTI4,RADBS1[I],RADBS2[I],ENER[I],NS[I],KS[I]) ;
            H ← -1    ;
FOR I ← 1 STEP 1 UNTIL 2 DO
            BEGIN
            WRITE (FLOT, FMT07);
            P ← 0;
            H ← H + 2    ;
            G ← 0    ;
            RAD[H] ← RADBS1[I]     ;
            RAD[H+1] ← RADBS2[I]    ;
LOOP:       J ← 0;
FOR PHI ← 0.39270, 1.17810 DO
            BEGIN
            FOR N ← NS[I] - 0.01 STEP 0.01 UNTIL NS[I] + 0.01 DO
```


Computer Analysis (Continued).

```
BEGIN
    FOR K ← KS[I]-0.01 STEP 0.01 UNTIL KS[I]+0.01 DO
    BEGIN
    J ← J + 1    ;
    RAC[J] ←  RA    ;
    KD[J] ← K;
    ND[J] ← N;
    END;END;END;
FOR J ← 1 STEP 1 UNTIL 9 DO
M[J]  ←  (RAD[H] - RAC[J] )*2 + ( RAD[H+1]- RAC[J+9])*2     ;
MIN ← M[1]    ;
Q ← 1    ;
FOR J ← 2 STEP 1 UNTIL 9 DO
    BEGIN
    IF M[J] ≤ MIN THEN
    BEGIN
    MIN ← M[J]     ;
    Q ← J   ;
    END;END;
NS[I] ← ND[Q] ;
KS[I] ← KD[Q] ;
WRITE ( FLOT, FMT06, NS[I], KS[I], P, MIN, ENER[I] ) ;
    G ← G+1;
    IF N ≠ 5 THEN GO LOOP ELSE
    BEGIN
    E1 ← NS[I]*2 - KS[I]*2;
    E2 ← 2 × NS[I] × KS[I];
    EL ← E2 / (NS[I]*2 + KS[I]*2 ) *2;
    WRITE ( FLOT, FMT09 )    ;
    WRITE (FLOT, FMT06, E1, E2, EL, ESL )    ;
    END;END; END.
```

Computer Analysis (Continued).

BIBLIOGRAPHY†

1. F. Seitz, in Imperfections in Nearly Perfect Crystals, p. 76, John Wiley & Sons, Inc., New York, 1952.
2. J. L. Robins and J. B. Swan, Proc. Phys. Soc. 76, 857 (1960).
3. H. Ehrenreich and H. R. Philipp, Phys. Rev. 128, 1622 (1962).
4. E. Rudberg, Proc. Roy. Soc. A127, 111 (1930).
5. G. Ruthemann, Ann. Physik 6, 113 (1948).
6. E. Rudberg and J. C. Slater, Phys. Rev. 50, 150 (1936).
7. H. Wanatabe, Phys. Rev. 95, 1684 (1954).
8. L. B. Leder, H. Mendlowitz and L. Marton, Phys. Rev. 101, 1460 (1956).
9. B. Gauthe, Ann. Phys., Paris 3, 915 (1958).
10. E. J. Steinglas, Nature 178, 1387 (1956).
11. L. Marton and L. B. Leder, Phys. Rev. 94, 203 (1954).
12. L. B. Leder, Phys. Rev. 107, 1569 (1957).
13. D. Bohm and D. Pines, Phys. Rev. 92, 626 (1955), and preceding papers.
14. W. Lang, Optik 5, 499 (1949).
15. C. J. Powell and J. B. Swan, Phys. Rev. 115, 869 (1959).
16. H. Wanatabe, J. Phys. Soc. Japan 10, 321 (1955).
17. G. Meyer, Z. Physik 148, 61 (1957).
18. L. Marton, Rev. Mod. Phys. 28, 172 (1956).
19. P. A. Wolff, Phys. Rev. 92, 18 (1953).
20. E. N. Adams, Phys. Rev. 98, 947 (1955).

---

† Abbreviations herein follow the form recommended by the American Institute of Physics.

BIBLIOGRAPHY (Continued)

21. R. E. Schlier and H. E. Farnesworth, J. Chem. Phys. 30, 917 (1959).

22. J. J. Lander and J. Morrison, J. Chem. Phys. 37, 729 (1962).

23. T. E. Feuchtwang, Phys. Rev. 155, 715 (1967).

24. A. Taloni and D. Haneman, Surface Science 8, 215 (1967).

25. D. Haneman, Phys. Rev. 121, 1093 (1961).

26. E. Bauer, Fourth International Materials Symposium, Berkeley, California, June 19-21, to be published, 1968.

27. I. Tamm, Z. Physik 76, 849 (1932).

28. A. U. MacRae, Surface Science 2, 522 (1964).

29. P. A. Flinn, S. L. Ruby and W. L. Kell, Science 143, 1434 (1964).

30. R. F. Wallis and D. C. Gazis, Phys. Rev. 128, 106 (1962).

31. B. C. Clark, R. Herman and R. F. Wallis, Phys. Rev. 139, 860 (1965).

32. A. A. Maradudin and J. Melngailis, Phys. Rev. 133, A1188 (1964).

33. E. R. Jones, J. T. McKinney and M. B. Webb, Bull. Amer. Phys. Soc. 10, 324 (1965).

34. J. Aldag and R. M. Stern, Phys. Rev. Lett. 14, 857 (1965).

35. D. L. Huber, Phys. Rev. 153, 722 (1967).

36. R. F. Wallis and A. A. Maradudin, Phys. Rev. 148, 962 (1966).

37. S. F. Edwards, Proc. Roy. Soc. A267, 518 (1962).

38. H. Jones, Proc. Roy. Soc. A267, 139 (1962).

39. J. M. Ziman, Proc. Phys. Soc. 88, 387 (1966).

40. G. C. Sergeeva, Soviet Phys. JETP 21, 108 (1965).

41. H. Jones, Proc. Roy. Soc. A294, 405 (1966).

42. M. Steenbeck, Z. Physik 76, 260 (1932).

43. R. Kronig and J. Korringa, Physica 10, 406, 800 (1943).

BIBLIOGRAPHY (Continued)

44. D. Pines, in Solid State Physics, Vol. 1, p. 367, Academic Press, Inc., New York, 1955.

45. R. H. Ritchie, Phys. Rev. 106, 874 (1957).

46. E. A. Stern and R. A. Ferrell, Phys. Rev. 120, 130 (1960).

47. C. J. Powell and J. B. Swan, Phys. Rev. 118, 640 (1960).

48. J. Hubbard, Proc. Phys. Soc. A68, 976 (1955) and preceding papers.

49. H. Kanazawa, Progr. Theo. Phys., Japan 13, 227 (1955).

50. E. N. Adams, Phys. Rev. 85, 41 (1952).

51. N. F. Mott, Proceedings of the Tenth Solvay Congress, Brussels, 1954.

52. P. Nozieres and D. Pines, Phys. Rev. 109, 762 (1958).

53. J. Lindhard, Kgl. Danske Videnskab. Selskab, Mat. -fys. Medd. 28, No. 8 (1954).

54. F. C. Brown, The Physics of Solids, W. A. Benjamin, Inc., New York, 1967.

55. H. Frohlich and H. Pelzer, Proc. Phys. Soc. A68, 44 (1955).

56. D. Pines, Elementary Excitations in Solids, W. A. Benjamin, Inc., New York, 1963; see p. 65.

57. R. Resnick and D. Halliday, Physics for Students of Science and Engineering, p. 310, John Wiley & Sons, Inc., New York, 1960.

58. A. S. Davydov, Quantum Mechanics, p. 309, Addison-Wesley Publishing Co., Inc., Reading, Massachusetts, 1965.

59. W. T. Spencer and M. P. Givens, J. Opt. Soc. Amer. 54, 1337 (1964).

60. R. W. Roberts and T. A. Vanderslice, Ultrahigh Vacuum and Its Applications, Prentice Hall, Inc., Englewood, N. J., 1963.

61. W. F. Brusner and T. H. Batzer, Practical Vacuum Techniques, Reinhold Publishing Corp., New York, 1965.

62. J. J. Lander, in Progress in Solid State Chemistry, Vol. 2, p. 1, Pergamon Press, New York, 1965.

BIBLIOGRAPHY (Continued)

63. L. B. Leder and J. B. Simpson, Rev. Sci. Instr. 29, 571 (1958).

64. J. A. Simpson, Rev. Sci. Instr. 32, 1283 (1961).

65. F. A. Jenkins and H. E. White, Fundamentals of Optics, McGraw-Hill Book Co., Inc., New York, 1957; see p. 51.

66. W. R. Hunter, J. Opt. Soc. Amer. 55, 1197 (1965).

67. F. W. Young, Jr. and T. R. Wilson, Rev. Sci. Instr. 32, 559 (1961).

68. G. W. Simmons, D. F. Mitchell, and K. R. Lawless, Surface Science 8, 130 (1967).

69. W. W. Beeman and H. Friedman, Phys. Rev. 56, 392 (1939).

70. S. T. Stephenson, Phys. Rev. 58, 877 (1940).

71. A. Ia Viatskin, Soviet Phys-Techn. Phys. 3, 2252 (1958).

72. M. Creuzberg, unpublished.

73. H. Raether, in Springer Tracts in Modern Physics, Vol. 33, Springer-Verlag, Berlin, 1965.

74. C. J. Powell, Aust. J. Phys. 13, 145 (1960).

75. O. Hachenberg and W. Brauer, Advances in Electronics and Electron Physics 11, 413 (1959).

76. A. J. Dekker, in Solid State Physics, Vol. 6, p. 251, Academic Press, Inc., New York, 1958.

77. H. D. Hagstrum, Phys. Rev. 150, 492 (1966).

78. G. F. Amelio and E. J. Scheibner, Surface Science, to be published and, G. F. Amelio, Ph. D. Thesis, to be submitted, Dept. of Phys., Georgia Institute of Technology, 1969.

79. P. W. Palmberg and T. N. Rhodin, J. Appl. Phys. 39, 2425 (1968).

80. G. W. Simmons, private communication.

81. G. A. Burdick, Phys. Rev. 129, 138 (1963).

82. B. Segall, Phys. Rev. 125, 109 (1962).

83. A. B. Pippard, Proc. Roy. Soc. A250, 325 (1957).

BIBLIOGRAPHY (Concluded)

84. P. P. Reichertz and H. E. Farnesworth, Phys. Rev. 75, 1902 (1949).

85. L. Marton and L. B. Leder, Phys. Rev. 94, 203 (1954).

86. W. Kleinn, Optik 11, 226 (1954).

87. H. Wanatabe, J. Phys. Soc. Japan 9, 920 and 1035 (1954).

88. B. Gauthe, Compt. Rend. 239, 399 (1954).

89. F. Pradul and F. Saporte, C. R. Acad. Sci., Paris 246, 2880 (1958).

90. I. Marklund, S. Anderson and J. Martinson, Arkiv Physik 37, 127 (1968).

91. D. Beaglehole, Proc. Phys. Soc. 85, 1007 (1965).

92. S. Roberts, Phys. Rev. 114, 104 (1959).

93. J. R. Beattie and G. K. T. Conn, Phil Mag. 46, 989 (1955).

94. J. G. Hanus, MIT Solid State and Molecular Theory Group Quarterly Progress Report, No. 44, 29 (1962).

95. H. Ehrenreich, H. R. Philipp and D. J. Olechna, Phys. Rev. 131, 2469 (1963).

96. W. Lang, Optik 3, 233 (1948).

97. G. Mollenstedt, Optik 5, 499 (1949).

98. C. J. Powell, Phys. Rev. Lett. 15, 852 (1965).

VITA

Leland Kay Jordan, III was born September 19, 1942 in Atlanta, Georgia. He is the oldest of three children of Leland K. Jordan, Jr. and Margaret Garbutt Jordan. On August 28, 1965, he was married to Pamela Ellen Davies of Macon, Georgia; they have one child, Lizbeth Katheryn.

Mr. Jordan graduated from Lanier Senior High School in Macon in June 1960 and entered the Georgia Institute of Technology in the fall of that same year. He received a Bachelor of Physics degree in June 1964 and the Master of Science degree in 1966.

Mr. Jordan was employed as a student assistant in 1963 with the Magnetics Section of the Physical Sciences Division at Georgia Institute of Technology. Since 1966, he has worked as a graduate research assistant under Dr. Scheibner in low-energy electron scattering studies. He is a member of Sigma Pi Sigma, Sigma Xi, and the American Physical Society.